NCCR QSIT Junior Meeting 2018

Passugg, 4-6 June, 2018

Contact

Eric Bonvin
ETH Zürich
Photonics Laboratory
Tel.: +41 44 633 09 94
E-Mail: ebonvin@ethz.ch

Felix Tebbenjohanns
ETH Zürich
Photonics Laboratory
Tel.: +41 44 633 05 51
E-Mail: tefelix@ethz.ch

Cover image: With kind permission of Chur Tourismus (www.churtourismus.ch)

Contents

1

Program

	Monday, June 4th	Tuesday, June 5th	Wednesday, June 6th
8:00		Breakfast	Breakfast
9:00		Ronja Khelifa	Tamás Kriváchy
9:15		Corentin Pignot	Oscar Garcia
9:30		Anna Kuzmina	Oindrila Deb
9:45		Zijin Lei	Jodok Happacher
10:00		Coffee break	Coffee break
10:45		Johan Andberger	Amina Ribeiro
11:00		Pol Welter	Aleksandra Nelson
11:15		Mikolaj Roguski	Olivier Faist
11:30	Registration	Anina Leuch	Mehdi Ramezani
11:45		Jann Ungerer	Victor Helson
12:15	Lunch	Lunch package	Lunch
13:30	Welcome	Afternoon activities	Jeffrey Mohan
13:45	Alexandra Nagy		Natasha Tomm
14:00	Alexander Baumgärtner		Gaëtan Gras
14:15	Maryse Ernzer		Brennan de Neeve
14:30	Stefania Balasiu		Closing Remarks
14:45	Coffee break		Departure
15:30	Urban Senica		
15:45	Benedikt Kratochwil		
16:00	Liang Zhai		
16:15	Kilian Seibold		
16:30	Alessia Pally		
17:30	Dinner & Poster Session	Conference Dinner	
19:30			

2

Abstracts

A driven-dissipative quantum Monte Carlo method for open quantum systems

Alexandra Nagy[1] and Vincenzo Savona[1]

[1]*Institute of Physics, Ecole Polytechnique Fdral de Lausanne (EPFL), CH-1015, Lausanne, Switzerland*

We develop a real-time Full Configuration Interaction Quantum Monte Carlo approach to model driven-dissipative open quantum systems with Markovian system-bath coupling. The method enables stochastic sampling of the Liouville-von-Neumann time evolution of the density matrix, thanks to a massively parallel algorithm, thus providing estimates of observables on the non-equilibrium steady state. We present the underlying theory, and introduce initiator technique and importance sampling to reduce the statistical error. Finally, we demonstrate the efficiency of our approach by applying it to the driven-dissipative two-dimensional XYZ spin-1/2 model on lattice.

I. INTRODUCTION

The study of the nonequilibrium dynamics of many-body open quantum systems has attracted increasing attention in recent years, due to the progress in several experimental areas, including ultracold atomic gases, trapped ions, and superconducting circuits [1–4]. A common feature of these systems is the coupling to an external environment. The time evolution is then governed by the Liouville-von-Neumann equation which – in the case of stationary external conditions – typically drives it into a nonequilibrium steady state (NESS). Here, the competition between the Hamiltonian dynamics and the system-bath interaction gives rise to a multitude of novel phenomena, including nonequilibrium dissipative phase transitions [5, 6].

In this paper, we develop a real-time Projector Monte Carlo (PMC) approach to open quantum systems, which we call driven-dissipative quantum Monte Carlo (DDQMC). DDQMC shares many of the features of a PMC, but it samples the elements of the complex-valued density matrix instead of the wavefunction. The method does not truncate the Hilbert-space and contrary to tensor network methods, its applicability is not bound to the dimensionality of the system. In order to demonstrate the use of DDQMC, we simulate a two-dimensional spin lattice governed by the Heisenberg XYZ Hamiltonian interacting with a dissipative environment.

II. DRIVEN-DISSIPATIVE QUANTUM MONTE CARLO

We describe now how the dynamics of open quantum systems following the Liouville-von-Neumann equation can be cast into a Monte Carlo algorithm. The approach is based on the algorithm of FCIQMC, for a complete derivation readers are referred to [7–11].

The general problem we aim to solve is that of a quantum system with several degrees of freedom, in the presence of external driving fields and Markovian coupling to the environment. The evolution of the steady matrix $\hat{\rho}$ is then governed by the Liouville-von-Neumann master equation [12]

$$\frac{d\hat{\rho}}{dt} = \mathcal{L}(\hat{\rho}) = -i[\hat{H}, \hat{\rho}] + \sum_i \mathcal{L}_i(\hat{\rho})\,. \tag{1}$$

The dissipative part of the dynamics is described by

$$\sum_i \mathcal{L}_i(\hat{\rho}) = -\sum_i \frac{\gamma_i}{2}\left[\left\{\hat{F}_i^\dagger \hat{F}_i, \hat{\rho}\right\} - 2\hat{F}_i\hat{\rho}\hat{F}_i^\dagger\right]\,, \tag{2}$$

where $\hat{F}_i$ are the jump operators, characterizing the transitions induced by the environment, and γ_i are the corresponding transition rates. If the density matrix is expressed in vectorized form, the Liouvillian superoperator can be expressed in matrix form using Kronecker products [13]. Then Eq. (1) can be written in the form of

$$\frac{d\rho_{ij}}{dt} = \mathcal{L}_{ij}^{ij}\rho_{ij} + \sum_{l,m\neq i,j} \mathcal{L}_{ij}^{lm}\,\rho_{lm}\,, \tag{3}$$

where $\mathcal{L}_{ij}^{lm}$ are the matrix elements of the superoperator. Here ρ_{ij} represents the now complex valued amplitude of one of the basis operators $|\phi_i\rangle\langle\phi_j|$, from now on referred as "configurations".

In order to stochastically represent Eq. (3), we introduce a fundamental unit called *walker*. Each walker has a sign ($q = \pm 1$), and contributes to sample the amplitude of one of the configurations. Since the density matrix elements are complex, we introduce two sets of walkers for the real and imaginary parts respectively. The dynamics of the walker population is determined by a set of rules designed to stochastically sample Eq. (3). The complete derivation for DDQMC can be found in our recently published paper [14].

III. RESULTS

In order to demonstrate the effectiveness of DDQMC, we simulated the two-dimensional spin-1/2 XYZ Heisenberg lattice in the presence of a dissipating channel which tends to relax each spin into the $|s_z = -1/2\rangle$ state. The model follows the Liouville-von-Neumann equation and the Hamiltonian is governed by ($\hbar = 1$)

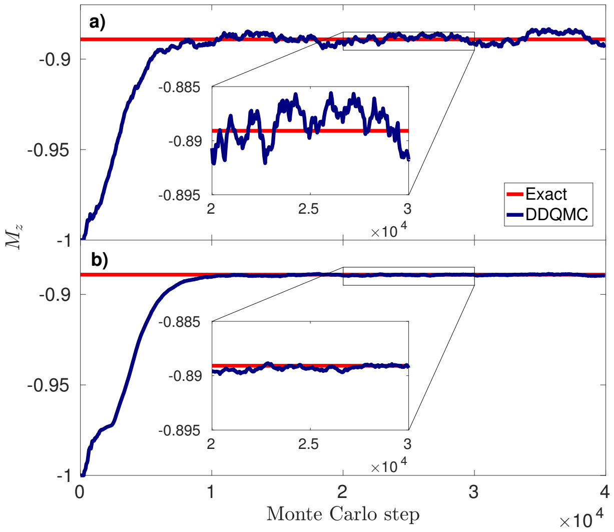

FIG. 1: The exact and the DDQMC magnetization values (in units of $\hbar$) for the 3×3 dissipative XYZ Heisenberg lattice with periodic boundary condition. The coupling parameters are $J_x/\gamma = 0.225$, $J_y/\gamma = 0.335$ and $J_z/\gamma = 0.25$. The diagonal population was limited to (a) 50^4 and (b) 20^6 walker.

$$\hat{H} = \sum_{\langle l,m \rangle} \left(J_x \hat{S}^x_l \hat{S}^x_m + J_y \hat{S}^y_l \hat{S}^y_m + J_z \hat{S}^z_l \hat{S}^z_m \right) \quad (4)$$

$$\frac{\mathrm{d}\hat{\rho}}{\mathrm{d}t} = -i[\hat{H}, \hat{\rho}] - \frac{\gamma}{2} \sum_k \left[\left\{ \hat{S}^+_k \hat{S}^-_k, \hat{\rho} \right\} - 2\hat{S}^-_k \hat{\rho} \hat{S}^+_k \right] \quad (5)$$

where $\hat{S}^\alpha_l$ are the spin operators acting on the l-th spin, J_α are the coupling constants between nearest neigbour spins, γ is the dissipation rate, and $\hat{S}^\pm_m = \hat{S}^x_m \pm i\hat{S}^y_m$.

Recently, the system has attracted significant interest since the competition between the coherent Hamiltonian dynamics and the incoherent spin flips leads to a dissipative phase transition. The steady-state magnetization per site is defined as

$$M_z = \frac{1}{N} \sum_{k=1}^{N} \mathrm{Tr}(\hat{\rho}\hat{\sigma}^z_k), \quad (6)$$

where N is the number of lattice sites.

Figure 1(a) shows the magnetization of the 3×3 lattice as a function of the Monte Carlo iteration step with a diagonal population of 50^4 walkers. The exact solution obtained by directly solving the linear system is also plotted. Increasing the diagonal population to 20^6 reduces the statistical error as seen in the corresponding result in Fig. 1(b). The exact calculations are in agreement with the one obtained by DDQMC.

IV. CONCLUSIONS

We have introduced a quantum Monte Carlo approach to open many-body quantum systems with Markovian system-bath coupling, called DDQMC. The method is based on the FCIQMC algorithm exploiting the analogy between the long-time dynamics of the Lindbladian master equation and the imaginary-time Schrodinger equation. DDQMC allows direct sampling of the steady state density matrices in any discrete basis set, and in all cases studied it has proven to be accurate.

Acknowledgments

We acknowledge enlightening discussions with Markus Holzmann, Mario Geiger and Eduardo Mascarenhas. We are indebted to Hugo Flayac for having provided the MCWF simulations used to benchmark the present results. This work was supported by the Swiss National Science Foundation through Project No. 200021_162357.

---

[1] I. Carusotto and C. Ciuti, Rev. Mod. Phys. **85**, 299 (2013).

[2] M. J. Hartmann, J. Opt. **18**, 104005 (2016).

[3] K. Le Hur, L. Henriet, A. Petrescu, K. Plekhanov, G. Roux, and M. Schiró, Comptes Rendus Physique **17**, 808 (2016).

[4] C. Noh and D. G. Angelakis, Rep. Prog. Phys. **80**, 016401 (2017).

[5] E. M. Kessler, G. Giedke, A. Imamoglu, S. F. Yelin, M. D. Lukin, and J. I. Cirac, Phys. Rev. A **86**, 012116 (2012).

[6] S. Diehl, A. Micheli, A. Kantian, B. Kraus, H. P. Büchler, and P. Zoller, Nat Phys **4**, 878 (2008).

[7] G. H. Booth, A. J. W. Thom, and A. Alavi, J Chem Phys **131**, 054106 (2009).

[8] J. S. Spencer, N. S. Blunt, and W. M. Foulkes, J Chem Phys **136**, 054110 (2012).

[9] N. S. Blunt, T. W. Rogers, J. S. Spencer, and W. M. C. Foulkes, Phys. Rev. B **89**, 245124 (2014).

[10] J. J. Shepherd, G. E. Scuseria, and J. S. Spencer, Physical Review B **90** (2014).

[11] G. H. Booth, S. D. Smart, and A. Alavi, Molecular Physics **112**, 1855 (2014).

[12] C. Gardiner and P. Zoller, *Quantum Noise* (Springer, Berlin, Heidelberg, 2004).

[13] M. Jakob and S. Stenholm, Phys. Rev. A **67**, 032111 (2003).

[14] A. Nagy and V. Savona, arXiv:1802.05931 [quant-ph] (2018), 1802.05931.

A New Apparatus for Trapping and Manipulating Single Strontium Atoms

Alexander Baumgärtner,[1, 2] Ivaylo Madjarov,[2] Alexandre Cooper-Roy,[2] Zeren Lin,[2] Jacob Covey,[2] and Manuel Endres[2]

[1]*Institute of Quantum Electronics, ETH-Hönggerberg, CH-8093, Zürich, Switzerland*
[2]*Division of Physics, Mathematics and Astronomy,*
California Institute of Technology, Pasadena, CA-91125, USA

The assembly of large-scale arrays of individual neutral atoms in optical tweezers is a recently-demonstrated technique to create defect-free many-body systems. To this end, we designed and built a new setup to try this approach with strontium atoms. This novel apparatus allows for long vacuum lifetimes (tens of second) while maintaining high atomic flux for fast loading of the magneto-optical trap at rates of up to 170 ms **rate in kHz or time in ms**. With this apparatus, we realized magneto-optical traps with up to 2×10^8 atoms and demonstrated the imaging of strontium atoms in optical tweezers for the first time. Furthermore, we developed a cooling scheme that allows for imaging and cooling of strontium atoms inside the optical tweezers. This is crucial for the further steps of the experiment, in which we aim to image the atoms multiple times in order to rearrange.

I. INTRODUCTION

Through continuous improvements in the control over quantum systems, simulations of quantum many-body physics with control over single constituents has become a common goal for several experimental platforms. In solid state systems such as superconducting quantum interference devices[1] or semiconductor nanowires[2], the primary challenge remains to isolate mesoscopic structures from their environment to prevent decoherence. Alternatively, atomic systems consisting of ions or ultracold atoms serve as small quantum systems by definition. Here, the coherent control over single constituents (i.e. particles) and manipulation of their interactions poses a significant challenge in this field.

Loaded from a MOT and cooled further inside the small trap, the idea is to build small quantum systems using a bottom-up approach with the ability to entrap them in separate beams, allowing for control over each atom. This platform has already been successfully used in creating small Hubbard building blocks[3], as well as small spin systems interacting via Rydberg excitations[4]. The main challenge with this approach, however, is scalability. The probability of loading one atom into a tweezer is non-deterministic, with typical probabilities reported to lie within the range of 50%[5] to 90%[6]. This results in a vanishing probability of realizing defect-free systems as their size increases. By rearranging the arrays after the initial imaging sequence, this limitation has been overcome by two groups[7,8], which enables scaling these systems to larger sizes with no apparent limit. The aforementioned idea has already been extended to realize 51-atom spin chains as a result of this promising technique[9].

On this basis, we want to investigate this approach further by using atomic strontium instead of the previously investigated rubidium. This should allow for larger system size, higher controllability, and new possibilities to introduce interactions via Rydberg states due to the richer atomic structure of strontium.

II. STRONTIUM

In metrology, strontium has received much attention due to its *Clock transition*, making it an ideal candidate for optical lattice clocks[10,11]. A very cold magneto-optical trap (MOT) that cycles on a singlet-to-triplet line is good for loading tweezers, and a magic wavelength between these two states of this MOT at 515 nm gives a small tweezer confinement at a wavelength where commercially available, high power laser systems exist. These are ideal conditions to scale this technology to larger system sizes.

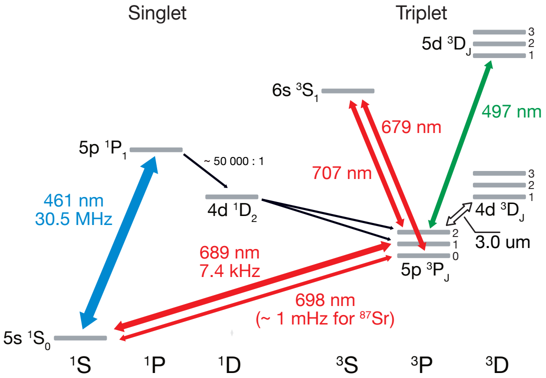

FIG. 1: Level diagram of atomic strontium including all relevant optical transitions for laser cooling and trapping.

III. TWEEZER GENERATION

We use two microscope objectives to produce diffraction limited tweezers with a beam waist of $\approx 1\ \mu$m at a tweezer wavelength of 515 nm.

To pave the way for constructing arrays of tweezers, we decided to use an Acousto-Optical Deflector (AOD) that we drive with multi-tone RF signals, which allows for the generation of multiple beams simultaneously. To

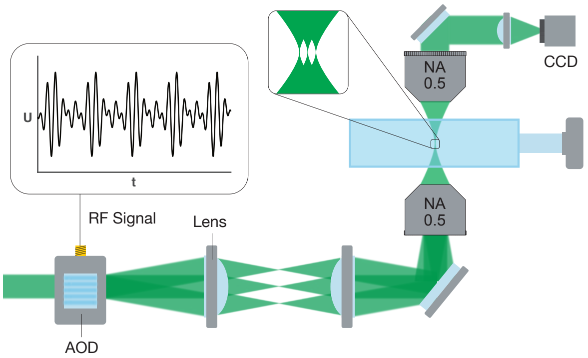

FIG. 2: Illustration of our 4f-system that images the deflection plane of the AOD to the back focal plane of the objective. The two lenses have the same focal length of 250 mm, which was selected to be large to simplify the alignment process. The three different beams are achieved through the superposition of three equidistant frequency tones that are sent to the AOD.

map the deflection in the AOD to spatially distinguished tweezers, we built a unit-magnification telescope to image the deflection plane of the AOD to the back focal plane of the objective. In the simple picture of Fourier optics, this implies that the 4 mm beams with various incident angles are ultimately mapped to small tweezers in the atomic plane, separated by a distance proportional to the differences between their respective RF frequencies. This is illustrated in FIG. 2.

IV. IMAGING

We propose a scheme for fluorescence imaging of strontium atoms in tweezers, which must be capable of imaging single atoms on a time scale of 100 ms without heating the atoms out of the tweezer. This is needed for realistic rearrangement schemes[7,8], since two images of the same atom must to be captured on a timescale over which vacuum-induced losses can be neglected. For this, we make use of the narrow $^1S_0 \to {}^3P_1$ transition to cool the atoms inside the tweezer, while we image them with the broad $^1S_0 \to {}^1P_1$ transition. As a first result, we have imaged atoms inside the tweezers by fluorescence imaging via the $^1S_0 \to {}^1P_1$ transition only. One of our first data sets is shown in FIG. 3.

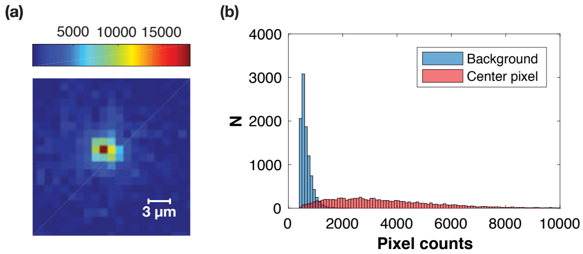

FIG. 3: **(a)** Single shot image of atoms inside the optical tweezer. The color bar shows counts on the EMMCD camera. **(b)** Histogram with pixel counts over 10, 000 realizations of the sequence, where the red bars show the counts of the central pixel of the tweezer compared to the counts of an arbitrary pixel outside of the tweezer in blue.

As a next step, we want to include the 689 nm laser system to test the proposed sideband cooling scheme for non-destructive imaging that allows for rearrangement. This will open up several avenues for new ways to synthesize and probe quantum many-body systems.

---

[1] A. Wallraff, D. I. Schuster, A. Blais, L. Frunzio, R.-S. Huang, J. Majer, S. Kumar, S. M. Girvin, and R. J. Schoelkopf, *Strong coupling of a single photon to a superconducting qubit using circuit quantum electrodynamics*, Nature **431**, 162 (2004).

[2] S. Nadj-Perge, S. Frolov, E. Bakkers, and L. P. Kouwenhoven, *Spin-orbit qubit in a semiconductor nanowire*, Nature **468**, 1084 (2010).

[3] A. Kaufman, B. Lester, M. Foss-Feig, M. Wall, A. Rey, and C. Regal, *Entangling two transportable neutral atoms via local spin exchange*, Nature **527**, 208 (2015).

[4] D. Barredo, H. Labuhn, S. Ravets, T. Lahaye, A. Browaeys, and C. S. Adams, *Coherent excitation transfer in a spin chain of three rydberg atoms*, Physical review letters **114**, 113002 (2015).

[5] N. Schlosser, G. Reymond, I. Protsenko, and P. Grangier, *Sub-poissonian loading of single atoms in a microscopic dipole trap*, Nature a-z index **411**, 1024 (2001).

[6] B. J. Lester, N. Luick, A. M. Kaufman, C. M. Reynolds, and C. A. Regal, *Rapid production of uniformly filled arrays of neutral atoms*, Physical review letters **115**, 073003 (2015).

[7] D. Barredo, S. de Léséleuc, V. Lienhard, T. Lahaye, and A. Browaeys, *An atom-by-atom assembler of defect-free arbitrary two-dimensional atomic arrays*, Science **354**, 1021 (2016).

[8] M. Endres, H. Bernien, A. Keesling, H. Levine, E. R. Anschuetz, A. Krajenbrink, C. Senko, V. Vuletic, M. Greiner, and M. D. Lukin, *Atom-by-atom assembly of defect-free one-dimensional cold atom arrays*, Science p. aah3752 (2016).

[9] H. Bernien, S. Schwartz, A. Keesling, H. Levine, A. Omran, H. Pichler, S. Choi, A. S. Zibrov, M. Endres, M. Greiner, et al., *Probing many-body dynamics on a 51-atom quantum simulator*, Nature **551**, 579 (2017).

[10] M. Takamoto, F.-L. Hong, R. Higashi, and H. Katori, *An optical lattice clock*, Nature **435**, 321 (2005).

[11] Y. Jiang, A. Ludlow, N. D. Lemke, R. W. Fox, J. A. Sherman, L.-S. Ma, and C. W. Oates, *Making optical atomic clocks more stable with 10-16-level laser stabilization*, Nature Photonics **5**, 158 (2011).

Challenges in Design and Fabrication of a Scalable 3D Ion Trap

Maryse Ernzer,[1] Chiara Decaroli,[1] Peter Clements,[1] and Jonathan Home[1]
[1] *Institute of Quantum Electronics, ETH-Hönggerberg, CH-8093, Zürich, Switzerland*

Ion traps are a promising platform for the realization of a quantum computer. In the following, I will discuss the design and fabrication challenges of a novel trap geometry. I will focus on the trap assembly, filter board and the integration of optical elements in the trap structure.

I. INTRODUCTION

Since Shor and Grover's proposal of quantum algorithms, which would improve the computational efficiency for factorization and big data searching[1,2], trapped ions have been proposed as a robust platform for quantum computation[3]. Even though all of the Di Vincenzo criteria are satisfied by trapped ions[4], the scalability requirement still remains unsatisfied[5,6].
One solution to the problem of scalability of ion traps consists in an array-like geometry. This would work as a quantum charged-coupled device (QCCD), where ions are stored in memory areas, manipulated in addressing regions and moved around in two dimensions[7]. For this purpose, one would need precise control over the transport of ions around corners, and has been explored recently by trap geometries implementing T and X shaped junctions[8].

Our design aims to achieve a building block of a QCCD architecture. The trapping region is shaped as a double junction formed by one long leg crossed by two shorter legs, dividing the main axis in three distinct regions, creating independently addressable experimental zones. Novel features of this design are the double junction geometry, the fabrication methods and the optical integration. Following the principle of a Paul trap,[9] ion confinement is generated by electrodes conducting radio-frequency (rf) and dc voltages. The oscillating electric field creates a quadrupole potential, confining the ions radially. The segmented dc electrodes provide the axial confinement and allow transport using time-varying potentials.

II. SCALING CHALLENGES

The realization of this novel trap is very challenging, due to the complexity of its geometry, together with the compactness requirement. Some of the challenges faced are: the design of the trap wafer assembly, to ensure precise alignment and mechanical stability; the design of the signal traces on the trapping wafer and on the filter board, which not only has to accommodate more than 100 signal lines but also has to be very compact; and the integration of the optical delivery within the trap.

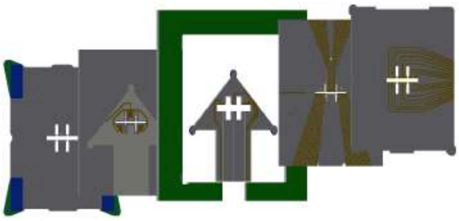

FIG. 1: Exploded view of the total trapping stack: (from left to right) bottom shim wafer, bottom trap electrode wafer, middle wafer aligned with the filter board(green), top trap electrode wafer and top shim wafer

For a three dimensional trap formed by a stack of wafers, the alignment between the different elements is very important. A small tilt or misplacement strongly disturbs the trapped ions. Asymmetries between the electrodes create a residual electric fields on the trap axis leading to excess micromotion of the ion. This issue becomes even more important in a modular scaling approach, where multiple small trapping units would be put together. Previously, alignment in alumina 3D traps relied on screwing the wafers together which introduced misalignments of 10 μm and resulted in excess micromotion.

The design of the segmented dc electrodes is complicated due to the high number of signal lines that have to fit in the geometrically restricted area between the two X junctions. According to the requirements of the QCCD architecture, the electrodes not only have to control the transport in one direction and the splitting of linear chains, but ions have to be moved in two dimensions. There will be 145 electrodes distributed around the double junction. Tracing individual signal lines for each electrode makes the fabrication of this trap more challenging than previous implementations.
To connect the electrodes to the outside, the trapping wafer stack will be wire bonded and glued to a printed circuit board (PCB). The board will contain a low pass RC filter on each dc track in order to clean the signal close to the trap and ground the capacitively coupled rf signals. This means that the filter board has to fit more than 140 track lines including the lumped filter elements.

An additional challenge related to the QCCD structure consists in the parallel manipulation of qubits in different experimental regions. Indeed, ions have to be targeted independently with appropriate laser beams. Especially in the case of a multi-species trap, the number of specific laser beams and correspondingly of bulk optics needed for the the quantum state manipulation and readout in-

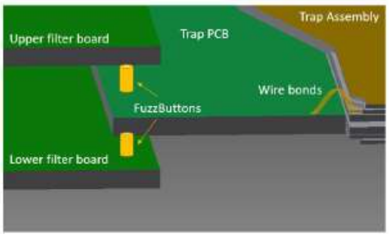

FIG. 2: Modular filter board using Fuzz Buttons

creases with the number of ions and species. In a large quantum computer the integration of optical beams becomes necessary.

III. SCALING SOLUTIONS

We propose several technical solutions to the challenges mentioned in the section above.

To address the scalabilty and precision alignment challenge, the trap is fabricated using the new technology of subtractive 3D printing. It consists of a stack of five silica glass wafers shown in Figure 1. The alignment is provided by features protruding on the wafers, decreasing the misalignment. The wafers will be fixed together using an epoxy with the lowest coefficient of thermal expansion available, low outgassing and a reliable cryogenic performance[10].

To meet the requirements of the double junction and fit the high number of dc electrodes, we use both sides of the trapping electrode wafer, and vias to switch from one side to the other.
For the filter board, we design two different structures: a single PCB holding both the trap and the filters, and a modular PCB design illustrated in Figure 2. The latter is composed by three boards. One board works as a holder for the trap which is directly glued and wire bonded. This trap board is connected on each side to another PCB carrying the actual filters. The connection between the boards will be realized by removable connectors such as Fuzz Buttons or Pogo pin connectors.

To address the challenge of optical delivery, three fibres will be embedded in the trap, one for each experimental zone. The laser beams will be coupled into photonic-crystal fibres. These will have a lensed fibre tip, fabricated by collapsing the capillaries and melting the tip to form a hemispherical lens. The beam after the lens will have a Gaussian shape, focused to a FWHM of 20 μm at a distance of 500μm. It is critical to align and fix the fibres to the wafer stack as they will be glued into rectangular grooves in the middle wafer. The alignment depends on the accuracy of the wafer fabrication but also on the thermal properties of the applied epoxy when it is cooled down to cryogenic temperatures.
When placed into an electric field, the dielectric fibres accumulate charges. The resulting electric field has to be compensated by additional electrodes on the middle wafer. Mirrors reflecting the light provided by the optical fibres out of the trap can be connected and used as electrodes. Furthermore, we are testing different coatings of indium-tin-oxide (ITO). This conductive layer which is up to 90% transparent at the relevant wavelength[11], would electrically shield the fibres and prevent charging effects on the fibre tip surface.

IV. LOOKOUT

Once the design will be completed, several fabrication aspects will be tested. An optimal shadow mask fabrication technique will be found. Different connectors for the filter board will be tested, the fibres will be integrated in the wafer and the trap will be fabricated.

Acknowledgments

We kindly thank QSIT for the INSPIRE Potentials-QSIT Master Internship Award.

---

[1] P. W. Shor, *Polynomial-time algorithms for prime factorization and discrete logarithms on a quantum computer*, SIAM review **41**, 303 (1999).
[2] L. K. Grover, in *Proceedings of the twenty-eighth annual ACM symposium on Theory of computing* (ACM, 1996), pp. 212–219.
[3] J. I. Cirac and P. Zoller, *Quantum computations with cold trapped ions*, Physical review letters **74**, 4091 (1995).
[4] C. Monroe, D. Meekhof, B. King, W. M. Itano, and D. J. Wineland, *Demonstration of a fundamental quantum logic gate*, Physical review letters **75**, 4714 (1995).
[5] D. P. DiVincenzo et al., *The physical implementation of quantum computation*, arXiv preprint quant-ph/0002077 (2000).
[6] C. Monroe and J. Kim, *Scaling the ion trap quantum processor*, Science **339**, 1164 (2013).
[7] D. Kielpinski, C. Monroe, and D. J. Wineland, *Architecture for a large-scale ion-trap quantum computer*, Nature **417**, 709 (2002).
[8] B. Blakestad, Ph.D. thesis, University of Colorado (2010).
[9] W. Paul, *Electromagnetic traps for charged and neutral particles*, Reviews of Modern Physics **62**, 531 (1990).
[10] *EPO-TEK ® T7110 Epoxy.*
[11] L. Davis, *Properties of transparent conducting oxides deposited at room temperature*, Thin Solid Films **236**, 1 (1993).

Characterizing the performance of a superconducting quantum processor

Stefania Balasiu,[1] Christian Kraglund Andersen,[1] Johannes Heinsoo,[1] Ants Remm,[1] Sebastian Krinner,[1] Christopher Eichler,[1] and Andreas Wallraff[1]
[1] *Department of Physics, ETH-Hönggerberg, CH-8093, Zürich, Switzerland*

Superconducting quantum processors are used extensively in state-of-the-art research in quantum computing due to their good coherence properties, the high-fidelity readout schemes, and the flexibility in scaling up to larger architectures. Here, we measure the single qubit gate performance in an 8 superconducting qubit processor using a technique called randomized benchmarking.

I. INTRODUCTION

Superconducting quantum processors are prime candidates for implementing the next steps in quantum computing research, such as fault-tolerant quantum error corrections schemes based on the surface code[1], and applications with noisy intermediate scale quantum computers[2]. Recent results[3] have shown that coherence times higher than 100 μs can be achieved with superconducting qubits, as well as single- an two-qubit average gate errors below 0.5% and 1%, respectively. Moreover, high-fidelity, fast multiplexed readout of up to 5 qubits has recently been achieved with errors below 2%[4].

To scale up any quantum processor, its algorithmic performance must be characterized and the coherent errors (due to qubit control) and incoherent errors (due to decoherence and qubit-qubit interactions) must be reduced[5]. One characterization technique is called randomized benchmarking (RB), and it has been used extensively to quantify the performance of single- and two-qubit gates[3,6], as well as the amount of correlated errors in multi-qubit algorithms and the scalability of single-qubit errors with the number of qubits in the algorithm[7].

II. QUANTUM COMPUTING WITH SUPERCONDUCTING QUBITS

A basic unit of an 8 superconducting qubit quantum processor is shown in Fig. 1. A qubit is capacitively coupled to a *readout resonator*, which is used to obtain information about the state of the qubit. The two *coupling resonators* are used to connect this qubit to its neighbors, which are not shown here. The state of the qubit is manipulated with microwave pulses sent via the *drive line.*

A zoom-in of the structure that forms the qubit is shown in Fig. 1 (b). This quantum bit (qubit) is called a *transmon* and it is formed from a non-linear superconducting quantum interference device (SQUID) loop in parallel with a capacitor (red cross). An external magnetic flux is applied through this loop to tune the frequency of the transmon via the *flux line.* This circuit creates an anharmonic oscillator[8] whose potential energy diagram as a function of the externally applied magnetic flux Φ is schematically shown in (c) (green). The transmon is similar to a Hydrogen atom, whose quantized energy levels, also shown in (c) (black), become closer together at higher energies. We can choose to access only the first energy transition of this system between the levels E_1 and E_0, which define our *computational basis states* $|0\rangle$ and $|1\rangle$ corresponding to the qubit ground and excited states.

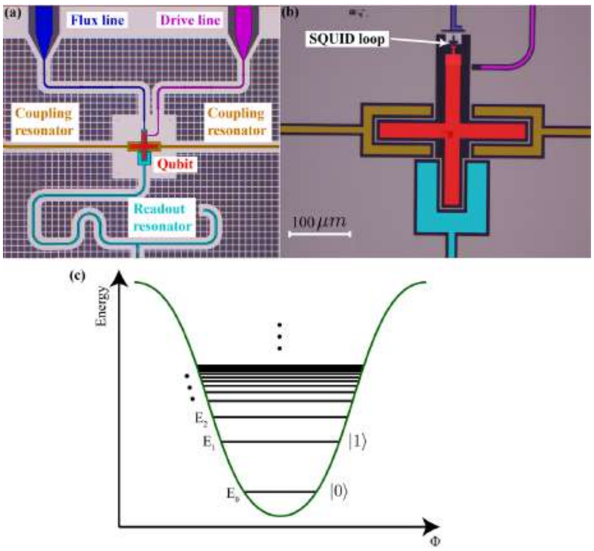

FIG. 1: Basic architecture of a quantum computer with superconducting qubits.

The readout resonator is used to perform *quantum non-demolition* (QND) measurements, which preserve the qubit state even after it was measured. To this end, the transmon-resonator system is placed in the *dispersive regime*, where the transmon frequency $\omega_{qb} = (E_1 - E_0)/\hbar$ is far detuned from the resonator frequency ω_r. The Hamiltonian describing the system in this regime is[8]:

$$\hat{H}_{\text{dispersive}} = \frac{\hbar(\omega_{qb} + \chi)}{2}\hat{\sigma}_z + \hbar(\omega_r + \chi\hat{\sigma}_z)\hat{a}^\dagger\hat{a}, \quad (1)$$

where $\hat{\sigma}_z$ is the Pauli Z operator, and $\hat{a}^\dagger$ ($\hat{a}$) create (annihilate) an excitation in the resonator. The first term describes the energy of the transmon with frequency $\omega_{qb}+\chi$, and the second term describes the resonator with its frequency renormalized to $\omega_r + \chi\hat{\sigma}_z$. The state of the resonator changes with the state of the qubit (captured by $\hat{\sigma}_z$) in a manner quantified by the proportionality term

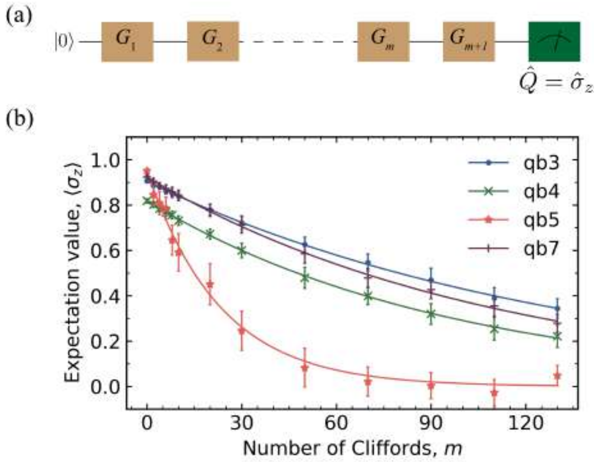

FIG. 2: Measurement results from RB on qubits 3, 4, 5, 7.

χ. Thus we can measure the response of the resonator to obtain information about our quantum bit.

III. CHARACTERIZING QUANTUM GATE PERFORMANCE WITH RB

The single qubit RB experiment is used to characterize the average error of single qubit gates. The RB measurement protocol is shown in Fig. 2 (a) and contains the following steps[6]: (1) Choose a sequence length m from a set of sequence lengths M. (2) Generate m random gates $\{G_i\}_{i\in[1,m]}$ sampled uniformly from the single qubit group of Clifford gates, C_1, and the inverse of these gates $G_{m+1} = (G_m...G_1)^\dagger$. (3) Prepare the qubit in $|0\rangle$, apply the sequence $G_{m+1}G_m...G_1$, and measure the $\hat{\sigma}_z$ operator. (4) Repeat step 3 a large number of times N ($N > 2^{10}$) and average all results to obtain the expectation value $\langle\hat{\sigma}_z\rangle$. (5) Repeat steps 2-4 K times and average all the K values of $\langle\hat{\sigma}_z\rangle$. (6) Repeat steps 2-5 for all sequence lengths $m \in M$. This protocol introduces more errors on the qubit as m gets larger. Thus, $\langle\hat{\sigma}_z\rangle$ as a function of m gives an exponential decay towards a state of the qubit where it has completely lost all useful information. Fig. 2 (b) shows these decays from RB on the four qubits indicated in the legend. From fits to these decays we extract the decay strength constants, α_1, and calculate the average error per applied Clifford element as $r_1 = (1-\alpha_1)/2^6$. We find average errors below 1% for all qubits except for qubit 5, which had $r_1 \simeq 2\%$ mainly due to its low coherence times.

IV. OUTLOOK

To use our 8 superconducting qubit processor for quantum error correction codes, our immediate goal is to improve our average single-qubit gate errors to values below 0.1%. The next steps in characterizing our processor is to implement this RB protocol on multiple qubits simultaneously in order to gain information about how r_1 scales with the number of simultaneously operated qubits, and to quantify the amount of correlated errors in our algorithms. If these sources of error are significant, they must be overcome in order to successfully implement quantum information protocols.

Acknowledgments

We acknowledge financial support from IARPA, ODNI, NCCR QSIT, and ETH Zürich.

---

[1] R. Barends, J. Kelly, A. Megrant, A. Veitia, D. Sank, E. Jeffrey, T. C. White, J. Mutus, A. G. Fowler, B. Campbell, et al., *Superconducting quantum circuits at the surface code threshold for fault tolerance*, Nature **508**, 500 (2014), ISSN 0028-0836, URL `http://www.nature.com/nature/journal/v508/n7497/full/nature13171.html`.

[2] J. Preskill, *Quantum computing in the nisq era and beyond*, arXiv:1801.00862 (2018), URL `https://arxiv.org/abs/1801.00862`.

[3] S. Sheldon, E. Magesan, J. M. Chow, and J. M. Gambetta, *Procedure for systematically tuning up cross-talk in the cross-resonance gate*, Phys. Rev. A **93**, 060302 (2016), URL `http://link.aps.org/doi/10.1103/PhysRevA.93.060302`.

[4] J. Heinsoo, C. K. Andersen, S. K. A. Remm, T. Walter, Y. Salathé, S. Gasparinetti, J.-C. Besse, A. Potočnik, C. Eichler, and A. Wallraff, *Rapid high-fidelity multiplexed readout of superconducting qubits*, ArXiv e-prints (2018), URL `https://arxiv.org/abs/1801.07904`.

[5] A. G. Fowler, M. Mariantoni, J. M. Martinis, and A. N. Cleland, *Surface codes: Towards practical large-scale quantum computation*, Phys. Rev. A **86**, 032324 (2012), URL `https://link.aps.org/doi/10.1103/PhysRevA.86.032324`.

[6] J. M. Epstein, A. W. Cross, E. Magesan, and J. M. Gambetta, *Investigating the limits of randomized benchmarking protocols*, Phys. Rev. A **89**, 062321 (2014), URL `https://journals.aps.org/pra/abstract/10.1103/PhysRevA.89.062321`.

[7] J. M. Gambetta, A. D. Córcoles, S. T. Merkel, B. R. Johnson, J. A. Smolin, J. M. Chow, C. A. Ryan, C. Rigetti, S. Poletto, T. A. Ohki, et al., *Characterization of addressability by simultaneous randomized benchmarking*, Phys. Rev. Lett. **109**, 240504 (2012), URL `http://link.aps.org/doi/10.1103/PhysRevLett.109.240504`.

[8] J. Koch, T. M. Yu, J. Gambetta, A. A. Houck, D. I. Schuster, J. Majer, A. Blais, M. H. Devoret, S. M. Girvin, and R. J. Schoelkopf, *Charge-insensitive qubit design derived from the Cooper pair box*, Phys. Rev. A **76**, 042319 (2007), URL `http://link.aps.org/abstract/PRA/v76/e042319`.

Coupled Waveguides for Dispersion Compensation in THz Frequency Combs based on Quantum Cascade Lasers

Urban Senica,[1] Jérôme Faist,[1] and Giacomo Scalari[1]
[1]Institute of Quantum Electronics, ETH-Hönggerberg, CH-8093, Zürich, Switzerland

Quantum Cascade Lasers are based on intersubband trasitions and can be tuned over a broad frequency range in the mid-IR and THz. Their use has recently been extended to frequency combs, which act as rulers in the frequency domain. A major limiting factor in achieving broadband operation, crucial for QCL-based combs, is group velocity dispersion (GVD). Previous results and preliminary simulations indicate that GVD can be compensated via a system of coupled waveguides, as the (anti)symmetric modes show a different frequency dependence of the group index.

I. INTRODUCTION

A. QCLs & Frequency Combs

First demonstrated in 1994, the Quantum Cascade Laser[1] (QCL) was a pioneering experimental discovery utilizing *intersubband transitions*. In essence, its operation is based on optical transitions between electronic states inside the conduction band, which are formed as a consequence of spatial confinement in multi quantum wells. One of the main advantages of QCLs is that their emission wavelength can be tuned over a broad frequency range, spanning the mid-IR and THz, by changing the quantum wells' width despite using the same material system.

Over the last few years, the use of QCLs has been extended to *frequency combs*, with their equidistantly spaced modes spanning a broad frequency range. The modes at frequencies f_n can be expressed as

$$f_n = f_\mathrm{ceo} + n f_\mathrm{rep} \tag{1}$$

which means the modes are spaced by the repetition rate f_rep, while the whole ensemble of modes is usually shifted by the carrier-envelope offset frequency f_ceo. In contrast to an array of single-mode lasers, the line-to-line frequency noise is correlated, meaning the linewidth of the beating between individual modes may be much smaller than that of the individual lines. This enables the use of *self-referencing*[2,3] - if the comb is spanning at least an octave, the f_ceo can be directly retrieved and stabilized. This is achieved by beating the second harmonic of a line in the lower portion of the spectrum with a line in the high frequency end. Consequently, the absolute frequency of each line is linked to f_rep, enabling the comb to act as a ruler in the frequency domain.

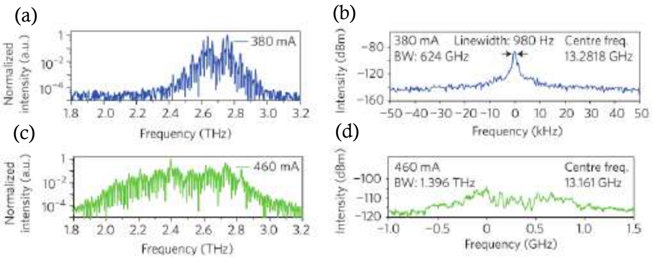

FIG. 1: Spectra of an octave spanning heterogeneous quantum cascade structure, as published in[4]. **(a)** and **(b)** display a brodband spectrum and a narrow beatnote in the comb regime. As shown in **(c)** and **(d)**, the laser does not operate as a comb unless an appropriate bias current is applied.

B. Group Velocity Dispersion

A necessary condition for QCL-based frequency combs is broadband operation, as shown in Fig. 1. A major limiting factor is *group velocity dispersion* (GVD), i.e., a change of the group refractive index n_g with frequency:

$$GVD = \frac{\partial}{\partial \omega}\left(\frac{1}{v_g}\right) = \frac{1}{c}\,\frac{\partial n_g}{\partial \omega} \tag{2}$$

There are several contributions to GVD, including material dispersion, gain dispersion and waveguide dispersion.

II. COUPLED WAVEGUIDES

A. Concept

We focus on minimizing waveguide dispersion. In the THz, a metal-metal waveguide is usually used, and a simple waveguide design often introduces (undesired) positive GVD, as shown in Fig. 2. One possible approach to minimize waveguide GVD is by using a double-chirped mirror (DCM) architecture by varying the waveguide width[5]. A two waveguide geometry can also be considered: if the waveguides are positioned close enough for the optical modes to overlap, we get a system of *coupled waveguides*. It is then possible to tune dispersion by changing the waveguides' coupling strength. In essence, we get *symmetric* and *antisymmetric* modes with different group indices $n_g(\omega)$ and consequently a modified GVD.

The task is to find a suitable geometrical arrangement of waveguides whose optimal dimensions need to be considered as well. This has already been demonstrated in

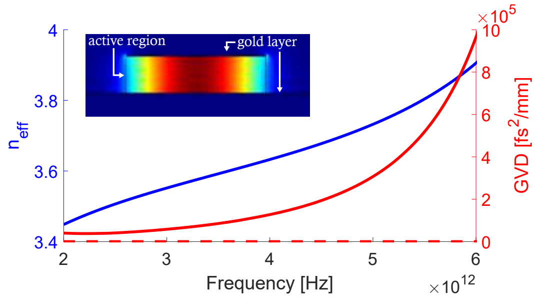

FIG. 2: Simulated effective refractive index n_{eff} and GVD for a metal-metal waveguide with dimensions (50×13) μm^2. Inset shows the electric field norm $|\mathbf{E}|$ across the waveguide cross-section at 3 THz.

the mid-IR, where coupled buried waveguides have been used[6]. To ensure that the desired antisymmetrical mode was the one lasing in experiment, one of the waveguides was passive, i.e., without a gain region.

B. Preliminary Simulation Results

As there is hardly any mode leakage around a metal-metal waveguide in the vertical direction, we consider a side-by-side waveguide placement and use eigenmode simulations. For the metal (gold) layers data from Ordal et al.[7] were used, while for the GaAs a model including optical phonons was implemented:

$$\varepsilon_r(GaAs) = \varepsilon_\infty + (\varepsilon_{DC} - \varepsilon_\infty) \cdot \frac{\Omega_{T0}^2}{\Omega_{T0}^2 - \omega^2 - i\Gamma_{TO}\omega} \quad (3)$$

with parameter values $\varepsilon_{DC} = 12.90$, $\varepsilon_\infty = 10.89$, $\Omega_{T0} = 268.7\ \mathrm{cm}^{-1}$ and $\Gamma_{TO} = 2.4\ \mathrm{cm}^{-1}$. A fundamental mode study implies that the waveguides need to be separated by only a few microns. Results of an example eigenmode simulation of two coupled waveguides placed 2 μm apart at a frequency of 3 THz are shown in Fig. 3.

Preliminary results of different air gap widths across a broad range of frequencies in the THz show that, much like in the aforementioned mid-IR case, we can modify GVD by essentially ”splitting” the group index frequency dependency of a single waveguide into two branches (for the symmetric and antisymmetric modes). To achieve a minimum GVD, an optimized structure which promotes the desired (anti)symmetric mode needs to be identified.

III. OUTLOOK

Besides finding an optimal waveguide arrangement, i.e., a configuration of coupled waveguides which yields a minimum GVD across a broad range of frequencies, the logical next step is to implement these structures and characterize them in the lab. Prior to experiments one also needs to consider the limitations of nanofabrication techniques. Preliminary simulation results suggest that the required precision is in the order of microns, which is attainable with current deep dry etching techniques.

Acknowledgments

We would like to thank QSIT and the ERC Consolidator Grant ”on-CHip thz frequency Combs (CHIC)”.

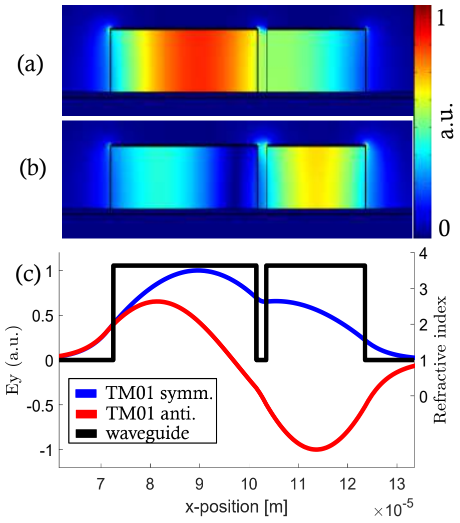

FIG. 3: COMSOL 2D eigenmode simulation results for coupled waveguides with dimensions (30×13) μm^2 and (20×13) μm^2, separated by a 2 μm wide air gap, at 3 THz. Electric field norm $|\mathbf{E}|$ across the waveguides cross-section is shown for **(a)** the TM01 *symmetric mode* and **(b)** the TM01 *antisymmetric* mode. **(c)** Vertical electric field component (E_y) along a horizontal x-cut line through the center of both waveguides. Refractive index is outlined in black.

---

[1] J. Faist et al., *Quantum Cascade Laser*, Science **264**, 553 (1994).

[2] D. J. Jones et al., Science **288**, 635 (2000).

[3] S. A. Diddams et al., Physical Review Letters **84**, 5102 (2000).

[4] M. Rösch et al., *Octave-spanning semiconductor laser*, Nature Photonics **9**, 42 (2015).

[5] D. Burghoff et al., *Terahertz laser frequency combs*, Nature Photonics **8** (2014).

[6] Y. Bidaux et al., *Coupled-Waveguides for Dispersion Compensation in Semiconductor Lasers*, Laser & Photonics Reviews p. 1700323 (2018).

[7] M. A. Ordal et al., *Optical properties of Au, Ni, and Pb at submillimeter wavelengths*, Applied Optics **26**, 744 (1987).

Coupling superconducting high impedance resonators to quantum dot qubits

Benedikt Kratochwil,[1] Andreas Landig,[1] Jonne Koski,[1] Mihai Gabureac,[1] Pasquale Scarlino,[1]
Christian Reichl,[1] Werner Wegscheider,[1] Andreas Wallraff,[1] Thomas Ihn,[1] and Klaus Ensslin[1]
[1] *Laboratory for Solid State Physics, ETH-Hönggerberg, CH-8093, Zürich, Switzerland*

Electron spins are promising candidates for quantum computation due to their long coherence times. A crucial step for quantum information processing is the ability to mediate long range interactions between distant qubits by using photons as carriers of quantum information. Recently, we achieved strong coupling of a spin qubit in a GaAs triple quantum dot with single microwave photons[1]. To enhance the qubit-photon coupling strength, the photons are stored in a cavity with a high characteristic impedance fabricated from a thin film of NbTiN. To couple two distant spin qubits coherently, current work focuses on improving both the qubit-photon coupling strength and the resonator linewidth by material optimization of NbTiN.

I. INTRODUCTION

There are two key ingredients to achieve practical quantum computation. The first is a long coherence time of an individual qubit, and the second is an ability to transfer information between distant qubits[2]. Promising candidates for long coherence times are semiconductor spin qubits[3,4]. To transfer quantum information over long distances, we follow a quantum electrodynamics approach by coupling the qubit to the microwave photons stored in a superconducting resonator. The coupling strength between an electron spin and a resonator photon is orders of magnitude smaller than in other qubit implementations such as charge qubits or superconducting qubits[5]. Thus reaching the strong coupling regime between spin qubit and resonator photons is challenging. There are different approaches to enhance coupling strength, which rely on admixing charge character to the spin states[6–8]. Relying on exchange interaction, we achieved strong spin-photon coupling with a resonant exchange qubit that is formed by three electrons in a triple quantum dot[1]. A key ingredient of this quantum device is a high impedance resonator. Here we present the current resonator implementation and show first steps towards improving the resonator for coupling of distant spin qubits in the future.

II. PREVIOUS WORK

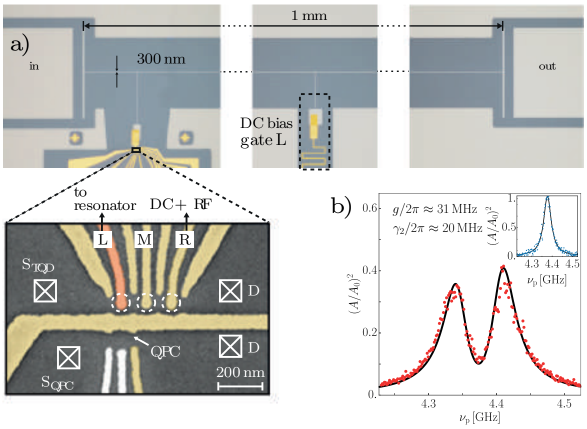

FIG. 1: Optical micrograph of the resonator and a false color scanning electron micrograph of the gate structure of the qubit in a). Normalized resonator transmission as a function of resonator probe frequency in the uncoupled (inset of b)) and the coupled configuration. The measurement in the coupled configuration shows a vacuum Rabi splitting due to the strong coupling of spin and photon.

In recent work we reported strong coupling of single photons in a high impedance superconducting NbTiN resonator and a gate defined three electron spin qubit[1]. The device that realized strong spin-photon coupling is shown in Fig 1a. It shows an optical micrograph picture of the resonator and a scanning electron micrograph zoom in of the gate structure. The resonator has a coplanar wave guide design with a 1 mm long and 300 nm wide central conductor strip defined on a 15 nm thin NbTiN film. The resonator transmission with the qubit far detuned is shown in the inset of Fig. 1b. and shows a single peak in transmission at the resonance frequency. By a fit we determine the resonator frequency $\nu_r = 4.3\,\mathrm{GHz}$ and the linewidth $\kappa/2\pi = 47.1\,\mathrm{MHz}$. The resonator is capacitively coupled to the quantum dot structure via the left plunger gate (see gate line marked in orange in Fig 1a). The coupling strength g between the resonator photons and the qubit scales with $\sqrt{Z_r}$[9,10]. Thus the resonator was designed to have a high characteristic impedance of $Z_r \cong 1.3\,\mathrm{k\Omega}$, more than one order of magnitude above the impedance of a standard $50\,\Omega$ resonator.

The triple quantum dot structure and a quantum point contact used for charge sensing are formed in a GaAs/AlGaAs heterostructure. The triple quantum dot is operated in the three electron regime and coupled to a single photon in the resonator. As the focus of this work is about the resonator structure we refer to[1] for detailed information about the qubit implementation.

The key signature of strong coupling of the qubit-photon system is the splitting of the resonator resonance when the qubit energy is tuned to match the resonator energy, also known as the vacuum Rabi mode splitting. The transmission spectrum for this configuration is shown in Fig. 1b. The data points are fit with an input output theory model[11] from which we extract a coupling strength of $g/2\pi \cong 31\,\mathrm{MHz}$ and a qubit decoherence rate of $\gamma_2/2\pi = 20\,\mathrm{MHz}$.

III. ONGOING WORK

To establish coupling of two distant spin qubits in the experiment we couple the two qubits to the same resonator acting as a quantum bus. This introduces a mutual qubit-qubit coupling strength J, which is given as[12]:

$$J = \frac{g_1 g_2}{2}\left(\frac{1}{\Delta_1} + \frac{1}{\Delta_2}\right), \tag{1}$$

where g_x and Δ_x with $x \in \{1, 2\}$ is the coupling strength and detuning of qubit x from the resonator frequency. Thus we aim for high individual coupling strengths g_x as well as a small linewidth of the resonator. The coupling strength can be increased by maximizing the characteristic impedance $Z_r = \sqrt{L_l/C_l}$ of the films, which is given by the ratio of resonator inductance L_l and capacitance per unit length C_l. For NbTiN, the inductance is divided into two contributions. The first is geometric inductance, which is determined by the dimensions of the resonator, and the second is the kinetic inductance arising from the inertia of moving cooper pairs in NbTiN. The kinetic inductance L_k is proportional to $R_\square$[13]. Therefore controlling the sheet resistance is a natural way to control the kinetic inductance. By changing the partial pressure of N_2 during the sputtering process we are able change the disorder of the deposited film and thus control the sheet resistance $R_\square$. From the measurements of $R_\square$ and the superconductor critical temperature T_C, the kinetic Inductance L_K can be calculated as[13].

$$L_K = \frac{R_\square h}{2\pi^2\Delta}\frac{1}{\tanh\left(\frac{\Delta}{2k_BT}\right)} \tag{2}$$

where T is the temperature, and Δ is the superconducting energy gap, which we estimate as $\Delta = 1.76k_BT_c$[14].

In table 1. we list the critical Temperature T_C, the sheet resistance $R_\square$ measured at 300 K,the calculated kinetic inductance at 4.2 K, and the thickness d of the NbTiN films grown on bare GaAs. If the partial pressure of N_2 is too high, as is the case for sample 4, the sample is not superconducting at liquid helium temperatures. For sample 3, the kinetic inductance is over 50 % higher compared with to the film used in[1].

TABLE I: Characteristic parameters of the different 10 nm to 15 nm NbTiN films sputtered on bare GaAs. The used Argon pressure is increased from top to bottom

Sample Nr.	T_C in K	$R_\square$ in $\Omega/\square$	L_K in pH/$\square$	d in nm
1	11.3	105	13	15
2	8.9	128	21	15
3	9.0	406	65	10
4	–	1882	–	15

IV. OUTLOOK

The future goal is to couple two distant spin qubits via the resonator. As we now have films with a higher kinetic inductance, the next step is to improve the resonator linewidth by optimizing the resonator geometry and improving the recipes for fabrication.

Acknowledgments

This work was supported by the Swiss Nation Science Foundation through the National Center of Competence in Research (NCCR) Quantum Science and Technology.

---

[1] A. J. Landig et al. (2017), 1711.01932.
[2] D. P. DiVincenzo, Fortschr. Phys. **48**, 771 (2000).
[3] R. Hanson et al., Reviews of Modern Physics **79**, 1217 (2007), 0610433.
[4] F. A. Zwanenburg et al., Reviews of Modern Physics **85**, 961 (2013), arXiv:1206.5202v1.
[5] R. J. Schoelkopf et al., Nature **451**, 664 (2008).
[6] K. D. Petersson et al., Nature **490**, 380 (2012), 1205.6767.
[7] J. J. Viennot et al., Science **349** (2015).
[8] M. Pioro-Ladrière et al., Nature Physics **4**, 776 (2008), 0805.1083.
[9] A. Stockklauser et al., Physical Review X **7** (2017), 1701.03433.
[10] M. Devoret et al., Ann. Phys. (Leipzig) **1611**, 767 (2007).
[11] M. J. Collett et al., Physical Review A **30**, 1386 (1984).
[12] J. Majer et al., Nature **449**, 443 (2007), 0709.2135.
[13] A. J. Annunziata et al., Nanotechnology **21** (2010), 1007.4187.
[14] M. Tinkham, *Introduction to Superconductivity 2nd edition* (1996).

Development of Hybrid Quantum Dot-Cold Atom Quantum System

Liang Zhai,[1] Jan-Philipp Jahn,[1] Janik Wolters,[1] Gianni Buser,[1]
Lucas Béguin,[1] Philipp Treutlein,[1] and Richard J. Warburton[1]
[1] *Department of Physics, University of Basel, Klingelbergstrasse 82, CH-4056 Basel, Switzerland*

We propose a best-of-both-worlds quantum hybrid system consisting of a source of single-photons based on a GaAs quantum dot and an atomic vapor quantum memory. We demonstrate a quantum memory on ^{87}Rb D_1 line with an internal efficiency of 17(3)% for 50 ns storage time. We generate single-photons frequency matched to Rb transitions with lifetime-limited transitions. The frequency and bandwidth of single-photons can be further optimized by strain tuning and single-photon shaping technique to achieve an efficient source-memory interface.

I. INTRODUCTION

The realization of a truly quantum network[1] would provide manifold opportunities across a range of scientific and technological frontiers, the most well-known being quantum key distribution[2], a cryptography method which promises unconditional security in data communication. The quantum network will almost certainly rely on quantum repeaters[3,4] to achieve long-distance transmission of quantum information. The quantum repeater is a device that allows end-to-end transmission of qubits based on quantum swapping. The single-photon source and the quantum memory are two major components for a quantum-repeater architecture: the single-photon source generates single-photons that serve as carriers of quantum information, while the quantum memory allows on-demand storage and retrieval of the quantum state of light.

These two components can be based on different quantum platforms and therefore be individually optimised. For the single-photon source, semiconductor quantum dots (QDs) are currently the most promising candidates[5] as they outperform other emitters regarding stability, brightness, single-photon purity as well as indistinguishablility. Moreover, the technology by which QDs can be embedded within semiconductor devices for nanophotonics engineering has matured significantly in recent years[6], making the QD platform very attractive for photonic quantum communication. For the quantum memory, warm vapor cells containing Rubidium atoms (Rb) are of particular interest. Such a memory requires neither advanced experimental technique such as laser cooling and atom traps, nor a cryogenic operation temperature, both of which may hinder practical applications of the memory[7]. Our proposal aims at combining these two different systems in a hybrid solution to build a quantum memory for single-photons, which is a first step towards the realization of a quantum repeater.

II. ATOMIC QUANTUM MEMORY

Our vapor cell memory is proposed and implemented on the ^{87}Rb D_1 line at 795 nm by employing electromagnetically induced transparency (EIT) scheme. The energy levels and relevant transitions of the ^{87}Rb D_1 line are shown in Fig. 1(a). The memory is first initialized by optical pumping, preparing all atoms in $F = 1$ hyperfine state in the $5^2S_{1/2}$ ground state. The control laser and signal pulses, which are both detuned from $F = 1$ by $\Delta = 2\pi \cdot 0.9$ GHz, are combined on a polarizing beam splitter (PBS) and sent to the vapor cell, see Fig. 1(c). The signal, which is deliberately attenuated to an intensity where on average each pulse contains only one photon, can then be stored in the warm Rb vapor, the temperature of which is carefully adjusted to achieve an optical depth of OD = 5. The FWHM bandwidth of the signal pulses is measured to be 0.66 GHz. After a storage period of 50 ns, a second identical control laser is sent in and the stored information can be retrieved. The signal pulses are separated from the strong control laser pulses by polarization, spatial as well as spectral filtering, and detected with a single-photon counting APD. By comparing the intensity of storage and retrieval pulses and

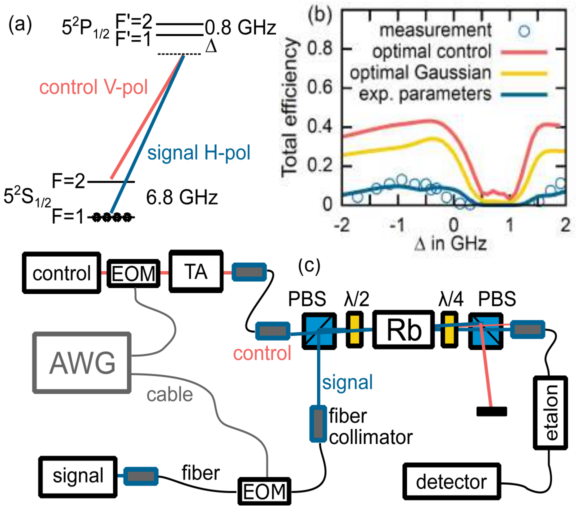

FIG. 1: (a) Level schemes of the ^{87}Rb D_1 line and relevant transitions. (b) The simulated internal efficiency of storage and retrieval of the memory as a function of detuning for various conditions (color lines) and measured date (blue circles). (c) Experimental setup for the memory. EOM: electro-optic modulator; AWG: arbitrary waveform generator; TA: tapered amplifier.

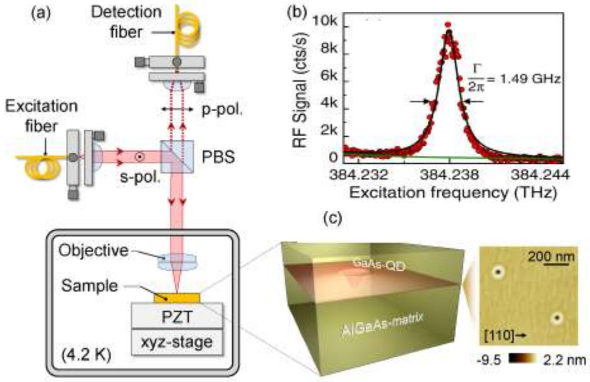

FIG. 2: (a) Schematics of the resonance fluorescence setup.(b) Resonance fluorescence spectrum for a charge exciton in the low power regime. (c) Sketch of the QD layer and an AFM picture of the nanoholes obtained with in situ etching.

correcting for loss in the system, we arrive at a total internal memory efficiency $\eta_{int} = 17(3)\%$ and a signal to noise ratio of $SNR = 3.7$. As shown in Fig. 1(b), this measured internal efficiency matches very well the predicted values computed for the experimental parameters. According to the simulation, the efficiency of our memory can be improved further to $\eta_{int} = 43\%$ by using Gaussian control pulses with higher laser power.

III. SINGLE-PHOTON SOURCE BASED ON DROPLET QUANTUM DOTS

Since the acceptance bandwidth of our atomic quantum memory is limited to a sub-GHz value[7], a key challenge for interfacing single-photon source with the vapor cell memory is to create a high flux of narrow linewidth single-photons from a quantum dot spectrally matched to ^{87}Rb atoms. GaAs QDs fabricated by droplet etching[8] (see Fig.2(c)) or droplet epitaxy[9] can emit single-photons at wavelengths close to ^{87}Rb D_1 line[10]. As shown in Fig. 2(a), the QD sample is bonded onto a piezo device made of lead zirconate titanate (PZT) and cooled down to liquid helium temperature. By applying uniaxial strain on QDs, the emission wavelength can be finely tuned to address the desired transition. The QD signal is separated from the excitation laser and sent to a spectrometer by making use of polarization-based dark-field microscope[11] sketched in Fig. 2(a), allowing us to perform resonant fluorescence of the QD. We sweep the laser frequency across the resonance of the charged exciton, the fluorescence intensity of which is recorded in Fig. 2(b) as a function of excitation frequency. With this result, we deduce a linewidth of 1.49 GHz, which is very close to the lifetime-limit.

The linewidth of the QD photons and their temporal shape can be further tailored based on a single-photon shaping technique. On application of a magnetic field along the QD's growth direction, we lift the degeneracy of the hole spin ground state $|\Uparrow\rangle_z$ and $|\Downarrow\rangle_z$ as well as the degeneracy of trions $|\Uparrow\Downarrow\uparrow\rangle_z$ and $|\Uparrow\Downarrow\downarrow\rangle_z$. Due to the heavy hole - light hole mixing, the two "diagonal" transitions are weakly allowed, making it possible for us to initialize the system into one of the spin ground states by driving one of the strong spin-preserving transitions. After this initialization, single Raman photons can be generated by pumping the spin-flipping transition, the waveform of which follows the control laser's pulse shape. By implementing this idea, we observe Raman photons with Guassian profile and a linewidth as low as around 200 MHz, an order of magnitude narrower than their natural linewidth.

---

[1] H. J. Kimble, *The quantum internet*, Nature **453**, 1023 (2008).

[2] N. Gisin, G. Ribordy, W. Tittel, and H. Zbinden, *Quantum cryptography*, Rev. Mod. Phys. **74**, 145 (2002).

[3] N. Sangouard, C. Simon, H. de Riedmatten, and N. Gisin, *Quantum repeaters based on atomic ensembles and linear optics*, Rev. Mod. Phys. **83**, 33 (2011).

[4] C. Simon, *Towards a global quantum network*, Nat. Photon. **11**, 678 (2017).

[5] G. Kiransk, H. Thyrrestrup, R. S. Daveau, C. L. Dreeen, T. Pregnolato, L. Midolo, P. Tighineanu, A. Javadi, S. S.tobbe, R. Schott, et al., *Indistinguishable and efficient single photons from a quantum dot in a planar nanobeam waveguide*, Phys. Rev. B **96**, 165306 (2017).

[6] P. Lodahl, S. Mahmoodian, and S. Stobbe, *Interfacing single photons and single quantum dots with photonic nanostructures*, Rev. Mod. Phys. **87**, 347 (2015).

[7] J. Wolters and G. Buser and A. Horsley and L. Béguin and A. Jöckel and J.-P. Jahn and R. J. Warburton and P Treutlein, *Simple atomic quantum memory suitable for semiconductor quantum dot single photons*, Phys. Rev. Lett. **119**, 060502 (2017).

[8] A. Stemmann and Ch. Heyn and T. Köppen and T. Kipp and W. Hansen, *Local droplet etching of nanoholes and rings on gaas and algaas surfaces*, Appl. Phys. Lett. **93**, 123108 (2008).

[9] C. Heyn, A. Stemmann, A. Schramm, H. Welsch, W. Hansen, and Á. Nemcsics, *Regimes of gaas quantum dot self-assembly by droplet epitaxy*, Phys. Rev. B **76**, 075317 (2007).

[10] J.-P. Jahn and M. Munsch and L. Béguin and A. V Kuhlmann and M. Renggli and Y. Huo and F. Ding and R. Trotta and M. Reindl and O. G Schmidt and A. Rastelli and P. Treutlein and R. J. Warburton, *An artificial Rb atom in a semiconductor with lifetime-limited linewidth*, Phys. Rev. B **92**, 245439 (2015).

[11] A. V. Kuhlmann et al, *A dark-field microscope for background-free detection of resonance fluorescence from single semiconductor quantum dots operating in a set-and-forget mode*, Rev. Sci. Instr. **84**, 073905 (2013).

Dynamical Casimir effect in an ultrastrongly coupled hybrid optomechanical system

K. Seibold,[1] H. Flayac,[1] and V. Savona[1]
[1] *Institute Physics (iPHYS), École Polytechnique Fédérale de Lausanne EPFL, CH-1015 Lausanne, Switzerland*

We investigate a dissipative tripartite atom-cavity-optomechanical system. We focus on a configuration where the two-level system ultrastrongly couples to the cavity mode, while the mechanical part interacts with the confined electromagnetic field via the standard optomechanical coupling. We explore the nontrivial ground state structure of such a hybrid system, which happens to host a coherent phonon population. While these populations remain virtual and are therefore not directly detectable in a particle-counting experiment, our work shows the possibility to extract real and coherent excitations from the mechanical mode through a non-adiabatical quench of the atom-cavity interaction.

I. INTRODUCTION

Cavity quantum electrodynamics explores the light-matter interaction at its fundamental level. In the strong coupling regime, the quantum emitter absorbs and spontaneously reemits photons several times before the excitation leaks into the environment. Beyond this paradigm, a regime called *ultrastrong* coupling[1,2] has recently drawn the attention on both theoretical and experimental sides. The ultrastrong coupling regime (USCr) emerges when the light-matter coupling strength becomes comparable to the bare emitter and cavity resonance frequencies. The study of ultrastrongly coupled atom-cavity setups is particularly interesting due to numerous novel and unconventional quantum phenomena. In the past decade this field of research as benefited from a great boost due to experimental realizations in different solid state and superconducting systems. In the strong coupling regime, a good approximation consists in making the rotating wave approximation, i.e. neglecting counter rotating terms. In the USCr, however, these terms must be taken into account. A key feature arising in ultrastrongly coupled setups is the determinant role of virtual particles that happen to spread over the ground and excited states. When studying an ultrastrongly coupled system, the standard tools such as the particle number operators or the statistical functions must therefore be reconsidered.

Besides, in the past few years, the field of cavity optomechanical systems has attracted wide interests. In these systems a mechanical mode couples via radiation pressure to the confined light in a cavity. Due to their entirely novel features and functionalities, hybrid optomechanical systems have been extensively studied in the past decade in electrical, microwave or optical systems

In the present work, we study the possibility of producing a nonzero population of real phonons in the steady-state of the tripartite system by *indirect dynamical Casimir effect* i.e. the nonadiabatic modulation of the ultrastrong light-matter coupling to produces real phonons through the mechanical coupling.

In my talk, I will first introduce the theoretical tools for the quantum treatment of the hybrid model. I will then devote some time to present the numerical results obtained by investigating the phonon population characteristics by applying a quench to the atom-cavity subsystem. Finally, I will propose to the attentive audience a discussion of our results and present a suitable platform in view of an experimental realization of our proposal.

II. THE MODEL

In the investigated system, a two-level system, interacts with a single mode of the electromagnetic field of an optical cavity. On the other hand, the mechanical resonator is coupled to the cavity light mode via the standard optomechanical coupling. The total Hamiltonian describing our tripartite system is given by combining the Rabi Hamiltonian describing the standard dipolar coupling between the qubit and the cavity mode with the standard optomechanical Hamiltonian and reads

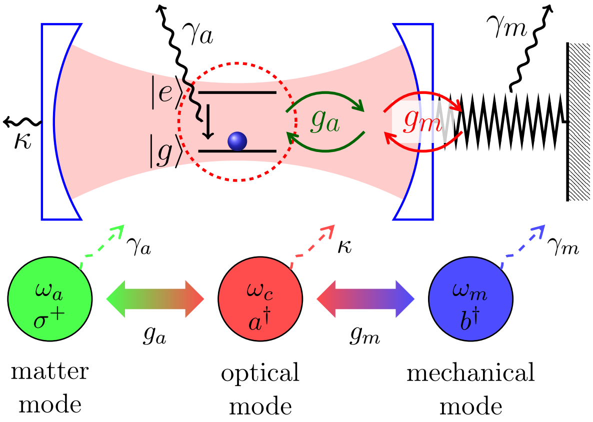

FIG. 1: Scheme and notations for the studied tripartite atom-cavity-mechanical oscillator: the mechanical mode couples via radiation pressure to a cavity-QED system.

$$\hat{\mathcal{H}} = \frac{1}{2}\hbar\omega_a\hat{\sigma}^z + \hbar\omega_c\left(\hat{a}^\dagger\hat{a} + \frac{1}{2}\right)$$
$$+\hbar g_a\left(\hat{a}+\hat{a}^\dagger\right)\left(\hat{\sigma}^- + \hat{\sigma}^+\right) + \hbar\lambda\frac{g_a^2}{\omega_a}\left(\hat{a}+\hat{a}^\dagger\right)^2 \quad (1)$$
$$+\hbar\omega_m\left(\hat{b}^\dagger\hat{b} + \frac{1}{2}\right) + \hbar g_m\hat{a}^\dagger\hat{a}\left(\hat{b}^\dagger + \hat{b}\right) .$$

ω_a , ω_c and ω_m are the bare atom, cavity photons and mechanical frequencies respectively. The atom-cavity coupling strength is written g_a and g_m is the optomechanical coupling strength. λ is a real positive scaling parameter of the A^2 term contribution. The operators $\hat{a}$, $(\hat{a}^\dagger)$ denotes the annihilation (creation) operator for the cavity light mode, σ^- (σ^+) is the lowering (raising) operator for the TLS and σ^z is the third Pauli operator and $\hat{b}$ $(\hat{b}^\dagger)$ denotes the annihilation (creation) operator for the mechanical mode.

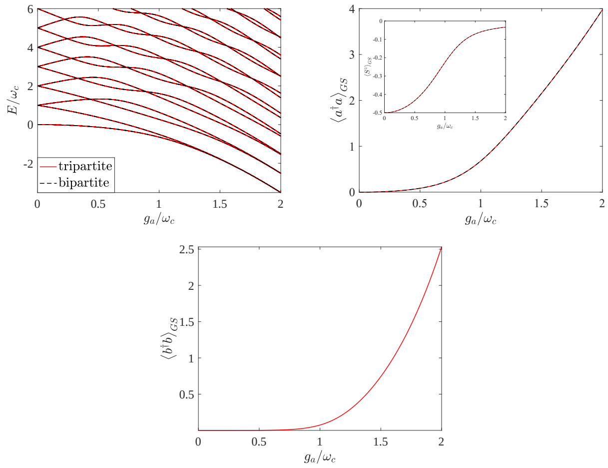

FIG. 2: Energy spectrum, mean ground-state populations of the optical field and phonon population. The inset shows the polarization of the two level system i.e. $S^z = \sigma^+\sigma^- - 1/2$.

III. REAL, VIRTUAL PARTICLES AND DISSIPATIONS

I will introduce a suitable formalism to enable the distinction between real and virtual particles and also the dressed master equation.

IV. RESULTS

The time dependent perturbation we apply to the system in order to produce real excitations in the mechanical mode consists in a continuous switch of the atom-cavity coupling strength over a finite time interval. I will show and analyze the dynamics of the hybrid system under the application of this perturbation.

V. EXPERIMENTAL FEASIBILITY AND OUTLOOKS

A suitable platform in view of an experimental realization of our proposal can be obtained in a hybrid microwave-optomechanical system[3] where a superconducting flux qubit couples to a microwave transmission line resonator. The advantage of using circuit-QED architectures and microwave cavity optomechanical structures lies in the possibility to achieve more easily ultrastrong light-matter interaction and stronger electromechanical coupling strength g_m respectively. Moreover, using superconducting flux qubit fulfills the double role of allowing switchable qubit resonator coupling in the USC regime while also allow fast enough switching of the qubit resonator coupling strength[4]. Finally, it should be noted that the magnitude of the different system parameters corresponds to state of the art values. An interesting extension of this work would be to consider a hybrid Dicke-optomechanical system, where a large ensemble of two level systems are placed into the cavity. The superradiant phase transition occurring in this new setup would give an enhancement of the different mode populations.

Acknowledgments

We thanks S. Savasta, E. Mascarenhas and P. Nataf for fruitful discussions.

This work was supported by the Swiss National Science Foundation through Project No. 200021_162357.

---

[1] A. Ridolfo, S. Savasta, and M. J. Hartmann, *Nonclassical radiation from thermal cavities in the ultrastrong coupling regime*, Phys. Rev. Lett. **110**, 163601 (2013), URL `http://link.aps.org/doi/10.1103/PhysRevLett.110.163601`.

[2] G. Scalari, C. Maissen, D. Turčinková, D. Hagenmüller, S. De Liberato, C. Ciuti, C. Reichl, D. Schuh, W. Wegscheider, M. Beck, et al., *Ultrastrong coupling of the cyclotron transition of a 2d electron gas to a thz metamaterial*, Science **335**, 1323 (2012), ISSN 0036-8075, URL `http://science.sciencemag.org/content/335/6074/1323`.

[3] J. Bochmann, A. Vainsencher, D. D. Awschalom, and A. N. Cleland, *Nanomechanical coupling between microwave and optical photons*, Nat Phys **9**, 712 (2013), ISSN 1745-2473, letter, URL `http://dx.doi.org/10.1038/nphys2748`.

[4] B. Peropadre, P. Forn-Díaz, E. Solano, and J. J. García-Ripoll, *Switchable ultrastrong coupling in circuit qed*, Phys. Rev. Lett. **105**, 023601 (2010), URL `https://link.aps.org/doi/10.1103/PhysRevLett.105.023601`.

Electrostatically Defined Quantum Dots in Bilayer Graphene

Alessia Pally,[1] Marius Eich,[1] Thomas Ihn,[1] and Klaus Ensslin[1]
[1]*Institute of Solid State Physics, ETH-Hönggerberg, CH-8093, Zürich, Switzerland*

Electronically defined quantum dots in bilayer graphene are a promising platform for spin-qubits. Using the band gap induced by applying a strong displacement field with a graphite back gate and split gates on top, charge carriers can be confined into a narrow channel. Several finger gates allow to tune the charge carrier density below them to create a versatile and highly tunable multi-dot system, where quantum dots can be formed below gates through p-n junctions or with gate-tunable tunnel barriers. We show the formation of single-, double-, and triple-dots. This system opens new possibilities for the study of spin-physics in graphene-based multi-dot systems.

I. INTRODUCTION

Graphene is a promising candidate for spin qubits, due to the low spin-orbit coupling (because of carbons low atomic mass) and low hyperfine interaction (because natural carbon is mainly composed of ^{12}C atoms)[1]. However, monolayer graphene does not exhibit a band gap, making electrostatical confinement of charge carriers difficult. In bilayer graphene a band gap can be opened by applying a perpendicular electric field[2]. By using a combination of a graphite back gate and patterned metal top gates, electrons can be electrostatically confined[3]. Quantum dots (QDs) can be formed by using additional gates. Our device allows us to control the occupation number of the QDs on the single particle level[4]. Here we will show the formation of various multi-dot systems and fully tunable single-dots.

II. SETUP

All measurement were performed in a dilution refrigerator with a base temperature of 10 mK, in a two-terminal configuration with a symmetrically applied bias voltage. Our sample consists of a bilayer graphene flake encapsulated between two boron nitride flakes with a graphite back gate and two layers of metallic top gates separated by a layer of aluminum oxide. The van der Waals heterostructure was stacked and contacted as explained in Refs. 3 and 4. A false color scanning force micrograph of the sample is shown in Fig. 1. For the measurements discussed here, only the bottom right split gates and the labelled finger gates on the right were used. By applying a positive voltage to the graphite back gate and a negative voltage to the split gates a strong displacement field is created, which induces a band gap in the bilayer graphene below the split gates[2]. If the Fermi energy is tuned into the gap, charge carriers are forced to flow through the narrow channel inbetween the split gates. By applying a voltage to the three finger gates L, R, and M, shown on the right of Fig. 1, the charge carrier density below them can be controlled.

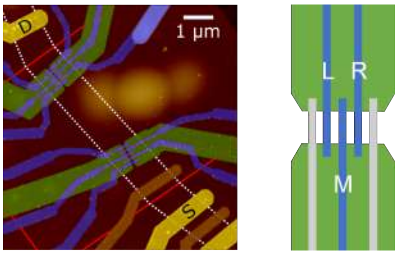

FIG. 1: Left: False color scanning force micrograph of the device. The red and white dashed lines depict the graphene flake and graphite back gate, respectively. The green gates are the split gates and the blue gates on top are the finger gates. The yellow gates are the source-drain contacts.[4] Right: Schematic of the used split gate and finger gate combination. The gray finger gates are unused. The used ones are labelled with L, R, and M.

III. MEASUREMENTS

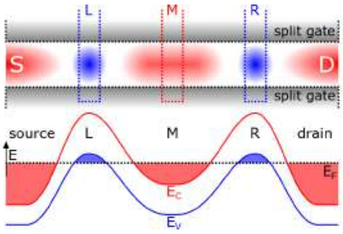

FIG. 2: Top: A schematic of the charge carrier distribution along the channel in a possible triple-dot regime. Red areas describe an electron density, while blue areas describe a hole density. Bottom: A schematic of the bandstructure of the configuration above. E_C and E_V denote the energy of the conduction and valence band, respectively. E_F denotes the Fermi energy.

Applying a large negative voltage to a finger gate tunes the band structure below the finger gate into the hole regime. Since source and drain are in the electron regime, p-n junctions will be formed between the finger gates and the leads. These p-n junctions act as natural tunnel barriers leading to the formation of a hole dot beneath the finger gate. Since each finger gate can be tuned separately with little crosstalk between them, several hole dots can be formed in series. Figure 2 shows a schematic of the band structure of a triple-dot formed by tuning the regions below gates L and R into the hole regime while

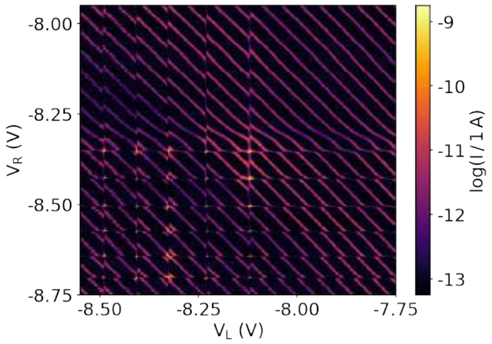

FIG. 3: Overview of the QDs with $V_M = -4.5$ V measured at 200 μV source-drain bias. The current is plotted logarithmically. The upper right quadrant corresponds to the single-dot regime. The upper left and lower right quadrants correspond to the double-dot regime. The lower left quadrant corresponds to the triple-dot regime.

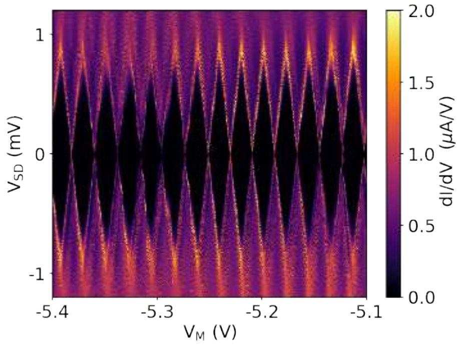

FIG. 4: Coulomb diamonds for the gate-defined QD with $V_L = -7.55$ V and $V_R = -7.5$ V and gate M acting as the plunger gate.

leaving the region below gate M in the electron regime. With three finger gates the formation of up to a quintuple dot is possible. As we see the system is highly tunable. It allows us to form up to a (2N-1)-tuple dot for N finger gates or to use several gates to obtain a fully tunable dot.

To get an overview of our system, we measure the current as a function of V_R and V_L for $V_M = -4.5$ V at 200 μV source-drain bias. The result is shown in Fig. 3, where we see three different regimes. In the upper right quadrant, a single QD is formed between gates L and R. In the upper left (lower right) quadrant, a hole-electron (electron-hole) double-dot is formed with a hole dot beneath gate L (gate R) and an electron dot between gates L and R. In the lower left quadrant, a triple-dot is formed as shown schematically in Fig. 2 with gates L and R tuned into the hole regime and an electron dot inbetween them.

Instead of forming hole dots, the finger gates can also create tunnel barriers by tuning the area underneath them close to charge neutrality. Therefore, dots with tunable tunnel barriers can be formed between two finger gates. By tuning gate L and R into the tunnel regime a big QD can be formed between them while gate M acts as a plunger gate and tunes the occupation number of the dot.

To study the gate-defined QD in more detail, we measure the Coulomb diamonds shown in Fig. 4. We set $V_L = -7.55$ V and $V_R = -7.5$ V while using gate M as plunger gate to change the occupation number of the QD. This allows us to keep the tunnel coupling constant while changing the occupation of the dot. From this measurement we extract the lever arm $\alpha = 0.041$ and the charging energy $E_{ch} = 900$ μV.

IV. CONCLUSION

The presented device offers a versatile platform for defining coupled QDs in bilayer graphene. Using the combination of a graphite back gate and metal split gates, the electrons are forced to flow through a narrow channel. Underneath smaller finger gates QDs can be defined. QDs can be defined both by p-n junctions and tunable gate-defined barriers allowing for highly tunable QDs. With several of these finger gates different multi-dot systems can be realized, which opens up new possibilities to study quantum effects such as the Kondo-effect or spin-blockade.

Acknowledgments

We thank Peter Märki, Erwin Studer, as well as the FIRST staff for their technical support. We also acknowledge financial support from the European Graphene Flagship, the Swiss National Science Foundation via NCCR Quantum Science and Technology, the EU Spin-Nano RTN network and ETH Zürich via the ETH fellowship program. Growth of hexagonal boron nitride crystals was supported by the Elemental Strategy Initiative conducted by the MEXT, Japan and JSPS KAKENHI Grant Number JP15K21722.

---

[1] B. Trauzettel, D. V. Bulaev, D. Lossi, and G. Burkard, *Spin qubits in graphene quantum dots*, Nature Physics **3**, 192 (2007).

[2] J. B. Oostinga, H. B. Heersche, X. Liu, A. F. Morpurgo, and L. M. K. Vandersypen, *Gate-induced insulating state in bilayer graphene devices*, Nano Materials **7**, 151 (2007).

[3] H. Overweg, H. Eggimann, X. Chen, S. Slizovskiy, M. Eich, R. Pisoni, Y. Lee, P. Rickhaus, K. Watanabe, T. Taniguchi, et al., *Electrostatically induced quantum point contact in bilayer graphene*, Nano Letters **18**, 553 (2018).

[4] M. Eich, F. Herman, R. Pisoni, H. Overweg, Y. Lee, P. Rickhaus, K. Watanabe, T. Taniguchi, M. Sigrist, T. Ihn, et al. (2018), (arXiv:1803.02923).

Fermi Level Pinning in GaAsSb Schottky Barriers

Ronja Khelifa,[1] Wei Quan,[2] Akshay Mahadev Arabhavi,[2] Olivier Ostinelli,[2] and Colombo Bolognesi[2]
[1]*Photonics Laboratory, ETH Zürich, CH-8093 Zürich, Switzerland*
[2]*Millimeter-Wave Electronics Laboratory, ETH Zürich, CH-8092 Zürich, Switzerland*

This work presents electrical measurements of the Schottky barrier height in n-type Gallium Arsenide Antimonide (GaAsSb) diodes. Fermi level pinning in processed Schottky barrier diodes with a nickel contact was observed. N-doped $GaAs_{0.5}Sb_{0.5}$ was grown with metalorganic chemical vapour deposition (MOCVD) on an InP substrate. A clean room process for diodes with diameters between 8 and 100 μm was developed and optimized. Current voltage (IV) characteristics for temperatures between 265 to 300 K were measured. The activation energy method was used to determine the barrier height.

I. INTRODUCTION

GaAsSb is a ternary III-V semiconductor. It is used as base material in high speed InP based double heterostructure bipolar transistors (DHBT)[1]. The characterization of the metal-semiconductor contact plays an important role in device optimization.

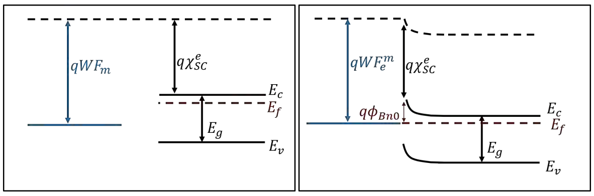

FIG. 1: Band structure of a metal and a n-doped semiconductor. left: separate, right: in contact in thermal equilibrium.

To analyse only the contact, a device with a rectifying metal-semiconductor interface, called Schottky barrier diode (SBD), is commonly fabricated. Ideally, the behavior of this diode is defined by material properties of the metal and the semiconductor (see figure 1). When brought in contact, electrons from the semiconductor diffuse into the metal, leaving behind fixed positive charges, acting as an electron barrier. The height of the so-called Schottky barrier ϕ_{Bn0} is given by the difference between the metal work function and the semiconductor electron affinity (1.13 eV for nickel on GaAsSb). In fabricated SBDs, the surface might be contaminated by other atoms or might be high in number of surface defects. This can introduce interface states within the band gap. These interface states lead to a pinning of the Fermi level at the surface of the semiconductor that is different than in bulk material. This influences the Schottky barrier height between metal and semiconductor.

II. FERMI LEVEL PINNING

Different theories for the pinning of the Fermi level in GaAs and GaSb exist. In the following, two rules are presented and adjusted to $GaAs_{0.5}Sb_{0.5}$ with an approximated band gap of $E_{\mathrm{g}} = 0.76\,\mathrm{eV}$[2].

"Two-Thirds Rule": This theory claims that for most covalent semiconductors a high peak density of surface states and defects are located about one-third above the energy level of the valence band maximum. This leads to Fermi level pinning at this point and to a barrier height of 2/3 of the band gap (~ 500 meV). This rule is found to be approximately correct for GaAs, but for GaSb not[3–5].

Acceptor States, "Anion Rule": Other measurements demonstrate that the Fermi level for a metal-SC interface, pins for GaAs near midgap and for GaSb near the valence band. The reason for the Fermi level pinning has been linked to the acceptor-like states of anion vacancies ("anion rule")[4,6,7]. Assuming for GaAsSb a linear interpolation between the relative location of acceptor states for GaAs and for GaSb, leads to an assumed barrier height of ~ 500 meV.

III. PROCESSING

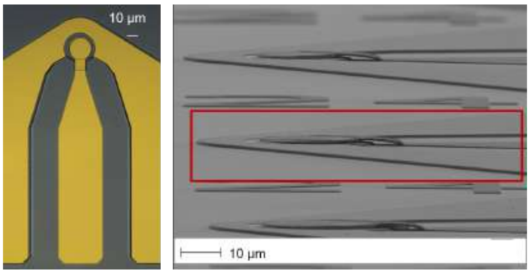

FIG. 2: Processed diodes. Left: Top view with a light Microscope. Right: Side view with a Scanning Electron Microscope (SEM). The red square marks one diode.

To measure the barrier height and analyse if Fermi level pinning can also be observed on MOCVD grown GaAsSb, Schottky barrier diodes with diameters between 8 and 100 μm were processed. Because the influence of Fermi level pinning due to impurities should be minimized, process optimization was one of the key factors. The process includes 3 etching, 6 photolithography and 3 metal evaporation steps, all performed in a clean room. To enable Ground-Signal-Ground Probing, an air bridge step had to be developed (see figure 2).

IV. MEASUREMENT RESULTS

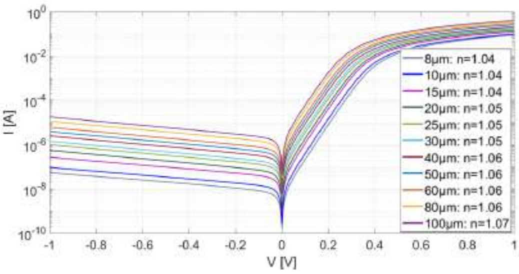

FIG. 3: Measured IV characteristics for different diode sizes at room temperature.

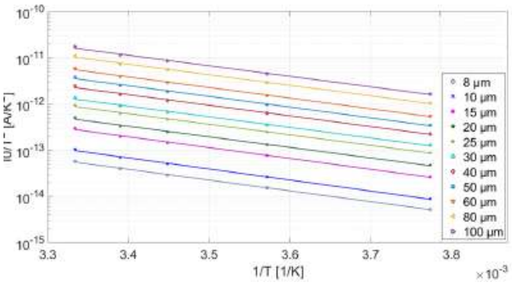

FIG. 4: Arrhenius plot for measurement results for different diode sizes. I_0 is determined by a linear fit in the logarithmic plot of the forward IV characteristic. The measurement results are at temperatures from 265 to 300 K.

For characterization, IV measurements in a cryogenic probing station were performed. All diodes showed the same behavior, independent of the location on the sample. In figure 3 representative IV measurements for different diode sizes at 300 K are shown. The ideality factor was determined by a linear fit of the forward bias and is shown in the legend. For all diode sizes it is close to unity. Thus the current is mainly determined by thermionic emission, with

$$I = I_0 \exp\left(\frac{qV}{kT}\right), \tag{1}$$

where

$$I_0 = A^{**}AT^2 \exp\left(-\frac{q\phi_{\mathrm{Bn}}}{kT}\right). \tag{2}$$

This allowed the determination of the Schottky barrier height with the so-called activation energy method. Equation 2 can be written as

$$\ln\left(\frac{I_0}{T^2}\right) = \ln\left(A^{**}A\right) - \frac{q(\phi_{\mathrm{Bn}})}{kT}. \tag{3}$$

A^{**} is the reduced effective Richardson constant, A the diode area, ϕ_{Bn} the effective barrier height, T the temperature, q the elementary charge and k the Boltzman constant. From the IV measurements, I_0 can be determined by extrapolating the linear fit in forward direction. For a temperature range between 265 and 300 K, I_0/T^2 is plotted for different diode sizes over $1/T$. From the slope of the linear fit the barrier height can be determined (see equation 3). No size dependency was observed and a mean barrier height was determined. The value is much lower than the ideal calculated barrier height of 1.13 eV. This clearly shows that Fermi level pinning can be observed.

V. CONCLUSION AND OUTLOOK

A process chain for GaAsSb Schottky barrier diodes was developed to determine electrically the Schottky barrier height with the activation energy method. Fermi level pinning was clearly observed. To determine if the Fermi level pinning follows the "two-thirds rule" or the "anion rule", more diodes with different As/Sb ratios or different metals, should be processed.

Acknowledgments

I would like to thank Prof. Dr. Oliver Ambacher, University of Freiburg, Germany, for the opportunity to supervise me during my master thesis externally in Zürich.

---

[1] C. R. Bolognesi et al., *The InP / GaAsSb Type-II Heterostructure System and its Application to High-Speed DHBTs and Photodetectors : Physics , Surprises , and Opportunities*, IEEE Electron Devices Meeting pp. 8–11 (2005).

[2] S. Adachi, *Properties of Semiconductor Alloys* (John Wiley&Sons Ltd, 2009).

[3] S. M. Sze and K. K. Ng, *Physics of Semiconductor Devices* (Willey Interscience, 2006), 3rd ed., pg. 134–179.

[4] P. W. Chye et al., *Photoemission study of Au Schottky-barrier formation on GaSb, GaAs, and InP using synchrotron radiation*, Physical Review B **18**, 5545 (1978).

[5] G. Y. Robinson, *Schottky Diodes and Ohmic Contacts for the III-V Semiconductors*, in *Physics and Chemistry of III-V Compound Semiconductor Interfaces*, edited by C. W. Wilmsen (1985), pp. 73–154.

[6] W. E. Spicer et al., *Unified defect model and beyond*, Journal of Vacuum Science and Technology **17**, 1019 (1980).

[7] J. S. Hwang et al., *GaAsSb bandgap, surface fermi level, and surface state density studied by photoreflectance modulation spectroscopy*, Applied Physics Letters **100**, 1 (2012).

Growth of in-plane InAs branched nanowires and standing <111>A GaAs nanowires by MBE

Corentin Pignot,[1] Martin Friedl,[1] Gözde Tütüncüoğlut,[1] Wonjong Kim,[1] Lucas Güniat,[1] Jordi Arbiol,[2] and Anna Fontcuberta i Morral[1]

[1]Laboratory of Semiconductor Materials, Institute of Materials, EPFL, Station 12,1015 Lausanne, Switzerland
[2]Catalan Institute of Nanoscience and Nanotechnology (ICN2),
CSIC and BIST, Campus UAB, Bellaterra, 08193 Barcelona, Catalonia Spain

We report the growth process of in-plane InAs nanowires (NWs) on top of defect-free GaAs nanomembranes (NMs) and the growth of standing <111>A GaAs NWs by molecular beam epitaxy (MBE) and selective area epitaxy (SAE). We show the low defect density of such NWs which is an important condition for electronics and optoelctronics applications. The perfect growth controllability allows us to achieve micrometer length NWs in the hope of integrating them into nanoscale devices.

I. INTRODUCTION

III-V semiconductors like GaAs and InAs are widely studied due to their very interesting electronic and optoelectronic properties arising from their unique characteristics. They present a direct band gap as well as a good band gap tunability, a high spin orbit coupling and a high g-factor to cite a few. Nanowires formed with this kind of semiconductors can be used in a very broad range of applications such as transistors, solar cells, sensors, light emitting diodes and so on. It is then understandable that a perfect growth controllability is necessary to achieve perfect optoelectronic devices.

GaAs NWs preferentially grow along the <111>B direction[1] but defects such as twins form due to similar energies of formation between twinned and untwinned monolayers. However, GaAs NWs have also been observed to grow in the <111>A direction where the energies of formation of twinned and untwinned monolayers are likely different. Thus, such NWs are good candidates for optoelectronic devices as no defect interfere with the carrier movement or the emission of light.

In-plane NWs are also interesting for the creation of nanowire networks as they have the possibility to be patterned at the large-scale over a whole wafer and to be used directly after the growth when standing NWs have to be laid down. An example where this could be useful is in experiments with Majorana Fermions (MFs) which have been experimentally observed in horizontal semiconductor nanowires in close proximity to an s-wave superconductor.[2] A big step would be to perform MFs manipulation in branched structures. We propose here to grow branched InAs NWs on top of defect-free NMs. The growth approach relies on the 7% lattice mismatch between the GaAs NMs and the InAs NWs allowing the InAs to deposit only on the top of the NMs because of surface and strain energy minimization.

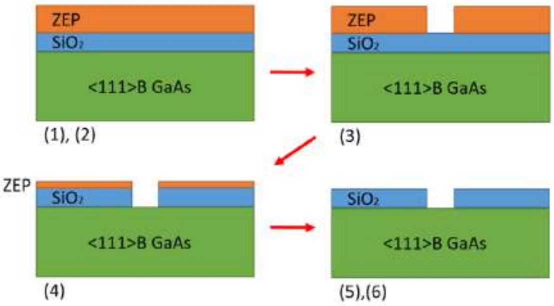

FIG. 1: Patterning of the sample

II. SUBSTRATE PREPARATION

Both InAs NWs and GaAs NWs are grown on <111>B GaAs wafers by selective area epitaxy (SAE). This method consists of creating a pattern by lithography in a mask layer allowing the GaAs to grow only in the wanted areas. The process flow is given in figure 1 and the steps are explained here. (1): Coating by PECVD of a 25 nm layer of SiO_2 on top of the GaAs wafer which will be the mask for the pattern. (2): Deposition of 60 nm of ZEP resist by spin coating (3): E-beam lithography + development of resist at -15°C (4): Etching of the SiO_2 by Reactive Ion Etching to create the pattern. (5): Resist stripping by O_2 plasma. (6): Last 10 seconds wet etch step with Hydrogen Fluoride to smoothen the pattern before the MBE growth.

In the case of in-plane InAs nanowires, the pattern created is arrays of slits and branched structures while for the standing GaAs nanowires, the pattern is arrays of ”dots” with different shapes such as circle [◦], triangle left [◁] and triangle right [▷].

III. GROWTH

The growth of the structures are performed in a DCA D600 Gen II solid-source MBE. The NWs grow by the self assembling method. As mentioned above, the InAs NWs are grown on GaAs defect-free nanomembranes.[3]

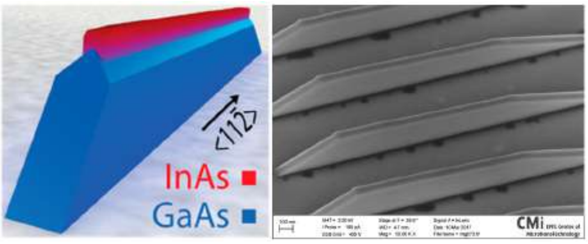

FIG. 2: **Left:** Schematic of the formation of the NMs and NWs **Right:** SEM image of NMs and NWs

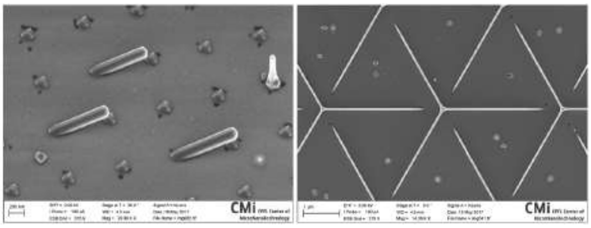

FIG. 3: **Left:** <111>A GaAs NWs **Right:** Top view of branched InAs NWs on top of defect-free GaAs NMs

By doing so we hope to reduce to the minimum the defects in the InAs NWs. The growth therefore include two parts, the growth of the NMs followed by the growth of the NWs.

For the NMs and for the standing NWs, the same growth recipe has been used. It has been found so far that the best growing parameters are a pyrometer temperature of 630°C, a Ga pressure of $2.4 \cdot 10^{-7}$ Torr and an As pressure of $2.8 \cdot 10^{-6}$ Torr. Those NWs and NMs have been grown for 30 minutes. The InAs NWs are then grown for 200s with an As pressure of $8 \cdot 10^{-6}$ Torr and an indium rate of 0.2 Å/s.

IV. RESULTS

Morphology: By these two methods, we have achieved micrometer length NWs. The results can be seen in figure 4. The InAs NWs can be scaled to below 50 nm in diameter and the GaAs NWs diameter can be reduced to 100 nm. The defect-free membranes only grow in the $<11\bar{2}>$ direction. The <111>A NWs grow in three different directions corresponding to the three <111> axis and it has been found that the best shape for the growth is the triangle left [◁].

Crystal structure: Analysis of the crystal structure of the NWs was done by HR-TEM. As expected, the <111>A NWs present a twin-free structure and it appears that the in-plane NWs have a low defect density with a misfit density of approximatively $100/\mu m$ and a twin density of $15/\mu m$. As a comparison, <111>B InAs NWs have a defect density of $400/\mu m$.[4]

Elemental mapping: We performed EELS on a cross section showing a high concentration of In at the top of the membranes as well as a small concentration of Ga at the junction between the nanowire and the nanomembrane due to diffusion during the growth.

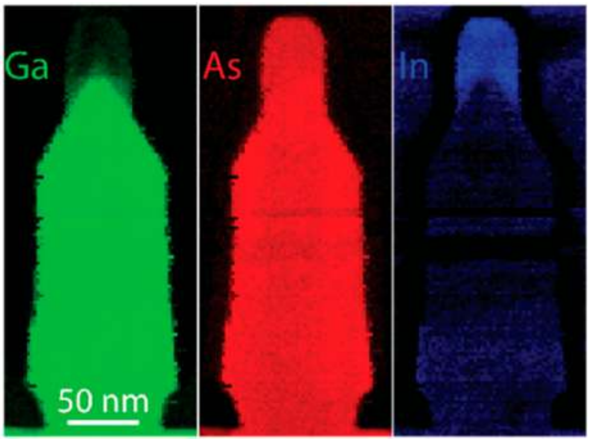

FIG. 4: EELS maps with elemental contrast of a NM/NW cross section.

Acknowledgments

This work is founded through the NCCR QSIT. We would also like to thank the CMi staff at EPFL for their support.

[1] X. Yuan, P. Caroff, J. Wong-Leung, L. Fu, H. H. Tan, and C. Jagadish, *Tunable Polarity in a III-V Nanowire by Droplet Wetting and Surface Energy Engineering*, Advanced Materials **27**, 6096 (2015), ISSN 15214095.

[2] V. Mourik, K. Zuo, S. M. Frolov, S. R. Plissard, E. P. a. M. Bakkers, and L. P. Kouwenhoven, *Signatures of Majorana Fermions in*, Science **336**, 1003 (2012), ISSN 0036-8075, 1204.2792.

[3] G. Tutuncuoglu, M. de la Mata, D. Deiana, H. Potts, F. Matteini, J. Arbiol, and A. Fontcuberta i Morral, *Towards defect-free 1-D GaAs/AlGaAs heterostructures based on GaAs nanomembranes*, Nanoscale **7**, 19453 (2015), ISSN 2040-3364, URL `http://xlink.rsc.org/?DOI=C5NR04821D`.

[4] H. Potts, M. Friedl, F. Amaduzzi, K. Tang, G. Tütüncüoglu, F. Matteini, E. Alarcon Lladó, P. C. McIntyre, and A. Fontcuberta I Morral, *From Twinning to Pure Zincblende Catalyst-Free InAs(Sb) Nanowires*, Nano Letters **16**, 637 (2016), ISSN 15306992.

[5] M. Friedl, K. Cerveny, P. Weigele, G. Tütüncüoglu, S. Martí-Sánchez, C. Huang, T. Patlatiuk, H. Potts, Z. Sun, M. O. Hill, et al., *Template-Assisted Scalable Nanowire Networks*, Nano Letters **18**, 2666 (2018), ISSN 15306992.

Influencing a Tunnel Junction with a Silver Nanocube

Anna Kuzmina,[1] Markus Parzefall,[1] Eric Bonvin,[1] and Lukas Novotny[1]
[1] *Photonics Laboratory, ETH Zürich, CH-8093, Zürich, Switzerland*

We discuss the development of an experiment to demonstrate the possibility of changing the electrical properties of gold - h-BN - graphene tunnel junctions due to the modification of the local density of optical states (LDOS) in the junction area. The modification of the LDOS will be carried out by positioning of a silver nanocube near the top surface of the junction. We will first present the main physical bases of the considered effect, then give a short description of the experimental setup and briefly discuss fabrication methods.

I. INTRODUCTION

Let us consider a tunnel junction which by definition consist of two layers of conducting materials with a potential barrier between them. An electron can pass (tunnel) through the barrier with conservation of the energy or with losing part of its energy. The two scenarios are refered to as elastic and inelastic electron tunneling, respectively. The inelastic tunneling process can be accompanied by light emission. Thus tunnel junctions could be used for transducing energy from an electronic source to optical radiation. These nanoscale emitters are of great interest not only because of their sub-wavelength size but also due to their high operation speed enabled by the femtosecond timescale of the tunneling process. However, the efficiency of energy conversion highly depends on the geometry of the junction[1], surrounding structures[2] and the choice of materials.

A significant number of recent studies was focused on metal-insulator-metal (MIM) tunneling junctions. The geometry of a representative MIM device with schematical step-by-step illustrations of the inelastic tunnelling process[3] is shown in Fig. 1. The inelastic tunneling event is accompanied by the excitation of a surface plasmon polariton (SPP) which radiatively decays with rate Γ_{rad}. Also, the rate of inelastic tunneling events Γ_{inel} is proportional to the local density of states (LDOS) and generally lower than the elastic one. Thus, in order to maximize the radiative efficiency of the device, we need to maximize both Γ_{inel} and Γ_{rad}.

In MIM junctions the Γ_{inel} rate could reach 10% of elastic tunneling rate[4] because of the strongly confined field inside the gap, but significant non-radiative SPP decay due to metal absorption make it difficult to realize efficient light emitter. Also the tunneling and plasmonic part are inseparable from each other in traditional MIM junctions. Both of these issues can be overcome by using a system which consists of a Van der Waals (VdW) tunneling device as a driving source and a separate plasmonic nanoparticle to define the optical properties of the system and improve photon conversion rates. In this type of structures, the top metal electrode is replaced by a graphene sheet which has negligible absorption in the optical range. A plasmonic nanoparticle is used to confine the electromagnetic fields in the junction area and to transduce the energy to the far-field[2,5].

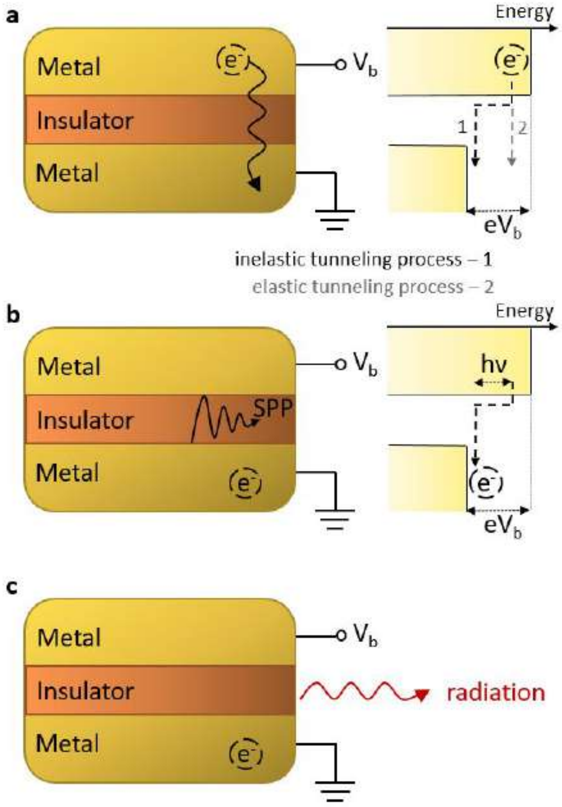

FIG. 1: Step-by-step illustration of the tunneling process in the MIM device. (a) Applying the positive voltage V_b and considering the same material of metal electrodes, the difference between Fermi levels of two metal parts become eV_b. The electron can tunnel from the upper electrode either elastically, i.e. with energy conservation, or inelastically, i.e. losing a part of an additional energy. (b) In case of inelastic tunneling an electron firstly excites surface plasmon polariton (SPP) mode and then (c) it partially decays to the radiation channel.

In our previous works the plasmonic nanoparticle had the stationary position on top of VdW junctions[2]. Our present goal is to experimentally study the dynamic IV characteristics during modulation of the vertical position of the nanoparticle. The sketch of the considered structure is shown in Fig. 2. The distance between the nanoparticle and the tunnel junction defines the LDOS in the junction area which should lead to a variation of the number of inelastic tunneling events. Thus the current through the junction should also be modulated.

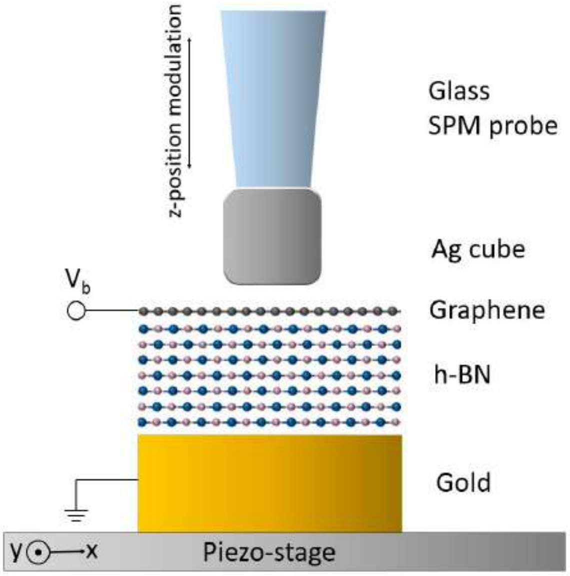

FIG. 2: VdW tunneling device consists of a bottom gold electrode (50 nm thickness), few layers of hexagonal boron nitride (h-BN) and a single layer of graphene. The plasmonic nanoparticle has a cubic shape (75 nm on edge) and it is attached to the glass SPM probe. The tunneling device can be moved in the horizontal (XY) plane via a piezo-electric stage, the vertical (Z) position of the nanocube is controlled by the SPM feedback system.

II. EXPERIMENTAL SETUP

The experimental setup allows for the variation of the distance between a device surface and a nanoparticle with nanometer precision. The glass probe with a nanocube is attached to the quartz tuning fork which acts as an electromechanical resonator. The feedback system tracks small changes in the resonance frequency of the tuning fork and keeps it constant by varying the distance (z-position). This design gives the opportunity to set the maximum interaction force between a probe and a surface and thus set the minimum distance between them. Also, the sample stage can be software-controlled which is very convenient for relative positioning of a probe and a device with tens of nanometer precision.

The electrical current change after a nanocube approach is expected to be lower than 1% of the absolute current magnitude. To conduct the experiment with high accuracy we will use a lock-in amplification scheme which will be locked to the vertical position modulation frequency. This approach will decrease the error of measurements as it allows for the rejection of electrical noise of the system at any other frequency.

III. FABRICATION METHODS

Chips with gold electrodes on a glass substrate are created by photolithography and thin film evaporation. They are used as a base for tunneling devices. These electrodes can act either as bottom electrodes of the VdW tunnel junction or as the contact for the graphene top layer. The graphene and h-BN flakes are firstly exfoliated from the bulk crystals and then characterized by optical and atomic-force microscopes to determine their thickness. Finally, suitable flakes are picked up, stacked on top of each other and transferred to the chip following the procedure which was developed by Zomer et al.[6]

The probe fabrication is carried out following the procedure developed by P. Bharadwaj[7]. Pulled glass fibers with 70 nm apex diameter are treated with APTES molecules and then immediately attached to the tuning fork. Then nanocubes are spin-coated on a clean coverslip. In order to attach a nanocube to the probe the nanocube firstly needs to be localized by topography measurements and then carefully picked up by changing or switching off the feedback loop. We are currently working on the development of a reproducible recipe for probe fabrication.

Acknowledgments

We would like to thank NCCR QSIT and ETHZ for financial support of this project

---

[1] J. Kern, R. Kullock, J. Prangsma, M. Emmerling, M. Kamp, and B. Hecht, *Electrically driven optical antennas*, Nature Photonics **9**, 582 (2015).

[2] M. Parzefall, A. Szabo, T. Taniguchi, K. Watanabe, M. Luisier, and L. Novotny, *Light from van der waals quantum tunneling devices* (2018), arXiv:1804.06163v1.

[3] M. Parzefall, Ph.D. thesis, ETH Zurich (2017).

[4] L. C. Davis, *Theory of surface-plasmon excitation in metal-insulator-metal tunnel junctions*, Physical Review B **16**, 2482 (1977).

[5] S. Namgung, D. A. Mohr, D. Yoo, P. Bharadwaj, S. J. Koester, and S.-H. Oh, *Ultrasmall plasmonic single nanoparticle light source driven by a graphene tunnel junction*, ACS Nano **12**, 2780 (2018).

[6] P. J. Zomer, M. H. D. Guimaraes, J. C. Brant, N. Tonbros, and B. J. van Wees, *Fast pick up technique for high quality heterostructures of bilayer graphene and hexagonal boron nitride*, Applied Physics Letter **105**, 013101 (2014).

[7] P. Bharadwaj, Ph.D. thesis, ETH Zurich (2012).

Interference Effects in InAs/GaSb Core-Shell Nanowires

Zijin Lei,[1] Christopher Mittag,[1] Heidi Potts,[2] Simon Robert Escobar Steinvall,[2] Matija Karalic,[1]
Martin George Friedl,[2] Anna Fontcuberta i Morral,[2] Thomas Ihn,[1] and Klaus Ensslin[1]

[1]Laboratory for Solid State Physics, ETH Zürich, CH-8093, Zürich, Switzerland
[2]Laboratory of Semiconductor Materials, EPFL, CH-1015 Lausanne, Switzerland

We report on a low-temperature magnetoconductance study to characterize the electrical and spin transport properties of InAs/GaSb core-shell nanowires grown by a gold free molecular beam epitaxy (MBE) method. The preliminary results show the universal conductance fluctuations and a density controlled crossover from weak localization to weak antilocalization. With one dimensional theory, the spin-orbit length and the phase coherence length have been extracted.

I. INTRODUCTION

Due to the band lineup, InAs-GaSb heterostructures can lead to the coexistence of particles and holes at the charge neutrality point. As predicted by Liu *et al.*[1], with strong spin-orbital interactions (SOIs), two-dimensional InAs-GaSb heterostructures, i.e. double quantum wells (DQWs), can exhibit a topological phase. Compared with the theoretical[2] and experimental[3] research on DQW systems, studies on one-dimensional heterostructure, i.e., InAs/GaSb core-shell nanowires (CSNWs) are still lacking. Based on the publications, with a certain ratio of the thickness of InAs and GaSb, the nanowire can also have an inverted band structure. Similar to DQWs, with the coexistence of particles and holes and strong SOIs in both regimes, InAs/GaSb CSNWs will have peculiar transport features[4,5].

In systems with strong SOIs, the spin relaxation can be probed through magnetoconductance measurements. In disordered conductors at low temperatures, constructive interference of pairs of backscattered, time-reversed paths interfere constructively in weak localization (WL). In the presence of spin relaxation, the interference can be destructive, yielding a positive conductivity correction known as weak antilocalization (WAL). These two kinds of corrections depend on the phase coherence length L_ϕ and the spin-orbital length $L_{\rm so}$, which indicate the scale on which the phase- and spin-information is preserved. These two length scales depend on the carrier density and temperature. In this presentation, we show magnetoresistance measurements on two InAs/GaAs CSNW samples: one is a single nanowire device and the other on is a parallel double wire device. In both samples, WL effect is found and in the double wire sample, the gate controlled crossover of WL and WAL is studied.

II. SAMPLE AND MEASUREMENT SET UP

The InAs/GaSb CSNWs studied here were grown in [111] direction using MBE through gold free methods. The InAs is the core, which is ~ 75 nm in diameter while the GaSb, which is ~ 25 nm thick, is wrapped as a shell. The wires are ~ 2.7 μm long and the width of the wires is $W \sim 125$ nm[6]. The insets of Fig.1 show the SEM images of the single and double wire devices. The nanowires were transferred from the growth substrate to a doped Si/SiO$_2$ wafer via the wet method[6]. The dielectric layer is 250 nm thick and the whole Si wafer works as a back gate to tune the carrier density. Four Ti/Au contacts are fabricated through standard electron beam lithography and metal sputtering. In order to reduce contact resistance, a short ion milling is done before sputtering. After fabrication, the distance between two inner contacts L is ~ 800 nm. Electronic measurements were performed in a 1.7 K ^{4}He system with a perpendicular magnetic field. The conductance of the nanowires is measured using DC four-terminal method. The conductance $G = V/I$, where V is the voltage between two inner contacts and I is the current through the outer two contacts.

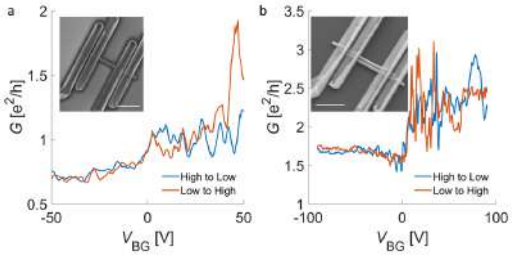

FIG. 1: The field effect measurement of single wire (a) and double wire (b) device. The insets are SEM images. The scale bar is 1 μm in both images.

III. RESULTS AND MODELING

Fig. 1 shows the field effect measurement of two samples. In both samples, the conductance of the individual wires is around e^2/h. Through the tuning of back gate voltage $V_{\rm BG}$, the conductance can be tuned. The conductance is minimal when $V_{\rm BG} = 0$ V. When $V_{\rm BG} > 0$ V, with the increase of $V_{\rm BG}$, the channel gets opened. This indicates the accumulation of electrons in InAs core. However, when $V_{\rm BG} < 0$ V the field effect is not obvious. The channels in both samples cannot be pinched off and the single wire sample has obvious hysteresis effect.

Fig. 2 presents the universal conductance fluctuations (UCF) of the single wire sample in a perpendicular magnetic field. Pronounced fluctuations of the conductance symmetric in B and a dip or peak at $B = 0$

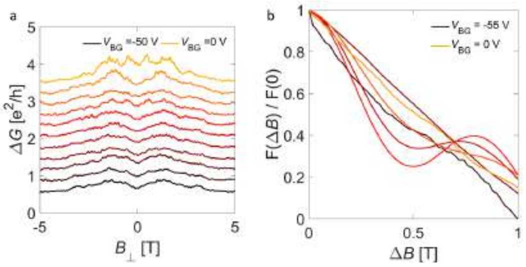

FIG. 2: (a) The magnetoresistance of single-nanowire sample. (b) Autocorrelation function of UCF in single nanowire sample.

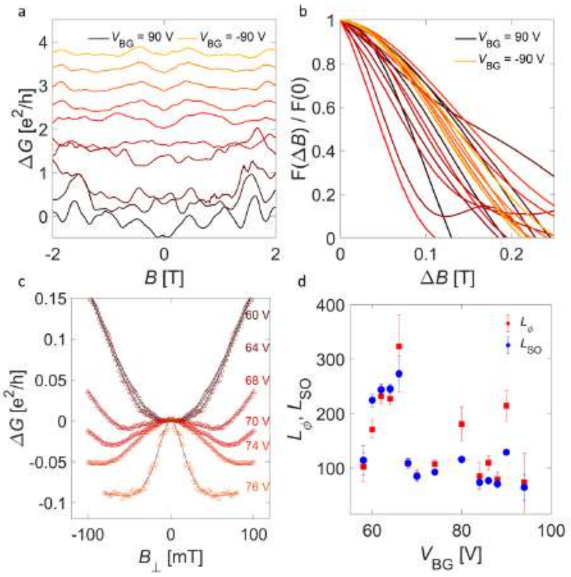

FIG. 3: (a) The magnetoresistance of double-nanowire sample. (b) Autocorrelation function of UCF in double nanowire sample. (c) Crossover of WL and WAL (d) L_ϕ and $L_{\rm SO}$ extracted from WL and WAL.

T can be clearly recognized. The amplitude of UCF rms(G) is $\sim 0.1e^2/h$.Fig.2.b shows the autocorrelation function $F(\Delta B) = \langle \delta G(B+\Delta B)\delta G(B)\rangle$ with different $V_{\rm BG}$. To get rid of the influence of WL and WAL, the magnetic field range is confined to [1, 4.5] T. From the decay of $F(\Delta B)$, we can get the correct value of ΔB_C for $F(\Delta B_C)/F(0) = 0.5$. In our measurement, $\Delta B_C \sim 500$ mT, with the formula $\Delta B_C = C\Phi_0/WL_\phi$, where C is a constant decreasing from 0.95 for $L_\phi \gg L_T$ to 0.95 for $L_\phi \ll L_T$and Φ_0 is flux quantum, we can estimate the phase coherence length $L_\phi \sim 20$ nm.

Fig. 3 shows the measurement results of double wire device. Similar to the single wire device, the UCF, WL, and WAL are observed. We use the similar method to analyze the UCFs. Here the amplitude is comparable with the single wire device, which is between $0.05 \sim 0.25e^2/h$, but ΔB_C is much smaller, which is $\sim$ 150 mT, suggesting a longer phase coherence length. For $L_\phi \gg$ W, $\Delta B_C = C\frac{h/e}{\pi W^2/4}$, which corresponds to the width of the nanowire.

Fig. 3c presents the crossover of WL and WAL when $V_{\rm BG} > 0$ V. With the increase of $V_{\rm BG}$, we can see the dip of WL change into peak of WAL. For the dirty metal regime ($L_\phi \gg L$, $\lambda \gg W$), the correction is

$$\Delta G(B) = -\frac{2}{h}\frac{e^2}{L}[\frac{3}{2}(\frac{1}{L_\phi^2} + \frac{4}{3L_{SO}^2}\frac{1}{D\tau_B})^{-1/2} - \frac{1}{2}(\frac{1}{L_\phi^2} + \frac{1}{D\tau_B})^{-1/2}],$$

where magnetic relaxation time is $\tau_B = \frac{3L_m^4}{W^2 D}$ and $D = v_{\rm F}/L_{\rm e}$ in one dimension[7]. From Fig.3 d we can see in the range of $V_{\rm BG}$ we study, $L_{\rm SO}$ and L_ϕ are always comparable.

IV. CONCLUSION AND OUTLOOK

Here we report our preliminary results of magnetoresistance of InAs/GaSb core-shell nanowires. In the future, it will be interesting to compare the magnetotransport of both particles and holes and to investigate the existence of Berry phase of this system via Aharonov-Bohm effect.

Acknowledgments

We acknowledge the support of the Swiss National Science Foundation.

---

[1] C. Liu, T. L. Hughes, X.-L. Qi, K. Wang, and S.-C. Zhang, *Quantum spin hall effect in inverted type-II semiconductors*, Phys. Rev. Lett. **100**, 236601 (2008).

[2] F. Qu, A. J. A. Beukman, S. Nadj-Perge, M. Wimmer, B.-M. Nguyen, W. Yi, J. Thorp, M. Sokolich, A. A. Kiselev, M. J. Manfra, et al., *Electric and magnetic tuning between the trivial and topological phases in InAs/GaSb double quantum wells*, Phys. Rev. Lett. **115**, 036803 (2015).

[3] M. Karalic, S. Mueller, C. Mittag, K. Pakrouski, Q. Wu, A. A. Soluyanov, M. Troyer, T. Tschirky, W. Wegscheider, K. Ensslin, et al., *Experimental signatures of the inverted phase in InAs/GaSb coupled quantum wells*, Phys. Rev. B **94**, 241402 (2016).

[4] V. V. R. Kishore, B. Partoens, and F. M. Peeters, *Electronic structure of InAs/GaSb core-shell nanowires*, Phys. Rev. B **86**, 165439 (2012).

[5] M.-E. Pistol and C. E. Pryor, *Band structure of core-shell semiconductor nanowires*, Phys. Rev. B **78**, 115319 (2008).

[6] H. Potts, *Ph.D. thesis: Gold-free growth of InAs nanowires growth, structural and electrical properties* (2017).

[7] A. E. Hansen, M. T. Björk, C. Fasth, C. Thelander, and L. Samuelson, *Spin relaxation in inas nanowires studied by tunable weak antilocalization*, Phys. Rev. B **71**, 205328 (2005).

Measuring the effect of vacuum field fluctuations on quantum Hall transport in the ultra-strong coupling regime

Johan Andberger,[1] Gian L. Paravicini-Bagliani,[1] Felice Appugliese,[1] Giacomo Scalari,[1] Mattias Beck,[1] and Jérôme Faist[1]

[1] *Institute of Quantum Electronics, ETH-Hönggerberg, CH-8093, Zürich, Switzerland*

In the regime of ultra-strong light-matter coupling a fundamental prediction is the non-zero occupation number of the ground (vacuum) state of the system.[1] We study the effect of this vacuum field on magnetotransport by coupling a 140 GHz complementary split-ring resonator cavity to a magnetotransport system and then modulating the cavity electric field using a metallic tip mounted on a set of piezoelectric slip-stick drives. By modulating the cavity electric field the strength of the light-matter coupling can be tuned and the effect of the vacuum field fluctuations on the magnetotransport system studied.

I. INTRODUCTION

Light-matter interaction is fundamental to quantum electrodynamics. Considering the interaction strength, quantified by the Rabi frequency Ω_R, between the matter and optical parts of a system different regimes can be identified. The Rabi frequency is given by

$$\hbar\Omega_\mathrm{R} = \vec{d}\cdot\vec{E}\,\sqrt{N} \tag{1}$$

with $\vec{d}$ being the dipole moment, $\vec{E}$ the (vacuum) electric field and N being the number of two-level systems the photons can couple to. When the coupling rate exceeds the different loss rates of the system, e.g. cavity loss, the strong coupling regime is reached. In this regime the matter and optical parts hybridize to form dressed states called polaritons. When the coupling becomes comparable to the unperturbed frequency of the optical or matter part the ultra-strong coupling regime is reached and in addition a squeezed vacuum ground state forms. The ultra-strong coupling regime has been demonstrated in several different systems.[2–4]

Here a high-mobility two-dimensional electron gas (2DEG) in a GaAs/AlGaAs heterostructure with Hall bar geometry is used as matter part and a 140 GHz complementary split-ring resonator as optical part. In an applied external magnetic field at cryogenic temperatures the quantization of the cyclotron orbits, called Landau levels, manifests in magnetotransport measurements in the form of the quantum Hall effect and Shubnikov-de Haas oscillations. The cavity can couple to the Landau levels by placing the 2DEG in-plane with the cavity electric field, this is illustrated in Fig. 1 (a). The gap of the split-ring resonator is 40 micrometres, indicating that the 140 GHz LC resonance is strongly sub-wavelength. This is one of the motivations for considering this system because the small mode volume produces an extremely large vacuum field, which can be estimated to be

$$E_\mathrm{vac} \sim \sqrt{\frac{\hbar\omega_\mathrm{cav}}{\varepsilon_0\varepsilon_r V_\mathrm{eff}}} \sim 1\ \mathrm{V/m}. \tag{2}$$

It has been previously shown that under illumination with a sub-terahertz light source polaritons can be observed in magnetotransport measurements.[5] To observe the effect of vacuum field fluctuations in magnetotransport the cavity is modulated electrostatically using a metallic tip that can be positioned at arbitrary positions above the resonator.

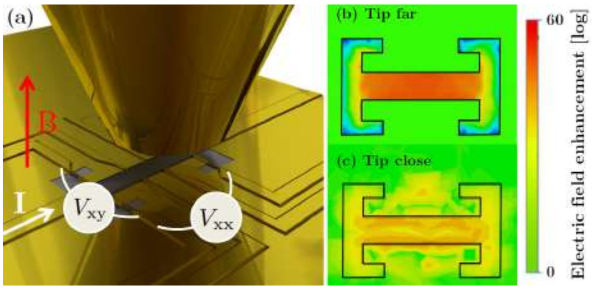

FIG. 1: (a) Hall bar geometry with complementary split-ring resonator gold metamaterial on top and tip positioned above. Shubnikov-de Haas oscillations are observed in measurements of $V_\mathrm{xx}(B)$ and the quantum Hall effect is observed in $V_\mathrm{xy}(B)$. (b) Simulation of the in-plane electric field with the tip far away, the cavity enhances the electric field by an order of magnitude. (c) When the tip is close the electric field enhancement is strongly reduced.

II. EXPERIMENT

The high-mobility 2DEG is formed in a GaAs/$\mathrm{Al_{0.3}Ga_{0.7}As}$ triangular quantum well 90 nm below the surface in a heterostructure grown by molecular beam epitaxy. A Si δ-doping layer with a density of 3.5×10^{12} cm^{-2} is located 50 nm below the surface, resulting in a 2DEG with an approximate electron density of $n_\mathrm{2D} = 2.1\times10^{11}$ cm^{-2} and electron mobility $\mu = 2\times10^6$ cm^2/Vs. The Hall bar mesa structure is defined by etching and the gold metamaterial is deposited on top to define the complementary split-ring resonator.

The magnetotransport measurements are performed in a dry dilution fridge with an electronic temperature of approx. 100 mK using a standard lock-in technique at magnetic fields up to 6T. The gold metamaterial could be

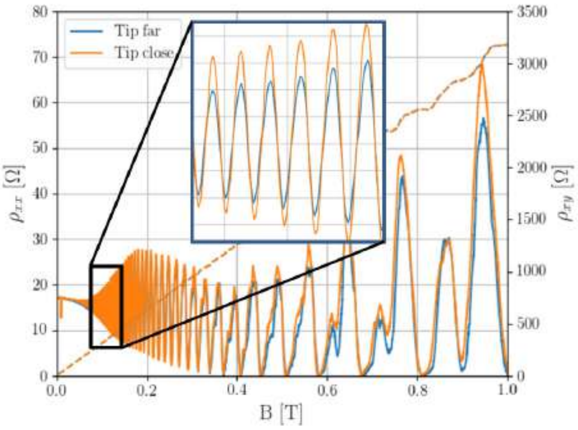

FIG. 2: The Shubnikov-de Haas oscillations from two magnetotransport measurements, one with the tip close and one with it far away from the cavity. A reduction in the amplitude is visible when the tip is close, as can be seen in the inset.

used as a top gate for limited tuning of the electron density, for the measurements the gate was biased at 200 mV.

The tip for modulating the cavity is gold-coated and can be positioned a few micrometres from the cavity using a set of three piezoelectric slip-stick drives. This tip diverts the electric field out of the cavity and alters the LC resonance frequency, reducing the electric field enhancement and therefore also the coupling strength to the 2DEG. Fig. 1 (b) and (c) show CST simulations of the tip close and far from the resonator.

III. RESULTS

The presence of the tip close to the resonator leads to a reproducible change in the amplitude of the Shubnikov-de Haas oscillations, but no change in their frequency in 1/B implying that the electron density stays constant,[6] i.e. the tip does not act on the sample in the form of a gate. The amplitude of the Shubnikov-de Haas is determined by the electron temperature and the quantum lifetime and since the temperature remains constant this implies that the vacuum field fluctuations result in a reduced quantum lifetime.[7] One explanation for this is that the polaritons provide additional loss channels, although this remains to be investigated.

IV. CONCLUSION AND OUTLOOK

The ability to investigate an ultra-strongly coupled system by measurements on both the optical and matter parts, as can be done in this system, is unusual and enables better investigation of the polariton state. In the near future higher-mobility samples will enable the study of fractional quantum Hall states and higher-density samples made of InSb opens up the investigation of higher light-matter coupling strengths. In the long term the goal would be to detect the photons in the squeezed vacuum ground state by non-adiabatic switching of the cavity.

---

[1] C. Ciuti, G. Bastard, and I. Carusotto, *Quantum vacuum properties of the intersubband cavity polariton field*, Physical Review B - Condensed Matter and Materials Physics **72**, 1 (2005), ISSN 10980121, 0504021.

[2] Y. Todorov, A. M. Andrews, R. Colombelli, S. De Liberato, C. Ciuti, P. Klang, G. Strasser, and C. Sirtori, *Ultrastrong light-matter coupling regime with polariton dots*, Physical Review Letters **105**, 1 (2010), ISSN 00319007, 1301.1297.

[3] G. Scalari, C. Maissen, D. Turcinkova, D. Hagenmuller, S. De Liberato, C. Ciuti, C. Reichl, D. Schuh, W. Wegscheider, M. Beck, et al., *Ultrastrong Coupling of the Cyclotron Transition of a 2D Electron Gas to a THz Metamaterial*, Science **335**, 1323 (2012), ISSN 0036-8075, arXiv:1111.2486v1, URL `http://www.sciencemag.org/cgi/doi/10.1126/science.1216022`.

[4] E. Orgiu, J. George, J. A. Hutchison, E. Devaux, J. F. Dayen, B. Doudin, F. Stellacci, C. Genet, J. Schachenmayer, C. Genes, et al., *Conductivity in organic semiconductors hybridized with the vacuum field*, Nature Materials **14**, 1123 (2015), ISSN 14764660, 1409.1900.

[5] G. L. Paravicini-Bagliani, F. Appugliese, E. Richter, F. Valmorra, J. Keller, M. Beck, C. Rössler, T. Ihn, K. Ensslin, G. Scalari, et al., *Tomography of an ultrastrongly coupled polariton state using magneto-transport in the quantum regime*, pp. 1–9 (2018), arXiv:1805.00846v1, URL `https://arxiv.org/pdf/1805.00846.pdf`.

[6] T. Ando, *Theory of Quantum Transport in a Two-Dimensional Electron System under Magnetic Fields. IV. Oscillatory Conductivity*, Journal of the Physical Society of Japan **37**, 1233 (1974), ISSN 13474073.

[7] N. Bartolo and C. Ciuti, *Vacuum-dressed cavity magnetotransport of a 2D electron gas*, pp. 1–5 (2018), 1805.02623, URL `http://arxiv.org/abs/1805.02623`.

Nanoscale imaging with scanning-NV magnetometry

P. Welter,[1] M. Palm,[1] M. S. Wörnle,[2,1] K. Chang,[1] Jan Rhensius,[1] C. Degen,[1] and P. Gambardella[2]
[1]*Institute of Solid State Physics, ETH- Zürich, CH-8093, Zürich, Switzerland*
[2]*Departement of Materials, ETH- Zürich, CH-8093, Zürich, Switzerland*

Nitrogen-vacancy defects in diamond are at the heart of a novel scanning probe technique for imaging magnetic fields. It combines high spatial resolution with high sensitivity. NV center magnetometry is an outstanding method for imaging electrical currents in nanostructures and mapping stray fields of magnetic thin films.

I. INTRODUCTION

Scanning magnetometry with nitrogen-vacancy (NV) centers in diamond is a novel technique to image magnetic fields at the nanoscale. The NV center, affixed to the apex of a cantilevered tip, serves as a sensor to measure local magnetic fields. Raster-scanning the tip over a sample yields two-dimensional maps of the magnetic fields at the surface.

Since its first proposal nearly two decades ago[1], the technique has sparked a considerable interest in the scientific community, seeing rapid progress and improvements to its performance continuing to this day. In recent years it has reached a level of maturity where it has become an almost routine tool when studying the rich field that is mesoscopic physics.

The technique combines high spacial resolution ($< 30\,\mathrm{nm}$) and high sensitivity ($\sim 100\,\mu\mathrm{T}/\sqrt{\mathrm{Hz}}$)[2]. It is applicable at a wide range of temperatures, including cryogenic and room temperature. It is also highly non-invasive, due to the lack of any significant magnetic back-action. Various sensing protocols exist that are sensitive to frequencies from DC up to GHz range.

The method has for instance been used to measure stray fields from magnetic structures[3–6], or the Oerstredt field of a current passing through a conductor[2]. In the latter case, reconstruction techniques allow a recovery of an image of the current density[2].

II. MAGNETIC FIELD SENSING

Our sensor is the negatively charged NV center, a color defect in diamond. It consists of a substitutional nitrogen located next to a vacant lattice point.

An energy diagram of the NV center is shown in FIG. 1c). The electronic ground and exited states $|g\rangle$ and $|e\rangle$ are located inside the diamond bandgap. Both are spin triplets, with $|m_s = 0\rangle$ separated from $|m_s = \pm 1\rangle$ by the zero field splitting D. Illumination with green laser light will populate the excited state. In addition to radiative relaxation (accompanied by the emission of a red photon), the excited state may also decay via a long-lived singlet state $|s\rangle$. The transition probability to this dark state is significant mostly for the $|m_s = \pm 1\rangle$ states. The fluorescence intensity is thus suppressed in the case of non-zero spin.

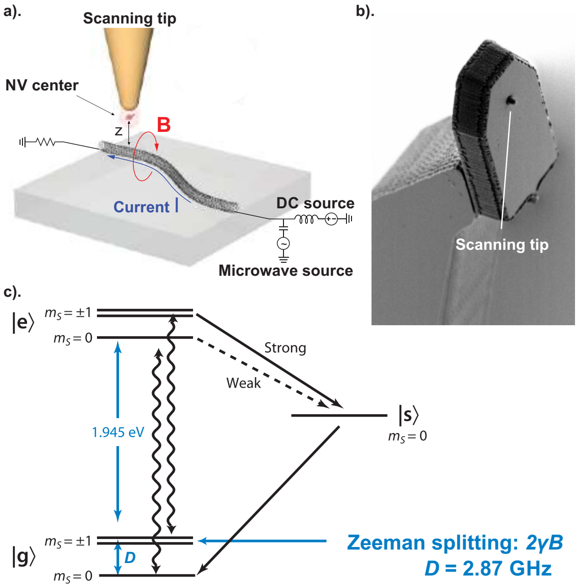

FIG. 1: a). Schematic representation of a current sensing experiment[2]. A nanodiamond containing a single NV center is attached to the apex of a commercial AFM cantilever tip. The NV center is scanned over the sample (here: a carbon nano-tube) and measures the Oerstedt field emanating from the sample. The microwave field required for ODMR is applied through the carbon nanotube itself. Optical illumination and readout occur through the transparent substrate. Adapted from reference[2]. b). An SEM picture of a monolithic diamond scanning probe with an NV center in the tip of a diamond pillar. c). Energy diagram of the NV center. The electronic ground and excited states $|e\rangle$ and $|g\rangle$ are spin triplets. Excitation can occur via illumination with green laser light. The decay back to the ground state can be radiative (wiggly lines) or non-radiative via a dark singlet state $|s\rangle$. The unequal transition rates (solid and dashed lines) result in spin-dependent fluorescence. An external magnetic splits the $|m_s = \pm 1\rangle$ degeneracy. Adapted from reference[7].

Continous illumination will eventually pump the NV into the $|m_s = 0\rangle$ state.

A. Optically detected magnetic resonance

These properties of the NV center make it suitable as a magnetic field sensor. By applying a microwave field

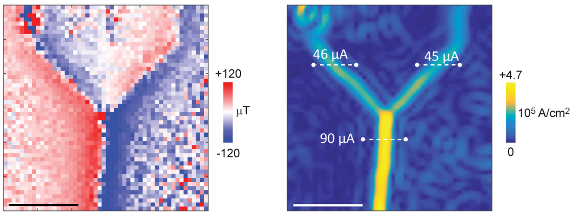

FIG. 2: a). Image of the Oersted field $B_{||}$ of a Y-shaped current-carrying Pt nanowire. b). Current density image reconstructed from the data in a). Integrating along the dashed lines shows that, qualitatively, current is conserved. All scale bars are $1\,\mu$m. Adapted from reference[2].

at the electron paramagnetic resonance (EPR) frequency (i.e. resonant with the $|m_s = 0\rangle \leftrightarrow |m_s = \pm 1\rangle$ transition), we can pump the non-zero spin states, and, in turn, see a reduced fluorescence intensity. Magnetic fields along the NV axis will lift the $|m_s = \pm 1\rangle$ degeneracy via Zeeman effect.

By sweeping the applied microwave frequency, one can determine the respective EPR resonance frequencies. The Zeeman shift $2\gamma_e B_{||}$ (where $\gamma_e = 28\,\text{GHz/T}$ is the electron gyromagnetic ratio) gives direct access to the local magnetic field[7]. For experimental purposes, a static bias field is applied, so that the two resonances are well separated and distinguishable.

B. Current imaging

A current in a conductor engenders an Oerstedt field. NV magnetometry is well suited to probe this field, see FIG. 1a. Assuming that the field was recorded at a constant height above the surface, and that the current is confined to the plane, one can invert Biot and Savart's law, and recover all three components of the current density (FIG. 2).

C. Scanning probes

While the first generation scanning probes consisted of a nanodiamond affixed to a commercial Si cantilever, we currrently use all-diamond scanning pillars. An SEM image of a diamond paddle with etched tip is shown in FIG. 1b. The pillars notably offer improved photon collection efficiency by close to an order of magnitude, as fluorescent light is wave-guided towards the detection optics. Recent advances in this area put forward a further order of magnitude enhancement, by carefully giving the pillar a parabolic taper.[8]

III. FUTURE WORK

In the future we intend to continue to improve the performance of our scanning probes, enhancing their sensitivity, reliability and overall practicality. We plan to make use of more advanced, detection schemes, which employ pulsed laser and microwave excitation.[9] These are expected to yield order of magnitude improvements in small signal detection.

Concerning samples, we are currently studying magnetic thin-films. NV magnetometry has proven to be an outstanding tool to help understanding and development of spintronic devices, for instance magnetic random access memory (MRAM).

---

[1] B. M. Chernobrod and G. P. Berman, *Spin microscope based on optically detected magnetic resonance*, Journal of Applied Physics **97**, 014903 (2005).

[2] K. Chang, A. Eichler, J. Rhensius, L. Lorenzelli, and C. L. Degen, *Nanoscale imaging of current density with a single-spin magnetometer*, Nano Letters **17**, 2367 (2017).

[3] I. Gross, W. Akhtar, V. Garcia, L. J. Martnez, S. Chouaieb, K. Garcia, C. Carrtro, A. Barthlmy, P. Appel, P. Maletinsky, et al., *Real-space imaging of non-collinear antiferromagnetic order with a single-spin magnetometer*, **549**, 252 (2017), ISSN 1476-4687.

[4] G. Balasubramanian et al., *Nanoscale imaging magnetometry with diamond spins under ambient conditions*, Nature **455**, 648 (2005).

[5] J.-P. Tetienne, T. Hingant, L. Rondin, S. Rohart, A. Thiaville, E. Ju, G. Gaudin, J.-F. Roch, and V. Jacques, *Nitrogen-vacancy-center imaging of bubble domains in a 6- film of cobalt with perpendicular magnetization*, Journal of Applied Physics **115**, 17D501 (2014).

[6] L. Rondin et al., *Stray-field imaging of magnetic vortices with a single diamond spin.*, Nat. Commun. **4**, 2279 (2013).

[7] R. Schirhagl, K. Chang, M. Loretz, and C. L. Degen, *Nitrogen-vacancy centers in diamond: Nanoscale sensors for physics and biology*, Annual Review of Physical Chemistry **65**, 83 (2014).

[8] N. H. Wan, B. J. Shields, D. Kim, S. Mouradian, B. Lienhard, M. Walsh, H. Bakhru, T. Schröder, and D. Englund, *Efficient extraction of light from a nitrogen-vacancy center in a diamond parabolic reflector*, **18**, 2787 (2018), ISSN 1530-6984, URL `https://doi.org/10.1021/acs.nanolett.7b04684`.

[9] C. L. Degen, *Scanning magnetic field microscope with a diamond single-spin sensor*, Applied Physics Letters **92**, 243111 (2008).

Near-field Raman Spectroscopy of Long Linear Carbon Chains encapsulated in Double Walled Carbon Nanotubes

Mikołaj Roguski,[1,2] Sebastian Heeg,[1] Lei Shi,[3] Thomas Pichler,[3] and Lukas Novotny[1]
[1]Photonics Laboratory, ETH-Hönggerberg, CH-8093, Zürich, Switzerland
[2]School of Chemistry, University of Edinburgh, EH9 3JJ Edinburgh, UK
[3]University of Vienna, Faculty of Physics, 1090 Wien, Austria

We investigate electronic and optical properties of long linear carbon chains encapsulated in double walled carbon nanotubes. By using tip-enhanced Raman scattering we are able to achieve spatial resolution of $\sim$ 25 nm, suitable for studying single carbon nanotube-chain pairs. Our aim is to describe the effects of the local environment of an inner nanotube on the optical band gap as well as vibrational properties of the encapsulated chain.

I. INTRODUCTION

Finite long linear carbon chains (LLCC) consisting of more than 100 atoms are considered to be a good approximation of the sp^1 hybridized linear carbon allotrope named carbyne.[1] Their predicted mechanical properties such as strength and young modulus surpass those of any other known material.[2] Despite many efforts, the longest lone-standing chains synthesised so far consisted of only 44 neighbouring carbon atoms due to their high reactivity under ambient conditions.[3] Additionally, short carbon chains are stabilized by end-capping groups affecting the inherent electronic properties of the chains. Recently, it was demonstrated that an interior of a multiwalled carbon nanotube can serve as a nanoreactor for formation of LLCC consisting of thousands of carbon atoms.[4,5] The confined space inside carbon nanotubes facilitates the carbon chain formation and protects them from the interactions with the outer environment. High stability and no recorded aging effect enable us to investigate their properties.[4] The structure of a LLCC in a double walled carbon nanotube (DWCNT) is presented in Fig. 1(a).

The form of LLCC with alternating single and triple bonds is energetically favoured due to a Peierl's distortion. This bond length alternation results in the opening of an electronic band gap and makes the chains suitable for optical spectroscopy measurements. An in-phase vibration of triple bonds between carbon atoms, referred to as the C-mode, is the only Raman-active mode of the chains and is shown in Fig. 1(b).[1] The local environment of an inner nanotube interacts with the encapsulated chains via van der Waals interactions, charge transfer and dielectric screening effect.[6] Last year, van der Waals interactions were described to be a dominating effect affecting the chains C-mode frequencies.[7] It was reported that different chiralities of the nanotubes are correlated with different Raman responses from the chains.

Our current goal is to study the charge transfer from the nanotube onto the encapsulated chains. To achieve this, we localize and characterize the DWCNTs which are only partially filled with chains by Raman spectroscopy. The comparison of the nanotube's Raman signal from the filled and empty parts, reports the presence of charge transfer effects. In general, the spatial resolution of a confocal microscope is diffraction limited to roughly a half of a wavelength of the incident light, which is insufficient to distinguish filled and empty DWCNTs. However, by using a laser-irradiated tip acting as an optical antenna, we are able to reach spatial resolution of down to 25 nm.[8] Such a high resolution enable us to probe the Raman signal from the filled and empty parts of the same DWCNT.

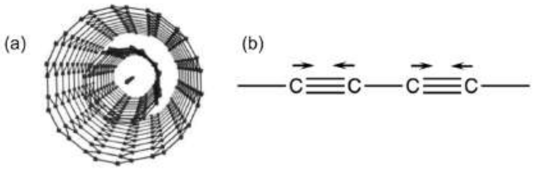

FIG. 1: (a) Model of long linear carbon chain encapsulated in double walled carbon nanotube. (b) Sketch of linear carbon chains with alternating double and triple bonds. The only Raman-active vibration of LLCC, C-mode, is described with the arrows above the carbon atoms.

II. EXPERIMENTAL

In our home-build experimental setup an inverted confocal microscope is combined with an atomic force microscope. A golden pyramid serves as a highly localized light source for Raman scattering. It is placed in the focus of the oil-immersion objective and is irradiated by a radially-polarized laser beam (633 nm). The optical signal from the sample is collected with the same objective and either is detected with an avalanche photo diode combined with a series of filters (used for imaging) or analyzed by a spectrograph with a CCD camera attached.

III. TERS IMAGING OF SINGLE CHAINS

In our experiment, first we map the area of the sample with the confocal Raman Spectroscopy in order to localize the LLCC. We also take Raman spectra to verify the presence of a single chain and its Raman frequency. A typical Raman spectrum is presented in Fig. 2. Usually we observe the chain's C-mode and the three modes cor-

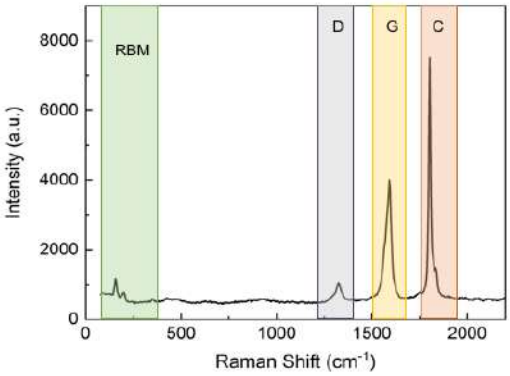

FIG. 2: Raman spectrum of long linear chains in double walled carbon nanotubes. The visible peaks are assigned to the bands corresponding to the vibrations of the nanotubes (RBM, D, G) and of the chains (C).

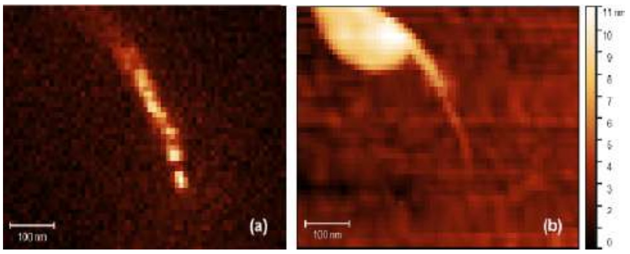

FIG. 3: Near-field Raman (a) and topographic (b) images of long linear chain in double walled carbon nanotube. The area of high topography just above the single tube is most likely an agglomeration of carbon nanotubes.

responding to the vibrations of the nanotubes. In particular, we are interested in the radial breathing mode (RBM) which provides us with the information on the diameter and chirality of nanotubes and the G-mode corresponding to the in-plane vibrations along the nanotube's hybrdized sp^2 bonds. The RBM as well as the G-mode describe the local environment for the confined chains.

Next, we approach the chains with the tip to map the intensity of the C-mode peak and topography of the sample. The correponding images are shown in Fig. 3(a) and (b). We are able to precisely localize the chains and the host nanotube. Additionally, topographic measurements reveal if there are any empty nanotubes around.

IV. OUTLOOK

The next step is to aquire tip-enhanced Raman spectra of the already identified partially-filled carbon nanotubes. Charge transfer between the inner carbon nanotube and the chain will result in a shift of the G-mode frequency, which is very sensitive to doping.[9] By comparing the Raman shift of the nanotube's G-peak for the regions with and without a chain inside, we will verify the charge transfer effects. Our experiments will bring further insight into the complex interaction between the host nanotube and the confined long liner carbon chains.

Acknowledgments

We acknowledge support from NCCR QSIT (GrantNo. 51NF40-160591) and from the Swiss National Science Foundation (grant no. 200021 165841). S.H. acknowledges financial support by ETH Zürich Career Seed Grant SEED-16 17-1.

---

[1] R. B. Heimann, S. E. Evsyukov, and L. Kavan, *Carbyne and carbynoid structures*, vol. 21 (Springer Science & Business Media, 1999).

[2] M. Liu, V. I. Artyukhov, H. Lee, F. Xu, and B. I. Yakobson, *Carbyne from first principles: chain of c atoms, a nanorod or a nanorope*, ACS nano **7**, 10075 (2013).

[3] W. A. Chalifoux and R. R. Tykwinski, *Synthesis of polyynes to model the sp-carbon allotrope carbyne*, Nature chemistry **2**, 967 (2010).

[4] X. Zhao, Y. Ando, Y. Liu, M. Jinno, and T. Suzuki, *Carbon Nanowire Made of a Long Linear Carbon Chain Inserted Inside a Multiwalled Carbon Nanotube*, Physical Review Letters **90**, 4 (2003).

[5] L. Shi, P. Rohringer, K. Suenaga, Y. Niimi, J. Kotakoski, J. C. Meyer, H. Peterlik, M. Wanko, S. Cahangirov, A. Rubio, et al., *Confined linear carbon chains as a route to bulk carbyne*, Nature Materials **15**, 634 (2016).

[6] M. Wanko, S. Cahangirov, L. Shi, P. Rohringer, Z. J. Lapin, L. Novotny, P. Ayala, T. Pichler, and A. Rubio, *Polyyne electronic and vibrational properties under environmental interactions*, Physical Review B **94**, 6 (2016).

[7] S. Heeg, L. Shi, L. V. Poulikakos, T. Pichler, and L. Novotny, *Carbon nanotube chirality determines properties of encapsulated linear carbon chain*, arXiv preprint arXiv:1711.04753 (2017).

[8] Z. J. Lapin, R. Beams, L. G. Cançado, and L. Novotny, *Near-field raman spectroscopy of nanocarbon materials*, Faraday discussions **184**, 193 (2015).

[9] S. Reich, C. Thomsen, and J. Maultzsch, *Carbon Nanotubes: Basic Concepts and Physical Properties* (Wiley, 2008).

Parametric symmetry breaking in a nonlinear resonator

Anina Leuch,[1,2] L. Papariello,[2] T. L. Heugel,[2] C. L. Degen,[1] O. Zilberberg,[2] R. Chitra,[2] and A. Eichler[1]
[1]*Institute for Solid State Physics, ETH Zurich, 8093 Zurich, Switzerland*
[2]*Institute for Theoretical Physics, ETH Zurich, 8093 Zurich, Switzerland*

We investigate a resonating system subject to a fundamental interplay between intrinsic nonlinearities and a combination of several driving forces. We have constructed a controllable and robust realization of such a system using a macroscopic doubly clamped string. We experimentally observe a hitherto unseen double hysteresis in both the amplitude and the phase of the resonators response function[1] which are in excellent agreement with the theoretical model. The double-hysteretic response can be understood through a symmetry breaking of parametric phase states that elucidates the selection criteria governing transitions between stable solutions. We further investigated that a parametrically driven resonator can sense external forces with an improved signal-to-noise performance when operated in the nonlinear regime[2].

I. INTRODUCTION

Parametric excitation of resonators plays an important role in many areas of science and technology. In its best known form, parametric excitation describes the modulation of a resonator's natural frequency at twice the natural frequency itself. In this case, energy is pumped into or out of the resonator depending on the phase of the modulation relative to the oscillation. For sufficiently strong parametric driving, the effective damping of the linear resonator becomes negative and the oscillation amplitude is stabilized by nonlinearities. The negative effective damping regime of the parametric resonator is particularly interesting because it features two stable oscillation solutions. These solutions, which we term 'parametric phase states', are a result of the double periodicity of the parametric excitation. They are degenerate in amplitude, but phase shifted by π, and they are fascinating because they allow for the study of broken time-translation symmetry and activated interstate switching in both classical and quantum systems. Recently, it was shown that an external force field can lift the amplitude degeneracy between the parametric phase states[3]. This degeneracy lifting becomes pronounced in the presence of nonlinear damping and leads to a robust double hysteresis in the frequency-swept response of the resonator, which can be used to measure small near-resonant forces.

II. EXPERIMENT

Our experimental setup consists of a doubly clamped steel string, see Fig. 1. Parametric excitation is realized by modulation of the position of one clamping point to change the tension inside the string. The motion of the string at ω is transduced into a voltage and read out via a lock-in amplifier. The lowest energy mode of the device satisfies the well-known equation of motion for a nonlinear, parametrically excited resonator:

$$\ddot{x}+\omega_0^2\left[1-\lambda\cos\left(2\omega t\right)\right]x+\Gamma\dot{x}+\alpha x^3+\eta x^2\dot{x}=\frac{F_0}{M}\cos\left(\omega t+\phi\right)\ , \tag{1}$$

where x is the displacement of the resonator and dots mark differentiations with respect to time t. The modulation amplitude λ controls the parametric excitation and $\Gamma=\omega_0/Q$ is the linear damping coefficient with Q the mechanical quality factor. The nonlinearities α and η denote the conservative (Duffing-type) and dissipative nonlinearities, respectively. F_0 is the amplitude of an applied external force, M is the effective mass of the resonator, and ϕ is a phase difference between applied force and parametric excitation.

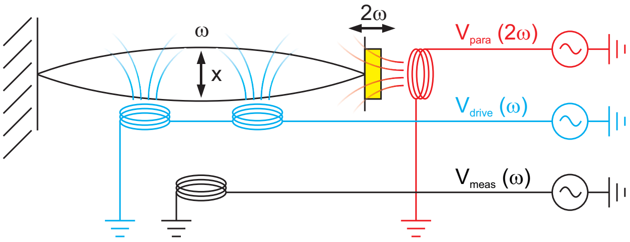

FIG. 1: Experimental realization of a parametric resonator based on a doubly clamped steel string (0.23 mm × 0.23 mm × 0.36 m). Direct driving at frequency ω and parametric excitation at frequency 2ω rely on AC currents through coils induced by voltages V_{drive} and V_{para}, respectively. The string position is read out from the voltage V_{sens} induced in a pickup coil.

We use relatively weak external driving to characterize the linear behavior of the device. Figure 2(a) shows the response of the lowest mechanical mode to driving voltages V_{drive} from 3.5 to 215 mV. To access the nonlinear regime of large displacement amplitudes ($r > d$), we parametrically excite the device. In the absence of an external driving force, we measure large and stable vibrations for values of the parametric excitation voltage V_{para} beyond a threshold of 0.6 V, see Fig. 2(b).

A striking interplay unfolds when parametric excitation and external driving act simultaneously. In Fig. 2(c), the measured displacement amplitude for an upward frequency sweep exhibits a single jump (at the boundary between domains III and IV), akin to the jump expected in standard externally driven Duffing resonators in the absence of parametric excitation. However, for downward frequency sweeps, a double hysteresis appears and the response displays two consecutive jumps (at the III-II and II-I boundaries, respectively). While the jumps (III-IV) and (III-II) describe the typical hysteresis for externally driven Duffing resonators, the second jump (II-

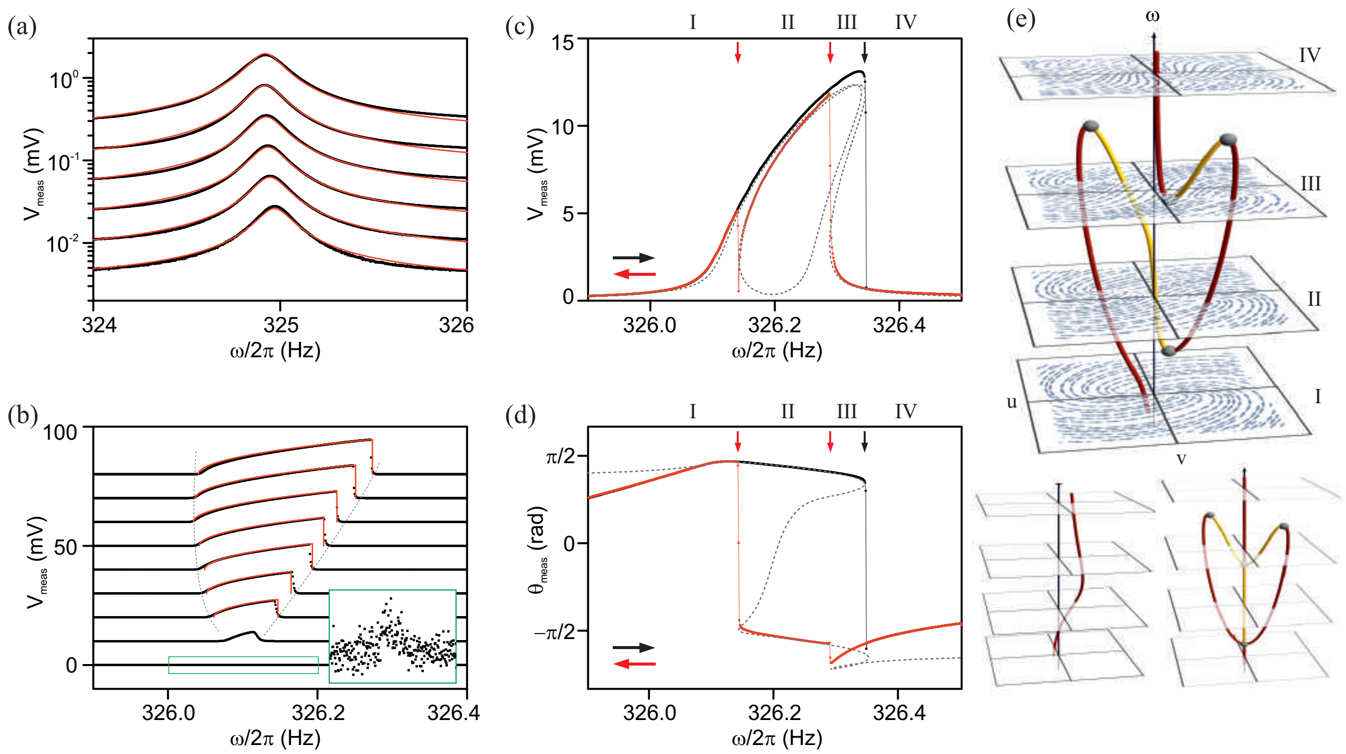

FIG. 2: Device response to the various drives: measured mean displacement as a function of drive frequency (dots). (a) Linear response with weak external drive amplitudes $V_{\rm drive} = 3.15 - 215\,{\rm mV}$ and with $V_{\rm para} = 0$. The background increase is due to direct electrical coupling between the drive and detection coils. All theoretical fits (red dashed lines) use $Q = 1800$. (b) Response to parametric excitation with $V_{\rm drive} = 0$ and $V_{\rm para} = 0.6\,{\rm V} - 215\,{\rm mV}$. All theoretical fits (red dashed lines) use a common model with $Q = 1800$, $\alpha = 2.45\times10^{10}\,{\rm m^{-2}s^{-2}}$ and $\eta = 6.8\times10^{6}\,{\rm m^{-2}s^{-1}}$. Curves are vertically offset by 10mV for better visibility and instability boundaries are traced by (gray) dashed lines. Inset shows onset of instability for $V_{\rm para} = 0.6\,{\rm V}$. (c)-(d) Main results: first experimental demonstration of double-hysteretic response when both external and parametric drives are activated. Plotted are the measured (c) mean displacement and (d) oscillation phase as a function of the drives' frequency for both upward sweep (black dots) and downward sweep (red dots). The response can be split into four domains (I-IV) by the appearance of three jumps, one at the upward sweep and two on the downwards sweep. Here, $V_{\rm drive} = 0.1\,{\rm mV}$, $V_{\rm para} = 0.8$ and $\phi = -45^\circ$. Theory curves are gray dashed lines. (e) For the fitted parameters, representative calculated stability maps of the system in the four domains at $\omega = 0.9997\omega_0$ in I, $\omega = 1.0\omega_0$ in II, $\omega = 1.0003\omega_0$ in III and $\omega = 1.0006\omega_0$ in IV. The evolution of the stable solutions (dark red lines) and unstable solutions (bright yellow lines), as well as the bifurcations (grey spheres) as a function of the driving frequency are also shown. In (f) and (g), the corresponding stationary solution evolution for an external drive ($\lambda = 0, F \neq 0$) and a parametric drive ($\lambda \neq 0, F = 0$) are shown. The range of $u = r\cos(\theta)$ and $v = r\sin(\theta)$ axes corresponds to $\pm 0.65\,{\rm mm}$ for (e) and (g), and for (f) it is $\pm 0.065\,{\rm mm}$.

I) is a novel feature that stems from an interplay with parametric excitation and has not been seen before in an experiment. The same hysteretic responses are more prominent in the measured oscillation phase $\theta_{\rm meas}$, see Fig. 2(d).

We could further experimentally confirm the predicted relationship between the applied near-resonant force and the position of the second jump (II-I)[2,3]. By investigating its the sensitivity to noise, we discovered that this method is highly insensitive to readout noise, which makes it, for example, promising for applications with nanomechanical force sensors.

Acknowledgments

We acknowledge technical support and know-how from P. Märki, C. Keck, U. Grob and T. Ihn. The construction of the setup was done in collaboration with the engineering office (M. Baer) and the mechanical workshop at the Department of Physics at ETH Zurich. This work has been supported by the ERC through Starting Grant 309301, and by the Swiss National Science Foundation.

---

[1] A. Leuch, L. Papariello, O. Zilberberg, C. L. Degen, R. Chitra, and A. Eichler, *Parametric symmetry breaking in a nonlinear resonator*, Phys. Rev. Lett. **117**, 214101 (2016).

[2] A. Eichler, A. Leuch, C. Degen, R. Chitra, and O. Zilberberg, *A parametric symmetry breaking transducer* (2017), arXiv:1803.10467.

[3] L. Papariello, O. Zilberberg, A. Eichler, and R. Chitra, *Ultrasensitive hysteretic force sensing with parametric nonlinear oscillators*, Physical Review E **94**, 022201 (2016).

Photon-mediated interactions between semiconductor qubits

Jann H. Ungerer,[1] David J. van Woerkom,[1] Pasquale Scarlino,[1] Clemens Müller,[2] Jonne V. Koski,[1] Andreas Landig,[1] Christian Reichel,[1] Werner Wegscheider,[1] Thomas Ihn,[1] Klaus Ensslin,[1] and Andreas Wallraff[1]

[1] *Laboratory for Solid State Physics, Department of Physics, ETH Zürich, CH-8093 Zürich, Switzerland*
[2] *Institute for Theoretical Physics, Department of Physics, ETH Zürich, CH-8093 Zürich, Switzerland*

Here we report an experiment consisting of two double-quantum dot (DQD) qubits, both strongly coupled to the same high-impedance SQUID-array resonator. We have realized coherent second-order interactions between the two qubits which are probed by performing microwave spectroscopy on the resonator. These coherent interactions resulted in avoided-crossings up to $2J = 27\,\mathrm{MHz}$ in the dispersive regime. This approach of using superconducting resonators as quantum-buses for coupling semiconductor qubits is expected to contribute to scaling up semiconductor devices for quantum information applications.

I. INTRODUCTION

Semiconductor qubits have been intensively investigated for quantum information applications[1]. The advantages of this platform are the flexibility in tuning, long coherences and well-known fabrication techniques[2,3]. The demonstration of spin coherence times exceeding seconds in purified silicon[4] boosted the research in this direction. So far, multi-qubit coupling was realized between very close ($\sim 100\,\mathrm{nm}$) double quantum dot (DQD) qubits via exchange interaction or capacitive coupling between charge qubits[5–7] and spin qubits[8–10]. One approach for extending the coupling range to 200-500 nm uses an additional quantum dot mediating the interaction[11–13]. Recently, a different approach that was inspired by the superconducting qubit community yielded strong coupling between a single microwave photon in a superconducting resonator and charge qubits [14–16], quickly followed by strong coupling to spin[17,18] qubits.

The present work is inspired by the superconducting qubit community where spatially separated superconducting qubits are routinely coupled[19,20]. In this talk, I will present our approach of coupling two DQD charge qubits to the same high-impedance superconducting resonator. We thereby realize coherent second-order interactions between the two qubits[21]. For more details, consider reading the corresponding publication[22].

II. SAMPLE DESCRIPTION

The sample consists of two DQD charge qubits, both strongly coupled to a single high-impedance $\lambda/4$ resonator (Fig. 1). The resonator is composed of 35 SQUIDS. Therefore, its resonance frequency is flux-tunable and it has an estimated impedance of $\sim 1\,\mathrm{k}\Omega$. At its open end, the DQDs are defined by using depletion gate technology on a mesa of a GaAs/AlGaAs heterostructure. They are separated by a distance of $42\,\mu\mathrm{m}$. The DQDs lie in the antinode of the electrical field of the resonator. The design and fabrication is similar to the one described elsewhere[15,23]. For performing reflection spectroscopy, we apply a microwave tone to a drive line, capacitively coupled to the resonator and measure the reflected amplitude and phase.

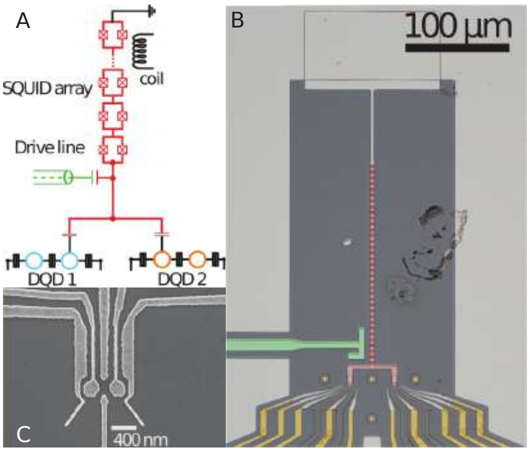

FIG. 1: (A) Circuit schematic with $\lambda/4$-SQUID array resonator (red), drive line (green), both DQDs (cyan and orange) and an external coil (black). (B) False colored optical micrograph, showing the measured device. The colors correspond to (A). The GaAs/AlGaAs mesa is colored dark-gray and the metallic gates defining the DQDs are colored gold-gray. (C) SEM micrograph of gate structure used for defining the DQDs in the GaAs/AlGaAs heterostructures.

Using the reflected amplitude, we determine the resonator frequency ν_r as a function of flux. We then configure the 2 DQDs ($k = 1, 2$) as two-level systems. The transition frequencies of the bare two-level systems are $\omega_k = \sqrt{4t_k^2 + \delta_k^2}$. Here, δ_k is the detuning and t_k is the tunnel coupling between the quantum dots. Both, δ_k and t_k can be tuned by changing the voltages on the gate electrodes shown in the SEM micrograph in Fig. 1C.

III. MEASUREMENT RESULTS

Making use of the tunable resonator, we tune successively $\nu_\mathrm{r} \approx 2t_k$ and measure the reflected phase at the resonator while varying the detuning δ_k of both DQDs individually (see Fig. 2A for DDQ2). We observe

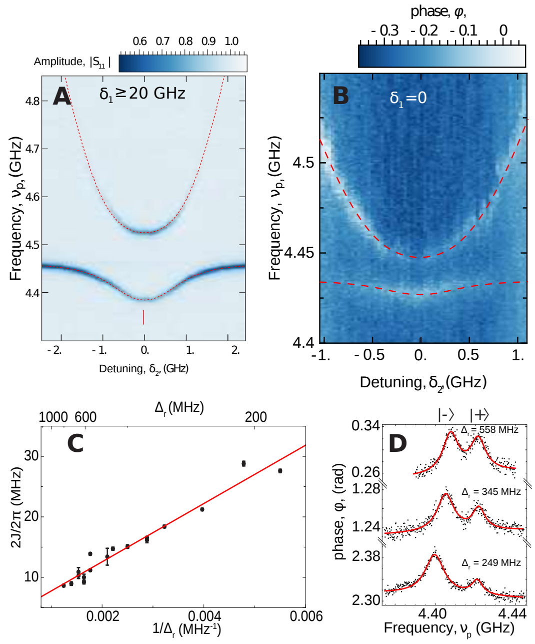

FIG. 2: (A) Vacuum Rabi splitting in the reflection spectrum $|S_{11}|$ changing δ_2 of DQD2 ($2t_2 = 4.448\,\mathrm{GHz}$) to bring DQD2 in resonance with the resonator state at $\nu_\mathrm{r} = 4.462\,\mathrm{GHz}$. (B) Dispersive Readout of resonator at $\nu_\mathrm{r} = 4.717\,\mathrm{GHz}$. DQD2 is brought in resonance with DQD1 at $\nu_1 = 4.436\,\mathrm{GHz}$. (C) Avoided level splitting $2J$ between qubit states extracted from fits to two Lorentzian lines in the resonator phase shift as shown in (D) for different resonator detunings Δ_r. The dashed red lines are fits to a master equation simulation.

avoided level-crossings between the photon state and the qubit-state from which we extract the coupling strengths $g_1/2\pi = 34\,\mathrm{MHz}$ and $g_2/2\pi = 69\,\mathrm{MHz}$ between each individual DQD qubit and the resonator. This avoided level-crossing can be well-resolved because $g_k/2\pi > \kappa/2 + \Gamma_{2,k}$, where κ is the photon loss rate from the resonator and $\Gamma_{2,k}$ denotes the linewidth of the qubits. This means that we are in the strong-coupling regime.

By varying the flux through the SQUIDs, we then change the resonator frequency to $\nu_\mathrm{r} = 4.717\,\mathrm{GHz}$, $\nu_\mathrm{r} - \nu_k \approx 8g_1 \approx 4g_2$. In this part of the experiment, we use the coupling between the resonator and the qubits for dispersive readout of the qubit states[15,24,25]. By varying both δ_k, we bring the qubit frequencies into resonance (Fig. 2B). When the individual qubit states are degenerated, they interact with each other mediated by virtual photons in the resonator. Therefore, the qubit states hybridize. As a consequence, in spectroscopy one can observe an avoided level-splitting of $2J = 2g_1 g_2/\Delta_\mathrm{r}$, where $\Delta_\mathrm{r} = \nu_\mathrm{r} - \nu_k$ is the detuning between the resonator frequency and the qubit frequencies. This results in two distinct resonances which represent the hybridized qubit states. The splitting $2J$ is extracted by fitting two Lorentzian lines[24]. By changing the resonator frequency, we determine the largest coherent qubit-qubit exchange rates of $2J/2\pi = 27\,\mathrm{MHz}$. When plotting $2J$ versus $1/\Delta_\mathrm{r}$, we find approximately the expected scaling (Fig. 2C and Fig. 2D). A linear fit results in $g_1 g_2/4\pi^2 = 0.25\,\mathrm{GHz}$, close to the expected $0.23\,\mathrm{GHz}$ from independent measurements of the coupling rates, $g_{1,2}$.

In the future, phtoton-mediated coupling will make two qubit gates between spatially separated charge or spin qubits possible. This is crucial for scaling up semiconductor-based quantum information devices[1,21].

Acknowledgments

We acknowledge contributions by C. K. Andersen, S. Gasparinetti, M. Collodo, J. Heinsoo, S. Storz, M. Frey, A. Stockklauser and M. Gabureac.

This work was supported by the Swiss National Science Foundation (SNF) through the National Center of Competence in Research (NCCR) Quantum Science and Technology (QSIT), the project Elements for Quantum Information Processing with Semiconductor/Superconductor Hybrids (EQUIPS) and by ETH Zurich.

---

[1] L. Vandersypen et al., npj Quantum Information **3**, 34 (2017).
[2] R. Hanson et al., Reviews of Modern Physics **79**, 1217 (2007).
[3] D. D. Awschalom et al., Science **339**, 1174 (2013).
[4] A. M. Tyryshkin et al., Nature materials **11**, 143 (2012).
[5] G. Shinkai et al., Physical review letters **103**, 056802 (2009).
[6] H.-O. Li et al., Nature communications **6**, 7681 (2015).
[7] D. R. Ward et al., npj Quantum Information **2**, 16032 (2016).
[8] M. D. Shulman et al., Science **336**, 202 (2012).
[9] M. Veldhorst et al., Nature **526**, 410 (2015).
[10] T. Watson et al., Nature (2018).
[11] F. R. Braakman et al., **8**, 432 (2013).
[12] T. A. Baart and ohers, **12**, 26 (2017).
[13] F. K. Malinowski, arXiv preprint arXiv:1706.03771 (2017).
[14] X. Mi et al., Science p. aal2469 (2016).
[15] A. Stockklauser et al., Physical Review X **7**, 011030 (2017).
[16] L. Bruhat et al., arXiv preprint arXiv:1612.05214 (2016).
[17] A. Landig et al., arXiv preprint arXiv:1711.01932 (2017).
[18] N. Samkharadze et al., Science **359**, 1123 (2018).
[19] A. Wallraff et al., Nature **431**, 162 (2004).
[20] J. Majer et al., Nature **449**, 443 (2007).
[21] L. Childress et al., Physical Review A **69**, 042302 (2004).
[22] D. J. van Woerkom et al., Unpublished (2018).
[23] P. Scarlino et al., arXiv preprint arXiv:1711.01906 (2017).
[24] D. Schuster et al., Physical review letters **94**, 123602 (2005).
[25] A. Wallraff et al., Physical review letters **95**, 060501 (2005).

Rényi entropy based EPR steering inequalities

Tamás Kriváchy,[1] Florian Fröwis,[1] and Nicolas Brunner[1]
[1] *Group of Applied Physics, University of Geneva, CH-1211 Geneva, Switzerland*

In bipartite steering one party (Alice) tries to influence the quantum state of another party. We derive conditional entropic uncertainty relations whose violation imply that steering is possible. In particular Rényi entropy-based relations are obtained which are tight in all dimensions for the case of Alice having two measurements in mutually unbiased bases mixed with white noise. The work also opens way to gaining more insight into the compatibility of measurements.

I. INTRODUCTION

The perplexing nonlocal nature of quantum systems was first encountered in Einstein, Podolsky and Rosen's (EPR) paradox[1], used as an argument that quantum mechanics is incomplete. Schrödinger shortly after introduced the term steering to describe the EPR situation,[2] where two parties, Alice and Bob, share a quantum state distributed to them from a source, and Alice is able to influence Bob's state through local operations (measurements) on her side. The effect was deemed unphysical in the early days, resolved through a local hidden variable (LHV) model by EPR or a local hidden state (LHS) model by Schrödinger. Much later the seminal work of Bell[3] showed that in quantum mechanics there are indeed cases which can not be explained by such LHV or LHS models, and opened up the way to understanding nonlocality. Through the formal connection of LHS models with steering it is now clear that every state exhibiting Bell nonlocality can demonstrate steering, and every steerable state is entangled[4], thus placing steering at an intermediate level between entanglement and Bell nonlocality.

II. EPR STEERING

In the task formulation of the steering scenario[4] Alice and Bob share many copies of a joint quantum state ρ_{AB}, given to them by a source. We say the state is steerable from Alice to Bob if Alice can preform local operations through which she can modify Bob's state. Bob, however, must verify that his state is indeed being steered and has not been prepared in some clever way. So for each copy of the state Bob asks Alice to steer either one way or the other (if Alice uses two measurements; however in general she can use more). Alice then tells Bob what measurement results she got so he can verify that indeed his state changed.[?] Bob gathers together statistics from Alice's and from his own measurements and tries to convince himself that indeed steering happened and there was not some tricky preparation of the states, that the results can't be explained by a LHS model.

A LHS model is one in which Bob receives a quantum state and Alice receives some classical information (about Bob's state) in each round, potentially different states in the rounds. So in such a model Alice could try to pretend that she steered Bob's state by using her information and a clever strategy to convey answers to Bob that he's expecting. For an illustration of the model see figure 1.

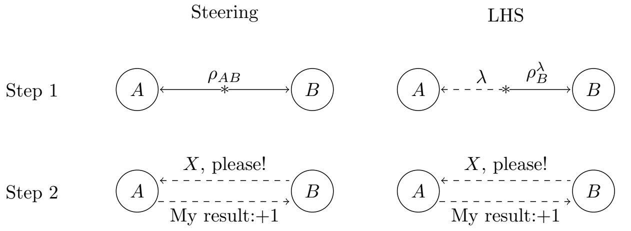

FIG. 1: In step 1, states are distributed to Alice and Bob. In a LHS model Alice only receives a classical state, λ. In step 2 Bob asks Alice to perform one of her measurements (here: X measurement), and Alice responds either based on her measurement (steering) or based on her received information and strategy (LHS). The two steps are repeated many times.

In the following we examine the steering scenario restricted to both Alice and Bob having only two measurements, denoted X_A, Z_A and X_B, Z_B, respectively.

III. RÉNYI STEERING INEQUALITIES

In previous works entropic steering inequalities have been derived using Shannon[5] and Tsallis[6] entropies from entropic uncertainty relation (URs), such as the Massen-Uffink one,[7]

$$H(X) + H(Z) \geq q(X, Z), \tag{1}$$

with the state-independent $q = -\log(c^2_{X,Z})$, where $c_{X,Z} = \max_{x,z} |\langle X_x | Z_z \rangle|$ is the maximum overlap between the eigenvectors of the X and Z measurement, and H denotes the Shannon entropy of the measurement results $H(X) = -\sum_x p_x \log p_x$ with $p_x = \mathrm{tr}(\rho |X_x\rangle\langle X_x|)$. From (1) one arrives at the steering inequality $H(X_B|X_A) + H(Z_B|Z_A) \geq q(X_B, Z_B)$, with the conditional Shannon entropy $H(X|Y) = \sum_y p(y) H(X|Y = y)$, the violation of which excludes the possibility of a LHS model.

The methods used in previous works are incompatible with Rényi entropies. In our approach we show that Rényi entropies can also be used for steering inequalities and that they outperform the others in commonly studied cases. We use the fact that in order to derive an entropic steering inequality the following two conditions are sufficient.

(i) The considered UR holds true when conditioned on a classical random variable Λ, i.e. $H(X|\Lambda) + H(Z|\Lambda) \geq q(X,Z)$.

(ii) The considered entropy must decrease under conditioning on additional information, i.e. $H(X) \geq H(X|Y)$

For the conditional Rényi entropy both conditions can be satisfied[8,9]. Using this we show that for $\alpha^{-1}+\beta^{-1}=2$, a LHS model implies

$$H_\alpha(X_B|X_A) + H_\beta(Z_B|Z_A) \geq q(X_B, Z_B), \tag{2}$$

i.e. a violation of this inequality excludes the existence of a LHS model. Thus it is in general a sufficient, but not necessary condition for steerability. In the following we show two cases where it is also a necessary condition.

IV. TIGHTNESS FOR WHITE NOISE

If Bob and Alice share a pure entangled state, steerability is equivalent to Alice using incompatible measurements, i.e. measurements which are not jointly measurable.[10,11] Thus the problem of determining whether Alice's measurements are jointly measurable can be examined through our entropic steering inequality (2).

Consider the case of Alice using mutually unbiased bases. Mutually unbiased bases are such that any basis elements from the two bases have the same overlap, $1/\sqrt{d}$. Let us consider the case when Alice uses the computational basis $\{|j\rangle_A\}_{j=1}^d$ for her measurement Z_A , its discrete Fourier transform $\{F|j\rangle_A\}_{j=1}^d$ for her X_A measurement, (generalizations of the Pauli σ_Z and σ_X in $d=2$) with

$$F = \frac{1}{\sqrt{d}} \sum_{j,k} \omega^{-jk} |j\rangle\langle k| \quad \text{with} \quad \omega = e^{2\pi i/d}. \tag{3}$$

These measurements are not jointly measurable. In order to nudge them towards being jointly measurable we add some white noise controlled by the parameter $\eta \in [0,1]$, such that both of Alice's measurement operators become white noise measurements in the limit of $\eta = 1$, as $Z_j^\eta := (1-\eta)|j\rangle\langle j| + \eta\mathbf{1}/d$, and similarly for her X_A measurements.

For this scenario it is straightforward to show that the exact threshold η^* above which the measurements Z_A^η and X_A^η are jointly measurable, is detectable by the violation of (2). In other words for any $\eta \geq \eta^*$ inequality (2) is satisfied, while for $\eta < \eta^*$ it is violated.

For $d=2$ tightness holds not just for the noisy computational and Fourier basis measurement, but for any two measurements on Alice's side, mixed with white noise.

V. CONCLUSION

In summary we have derived a new entropic steering inequality based on Rényi entropies. The derived inequality is tight for Alice having white noise on her measurements for $d=2$ and any measurements or for $d \geq 2$ for mutually unbiased bases.

Acknowledgments

We would like to thank Sébastien Designolle for his assistance with MUBs their exact noise thresholds, as well as Nicolas Gisin for his support. This project was supported by the European Research Council (ERC MEC).

---

[1] A. Einstein, B. Podolsky, and N. Rosen, *Can Quantum-Mechanical Description of Physical Reality Be Considered Complete?*, Phys. Rev. **47**, 777 (1935).

[2] E. Schrödinger, *Discussion of Probability Relations between Separated Systems*, Mathematical Proceedings of the Cambridge Philosophical Society **31**, 555 (1935), ISSN 1469-8064, 0305-0041.

[3] J. S. Bell, *On the Einstein Podolsky Rosen paradox*, Physics Physique Fizika **1**, 195 (1964).

[4] H. M. Wiseman, S. J. Jones, and A. C. Doherty, *Steering, Entanglement, Nonlocality, and the Einstein-Podolsky-Rosen Paradox*, Phys. Rev. Lett. **98**, 140402 (2007).

[5] S. P. Walborn, A. Salles, R. M. Gomes, F. Toscano, and P. H. Souto Ribeiro, *Revealing Hidden Einstein-Podolsky-Rosen Nonlocality*, Phys. Rev. Lett. **106**, 130402 (2011).

[6] A. C. S. Costa, R. Uola, and O. Gühne, *Steering criteria from general entropic uncertainty relations*, arXiv:1710.04541 [quant-ph] (2017), arXiv: 1710.04541.

[7] H. Maassen and J. B. M. Uffink, *Generalized entropic uncertainty relations*, Phys. Rev. Lett. **60**, 1103 (1988).

[8] P. J. Coles, R. Colbeck, L. Yu, and M. Zwolak, *Uncertainty Relations from Simple Entropic Properties*, Phys. Rev. Lett. **108**, 210405 (2012).

[9] M. Iwamoto and J. Shikata, Tech. Rep. 440 (2013).

[10] M. T. Quintino, T. Vértesi, and N. Brunner, *Joint Measurability, Einstein-Podolsky-Rosen Steering, and Bell Nonlocality*, Phys. Rev. Lett. **113**, 160402 (2014).

[11] R. Uola, T. Moroder, and O. Gühne, *Joint Measurability of Generalized Measurements Implies Classicality*, Phys. Rev. Lett. **113**, 160403 (2014).

[12] Note that without communication Bob couldn't notice any change in his marginal state $\rho_B = \mathrm{tr}_B(\rho_{AB})$.

Self-Catalyzed vertical GaAs nanotrees on Silicon

Oscar Garcia,[1] Lucas Güniat,[1] David Vindice,[1] Wonjong Kim,[1] Martin Friedl,[1]
Akshay Balgarkashi,[1] Jean-Baptiste Leran,[1] and Anna Fontcuberta i Morral[1]
[1]Laboratory of Semiconductor Materials, EPFL, CH-1015, Lausanne, Switzerland

In our aim to grow vertical self-catalyzed nanowires on [100] Si substrate we found the presence of a fancy triangular-shaped nanowire that we named nanotree. The present work explores this new promising structure that may be useful for light confinement in optoelectronic devices.

I. INTRODUCTION

III-V semiconductors offer, due to their high carrier mobility and direct bandgap, a great potential for optoelectronic applications, from detectors to emitting diodes[8] and solar cells[7]. However, III-V are scarce, and their use should be very well assessed. To reduce the amount of III-V material used, a deposition over a Silicon substrate can be done. Using Molecular Beam Epitaxy (MBE), a III-V thin film deposition over a Si wafer can be easily performed. Though, many defects appear due to lattice mismatch. An alternative to thin films can be found in nanowires.

Nanowires are elongated nanostructures with a reduced diameter, about hundreds of nanometers. When grown over a Si substrate, they show a strain relaxation at the interface due to their reduced cross-section, which leads to overcome lattice mismatch. Furthermore, nanowires can be tuned to show desired optoelectronic properties by combining different MBE grown layers, obtaining different quantum confined structures[3].

Silicon based technologies commonly use [100] wafers. The present work aims to build III-V nanowires over [100] Si in order to obtain procedures compatible with the current industry. The growth of the nanowire is made through Vapor-Liquid-Solid (VLS). In this technique, precursor droplets are placed over the substrate. This precursor contains the core components of the nanowire, III-V elements, and typically Gold acting as a catalyzer. The presence of Gold nanoparticles, which act as a seed, is useful to tune the nanowire characteristics[1], such as its diameter. However, the presence of Gold could lead to defects in the nanowire and creates deep-level traps in the Si wafer. This defects are reflected in a drastic decrease of the optoelectronic properties of the nanowire. For this reason, self-catalyzed method is purposed, where the precursor droplet only contains the III-V elements and the nanowire characteristics are tuned through the substrate and the droplet characteristics.

II. BIRTH OF NANOTREES

Results of a growth using this procedure are shown in figure 1. As it can be seen, mostly tilted structures appear, due to the preferential stable growth direction [111][6]. However, other more complex structures can be seen, forming a triangular shape called nanotree. This is the evidence that epitaxial growth in [100] direction can be achieved with a self-catalyzed approach. From now on, the work will be focused on this nanotree structures. Tuning the process characteristics, such as the partial pressure of As and Ga during Molecular Beam Epitaxy, more elongated or shortened nanotrees are obtained. It is expected to achieve a yield of about 10% of nanotrees with respect to the other types of structures.

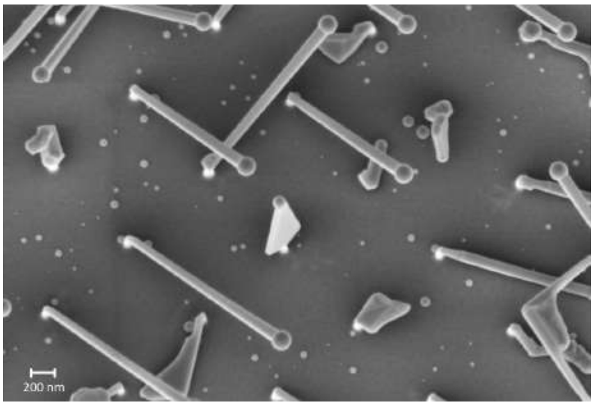

FIG. 1: 20° tilted SEM image of self-catalyzed growth on [100] Si substrate. A vertical nanotree can be observed with a white tonality in the center of the picture, while in its surrounding [111] nanowires are present.

In order to characterize this novel type of nanowire, nanotrees are extracted from the sample and transferred to another substrate, where they are isolated. Different optical techniques are used for characterization. Bulk GaAs show zinc-blend structure. However, in a nanowire, wurtzite structure can also be observed[5]. By means of micro Raman spectroscopy the presence of this phases can be determined. Due to the different phonon dispersion in zinc-blend and wurtzite, different shifts are observed in the spectra. Furthermore, surface modes that are not predicted by Raman theory for bulk material may be present in nanotrees[10].

The quality of the crystalline structure can be observed through photoluminescence and cathodoluminescence techniques[4] . Defects in the crystals create intermediate levels that widen the photoluminescence

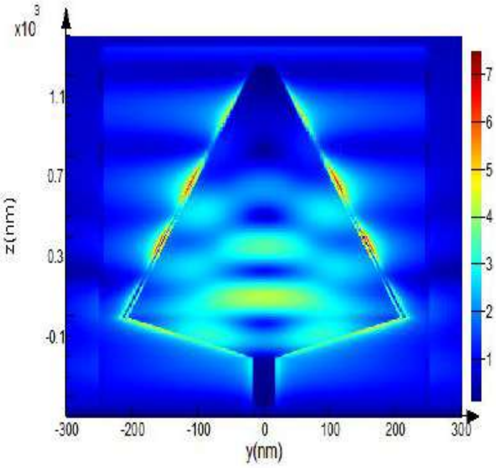

FIG. 2: Normalized electric field intensity FDTD simulations that show an electric field enhancement inside the nanotree.

spectra. Thus, this techniques allow to qualitatively compare the presence of defects in the nanostructures.[2]

III. THEIR FUTURE IS BRIGHT

Thanks to their shape and composition, nanotrees seem to be a promising nanostructure for optoelectronic devices. In order to probe into its interaction with light, a set of FDTD simulations was run. A nanotree model was constructed and a vertically incident planar wave polarized along y axis was simulated. Figure 2 shows an electric field intensity map resulting from this simulation. As it can be seen, there is a clear enhancement of the electric field inside the nanotree, thus revealing that this shape holds a good light confinement.

Nanowires are the perfect cradle to host quantum confinement. A set of GaAs-AlGaAs layers creates a quantum well that could extend along the nanotree axis in the form of a quantum wire[9]. It is believed that nanotrees will enhance this phenomena due to a more sharpened vertices. Furthermore, it has been shown in previous works that quantum dots can also be created at the vertices of a nanowire.

The fact that nanotrees show a good light confinement and the capability to host customized quantum confinement makes them a promising candidate for high efficiency optoelectronic devices such as emitting diodes and detectors.

Acknowledgments

We would like to thank Jordi Arbiol and Sara Martí, from ICN2, for their work on modeling the crystalline structure of nanotrees.

---

[1] MT Björk, BJ Ohlsson, T Sass, AI Persson, Claes Thelander, MH Magnusson, Knut Deppert, LR Wallenberg, and Lars Samuelson. One-dimensional heterostructures in semiconductor nanowhiskers. *Applied Physics Letters*, 80(6):1058–1060, 2002.

[2] Jessica L Boland, Sonia Conesa-Boj, Patrick Parkinson, Gozde Tutuncuoglu, Federico Matteini, Daniel Ruffer, Alberto Casadei, Francesca Amaduzzi, Fauzia Jabeen, Christopher L Davies, et al. Modulation doping of gaas/algaas core–shell nanowires with effective defect passivation and high electron mobility. *Nano letters*, 15(2):1336–1342, 2015.

[3] Maria De La Mata, Xiang Zhou, Florian Furtmayr, Jörg Teubert, Silvija Gradečak, Martin Eickhoff, Anna Fontcuberta i Morral, and Jordi Arbiol. A review of mbe grown 0d, 1d and 2d quantum structures in a nanowire. *Journal of Materials Chemistry C*, 1(28):4300–4312, 2013.

[4] D Gershoni, M Katz, Werner Wegscheider, LN Pfeiffer, RA Logan, and K West. Radiative lifetimes of excitons in quantum wires. *Physical Review B*, 50(12):8930, 1994.

[5] Frank Glas, Jean-Christophe Harmand, and Gilles Patriarche. Why does wurtzite form in nanowires of iii-v zinc blende semiconductors? *Physical review letters*, 99(14):146101, 2007.

[6] Daniel Jacobsson, Federico Panciera, Jerry Tersoff, Mark C Reuter, Sebastian Lehmann, Stephan Hofmann, Kimberly A Dick, and Frances M Ross. Interface dynamics and crystal phase switching in gaas nanowires. *Nature*, 531(7594):317, 2016.

[7] Peter Krogstrup, Henrik Ingerslev Jørgensen, Martin Heiss, Olivier Demichel, Jeppe V Holm, Martin Aagesen, Jesper Nygard, and Anna Fontcuberta i Morral. Single-nanowire solar cells beyond the shockley–queisser limit. *Nature Photonics*, 7(4):306, 2013.

[8] Dhruv Saxena, Sudha Mokkapati, Patrick Parkinson, Nian Jiang, Qiang Gao, Hark Hoe Tan, and Chennupati Jagadish. Optically pumped room-temperature gaas nanowire lasers. *Nature Photonics*, 7(12):963, 2013.

[9] W Wegscheider, LN Pfeiffer, MM Dignam, A Pinczuk, KW West, SL McCall, and R Hull. Lasing from excitons in quantum wires. *Physical Review Letters*, 71(24):4071, 1993.

[10] I Zardo, S Conesa-Boj, F Peiro, JR Morante, J Arbiol, E Uccelli, G Abstreiter, and A Fontcuberta i Morral. Raman spectroscopy of wurtzite and zinc-blende gaas nanowires: polarization dependence, selection rules, and strain effects. *Physical review B*, 80(24):245324, 2009.

Shiba states in the presence of spin-orbit interaction

Oindrila Deb[1]
[1] *Department of Physics, University of Basel, Klingelbergstrasse 82, CH-4056 Basel, Switzerland*

I. INTRODUCTION

In a conventional s-wave superconductor, quasiparticle excitations are gapped due to the formation of the superconducting gap. In the presence of magnetic impurities (such as atoms of 3d or 4f metals with a net magnetic moment) deposited on the surface of an s-wave superconductor [such as niobium (Nb) or lead (Pb)], the exchange interaction can induce a bound state within the gap known as a Yu-Shiba-Rusinov (YSR) or Shiba state[1]. There has been detailed study, both experimentally and theoretically[2–15] on the Shiba states. Recently, these states have attracted much attention in the context of magnetic impurity chains in which, when sufficiently close together, individual Shiba states can hybridize with adjacent bound states to form a band within the superconducting gap that can host Majorana fermions at its ends[16–25]. As mentioned earlier, the local magnetic moment of the impurity atoms is associated with their spin-split d-levels which will typically be far in energy from the Fermi level of the substrate superconductor. Then, the low-energy physics of the impurity atoms can be described in terms of its magnetic moment while its electronic degrees of freedom are effectively frozen out. The large impurity spin S is exchanged coupled to the electrons of the superconductor and can be approximated as classical[4,6,26].

Spin-polarized STM studies also indicate that in magnetic arrays with $\gtrsim$10 atoms spin dynamics is greatly suppressed[27]. It is, therefore, reasonable to model moments of magnetic atoms as static classical spins. In general, magnetic moments in these chains can form various configurations including a spiral[28].

Our aim is to see what happens to the Shiba bound states when spin-orbit interaction is present in the system along with the conventional superconductivity.

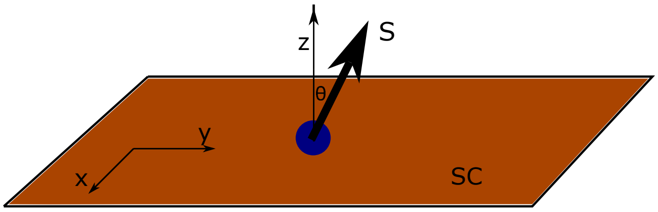

FIG. 1: A magnetic impurity sitting on an s-wave superconductor with classical spin S and oriented at an angle θ with respect to the z-axis.

II. THE HAMILTONIAN

For a single magnetic impurity placed at the origin, the Hamiltonian looks like :

$$H = \epsilon_{\mathbf{p}}\tau_z - J\vec{S}\cdot\vec{\sigma}\delta(\mathbf{r}) + \Delta\tau_x \tag{1}$$

Here, $\mathbf{p}$ and $\mathbf{r}$ denote the electron's momentum and position, $\epsilon_{\mathbf{p}} = \mathbf{p}^2/2m - \mu$ with the chemical potential μ, Δ is the superconducting gap, and J denotes the strength of the exchange coupling between the magnetic impurity with spin S and the electrons in the superconductor. The Pauli matrices σ_i (τ_i) operate in spin (particle-hole) space. The Hamiltonian is written in a basis which corresponds to the four-component Nambu operator $\Psi = [\psi_\uparrow, \psi_\downarrow, \psi_\downarrow^\dagger, -\psi_\uparrow^\dagger]^T$in terms of the electronic field operator $\psi_\sigma(\mathbf{r})$.

It can be shown analytically that the Hamiltonian has subgap solutions at energy $\pm E_b$ with[1,9]

$$E_b = \Delta\frac{1-\alpha^2}{1+\alpha^2} \tag{2}$$

where $\alpha = \pi\nu_0 JS$ in terms of normal-phase density of states ν_0. These subgap states are the Shiba states that appear due to the presence of magnetic impurity. These Shiba bound states possess two important properties. First, they are spin polarized, with the spin pointing parallel to the direction of S. Second, their wave function is localized around the impurity, decaying as $1/r$ for distances r smaller than the (energy-dependent) coherence length of the superconductor and exponentially beyond this length.

In our project we want to see the effect of spin-orbit interaction on the Shiba states and how their energy changes as a function of the spin-orbit strength.

Acknowledgments

I acknowledge support from the Swiss NSF and NCCR QSIT.

---

[1] L. Yu, Acta Phys. Sin. **21**, 75 (1965); H. Shiba, Prog. Theor. Phys. **40**, 435 (1968); A. I. Rusinov, Sov. Phys. JETP Lett. **9**, 85 (1969).

[2] A. Sakurai, Prog. Theor. Phys. **44**, 1472 (1970).

[3] A. Yazdani, B. A. Jones, C. P. Lutz, M. F. Crommie, and D. M. Eigler, Science **275**, 1767 (1997).

[4] M. E. Flatte and J. M. Byers, Phys. Rev. Lett. **78**, 3761 (1997).

[5] M. E. Flatte and J. M. Byers, Phys. Rev. B **56**, 11213 (1997).

[6] M. I. Salkola, A. V. Balatsky, and J. R. Schrieffer, Phys. Rev. B **55**, 12648 (1997).

[7] M. E. Flatte and J. M. Byers, Solid State Physics **52**, 137 (1999).

[8] M. E. Flatte and D. E. Reynolds, Phys. Rev. B **61**, 14810 (2000).

[9] A. V. Balatsky, I. Vekhter, and J.-X. Zhu, Rev. Mod. Phys. **78**, 373 (2006).

[10] S.-H. Ji, T. Zhang, Y.-S. Fu, X. Chen, X.-C. Ma, J. Li, W.-H. Duan, J.-F. Jia, and Q.-K. Xue, Phys. Rev. Lett. **100**, 226801 (2008).

[11] N. Y. Yao, L. I. Glazman, E. A. Demler, M. D. Lukin, and J. D. Sau, Phys. Rev. Lett. **113**, 087202 (2014).

[12] N. Y. Yao, C. P. Moca, I. Weymann, J. D. Sau, M. D. Lukin, E. A. Demler, and G. Zarand, Phys. Rev. B **90**, 241108 (2014).

[13] A. A. Zyuzin and D. Loss, Phys. Rev. B **90**, 125443 (2014).

[14] T. Meng, J. Klinovaja, S. Hoffman, P. Simon, and D. Loss, Phys. Rev. B **92**, 064503 (2015).

[15] M. Ruby, F. Pientka, Y. Peng, F. von Oppen, B. W. Heinrich, and K. J. Franke, Phys. Rev. Lett. **115**, 087001 (2015).

[16] S. Nadj-Perge, I. K. Drozdov, B. A. Bernevig, and A. Yazdani, Phys. Rev. B **88**, 020407 (2013).

[17] J. Klinovaja, P. Stano, A. Yazdani, and D. Loss, Phys. Rev. Lett. **111**, 186805 (2013).

[18] M. M. Vazifeh and M. Franz, Phys. Rev. Lett. **111**, 206802 (2013).

[19] B. Braunecker and P. Simon, Phys. Rev. Lett. **111**, 147202 (2013).

[20] S. Nakosai, Y. Tanaka, and N. Nagaosa, Phys. Rev. B **88**, 180503 (2013).

[21] F. Pientka, L. I. Glazman, and F. von Oppen, Phys. Rev. B **88**, 155420 (2013).

[22] I. Reis, D. J. J. Marchand, and M. Franz, Phys. Rev. B **90**, 085124 (2014).

[23] S. Nadj-Perge, I. K. Drozdov, J. Li, H. Chen, S. Jeon, J. Seo, A. H. MacDonald, B. A. Bernevig, and A. Yazdani, Science **346**, 602 (2014).

[24] R. Pawlak, M. Kisiel, J. Klinovaja, T. Meier, S. Kawai, T. Glatzel, D. Loss, and E. Meyer, npj Quantum information **2**, 16035 (2016).

[25] A. Heimes, P. Kotetes, and G. Schon, Phys. Rev. B **90**, 060507 (2014).

[26] A. Yazdani, B. A. Jones, C. P. Lutz, M. F. Crommie, and D. M. Eigler, Science **275**, 1767 (1997).

[27] S. Loth, S. Baumann, C. P. Lutz, D. M. Eigler, and A. J. Heinrich, Science **335**, 196 (2012).

[28] M. Menzel, Y. Mokrousov, R. Wieser, J. E. Bickel, E. Vedmedenko, S. Blugel, S. Heinze, K. von Bergmann, A. Kubetzka, and R. Wiesendanger, Phys. Rev. Lett. **108**, 197204 (2012).

Single spin magnetometry at mK-temperatures for the investigation of strongly correlated electron systems

Jodok Happacher,[1] Dominik Rohner,[1] Marcel.li Grimau Puigibert,[1] and Patrick Maletinsky[1]

[1] *Quantum Sensing Group, Universität Basel, CH-4096, Basel, Switzerland*

Scanning single spin magnetometry with Nitrogen Vacancy (NV) spins has emerged as a robust and powerful technique for the spatial imaging of mesoscopic magnetic systems. The high sensitivity combined with the nanoscale resolution extends experimental possibilities beyond the limits of other comparable sensing techniques and allows localized studies of electron correlations and electron spins. Strongly correlated electron systems have very particular intrinsic properties which were mostly studied in bulk. These materials have phase transitions with different electronic and magnetic orders accessible to a scanning NV-magnetometer. In this project, we will look at emergent quantum properties of strongly correlated electron systems such as unconventional superconductors, quantum Hall systems or multiferroics at temperatures around 100mK to improve our microscopic understanding of electronic correlations occurring in this regime.

I. INTRODUCTION

The investigation of strongly correlated electron systems requires outstanding magnetic sensing capabilities due to the nature of electron correlations and quantum transitions. Imaging exotic or possibly competing phases governed by different ordering phenomena poses significant experimental challenges.

For many physical systems of interest, ultra-low temperatures below 100mK are needed to get into the considered regime. This requires a system with good thermalization and a measurement technique with a small heat footprint.

Due to these difficulties, recent studies mainly addressed the bulk properties of these materials and could not observe quantum matter at the nanoscale owing to a lack of spatial resolution or sensitivity.

Nitrogen Vacancy (NV) based magnetic imaging does not have these shortcomings and provides a robust and powerful tool for quantitative nanoscale sensing. It is unique in providing the necessary sensitivity as well as spatial resolution for a venture into a variety of novel measurements.[1–3]

In this project, NV-magnetometry is implemented in a closed-cycle dilution refrigeration system operating at around 100mK, extending the possibilities beyond current experimental limitation[4,5] in the investigation of strongly correlated materials. The first pursued areas of interest involve the study of magnetism in oxide heterostructures with further applications in graphene, and unconventional superconductors being on the horizon.

II. EXPERIMENTAL SYSTEM

NV centers are point size defects in diamond formed by a nitrogen atom and a neighboring vacancy (Fig. 1b). The electronic structure in the ground state of a negatively charged NV can be described by $S = 1$ spin system as shown in Fig. 1c where m_s denotes the magnetic quantum number along the spins quantisation axis formed by the NV symmetry axis. The $m_s = 0$ state and the two degenerate $m_s = \pm 1$ states exhibit a highly spin dependent fluorescence due to the specifics of the NV's photophysical properties.[1] This effect can be used to optically detect electron spin resonance (ESR).[6] The NV can be optically excited with a green laser leading to an initialization into the bright $m_s = 0$ state. Manipulation with microwaves can pump the spin into one of the $m_s = \pm 1$ states with a reduced luminescence intensity.

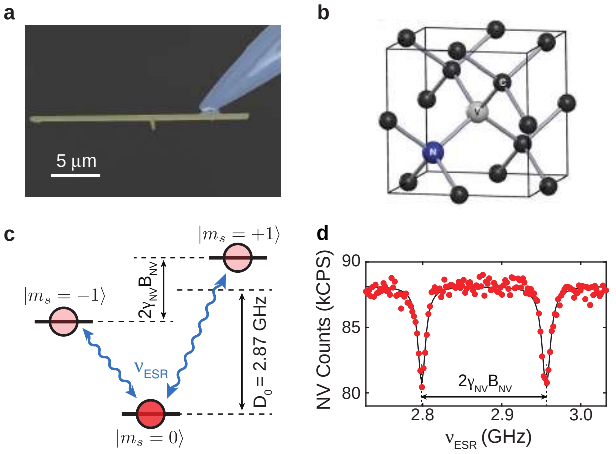

FIG. 1: **Basic properties of Nitrogen-Vacancy (NV) centers.** a) Scanning electron microscope picture of the diamond scanning probe[7] attached to the end of a quartz tip. The NV center is located in the tip of the nanopillar. b) Structure of the NV inside the diamond crystal lattice (adapted from [8]). c) Diagram of the ground-state electronic (spin-triplet) level structure of the NV center in an external magnetic field B_{NV} along the NV axis ($\gamma_{NV} \approx 2.8$MHz/G) lifting the degeneracy of the $m_s = \pm 1$ states. Microwaves (ν_{ESR}) can be used to drive optically detected electron spin resonance (ESR). d) ESR showing the Zeemann splitting between $m_s = -1$ and $m_s = +1$.

In the presence of a magnetic field along the NV symmetry axis the $m_s = \pm 1$ sublevels split due to the Zeeman effect (Fig. 1d). This can be exploited for magnetic imaging with sensitivities of a few $\mu T/\sqrt{Hz}$[9] which can be improved to the $nT/\sqrt{Hz}$ range[10] by coherent spin manipulation and dynamical decoupling.[11]

In the current approach the NV center is located in an all-diamond scanning probe[7] (Fig. 1a) a few 10's of nanometres from the diamond surface.[10] Therefore a close proximity to the sample can be achieved during scanning, thus allowing nanoscale spatial resolution.[10] The scanning probe itself is mounted on a tuning fork which is part of an atomic force microscope (AFM) with the purpose of precisely navigating the sensor to sample distance.

The experiment is performed in a closed-cycle refrigerator at a temperature of around 100mK. The cryostat posesses a free-space optical access allowing the optical initialization and read-out of the NV through a confocal microscope (CFM). One of the major challenges in the operation of such a system at cryogenic temperatures is the heat load of the measurement system. Therefore the nanopillar comprising the all-diamond scanning probe (Fig. 1a) is designed to enhance the collection efficiency due to its special waveguide properties[12]. It thereby maximizes spin-readout efficiency at low laser powers while pulsed measurement techniques are used to minimize laser and microwave heating.

III. MAGNETISM IN OXIDE INTERFACES

In recent years oxide interfaces have attracted notable attention due to their extraordinary properties.[13] The lanthanum aluminate ($LaAlO_3$) and strontium titanate ($SrTiO_3$) interface is one of the most prominent examples. The two oxide components themselves are non-magnetic and form perfect insulators, but when stacked together a 2D electron gas forms at the interface which has a high carrier concentration.[14] The material can show a variety of phenomena such as electrical conductivity[14], superconductivity[15], ferromagnetism[16], and magnetoresistance[17].

Scanning NV-magnetometry has been performed on the oxide interface for the investigation of its magnetic properties. The high sensitivity combined with unprecedented spatial resolution would allow to resolve the microscopic structure of individual magnetic patches which have been reported in [16]. However, in preliminary measurements at 4K no magnetic field was detected questioning the nature of the observed magnetism and highlighting the need for further investigations.

The charge transport in the system is not yet fully understood and can be studied by imaging stray magnetic fields with a NV-magnetometer. But current imaging remains challenging due to the limitations on the maximum current which can be applied to the thin film. In the upcoming measurements we will apply strong magnetic fields to the material in order to push the conductive channels to the edges resulting in higher detectable fields. Further investigations will focus on the transition process to superconductivity.

IV. OUTLOOK

There are two other materials which will be considered in the investigation of strongly correlated electron systems: graphene and strontium ruthanate (Sr_2RuO_4). Both exhibit a variety of unusual electronic and transport properties due to their highly two-dimensional electronic structure[18,19] and allow the study of quantum Hall systems and unconventional superconductivity at low temperatures.

NV-magnetometry can help to improve the microscopic understanding of these phenomena and help understand the nature of spin-ordering in graphene and the role of magnetism in p-wave superconductivity.

Acknowledgments

We would like to acknowledge the support of QSIT, the Swiss National Science Foundation and the EU FET project, DIADEMS.

---

[1] G. Balasubramanian et al., Nature **455**, 648 (2008).

[2] J. M. Taylor et al., Nature Physics **4**, 810 (2008).

[3] P. Appel et al., New J. Phys. **17**, 112001 (2015).

[4] E. Schaefer-Nolte et al., Review of Scientific Instruments **85**, 013701 (2014).

[5] L. Thiel et al., Nature Nanotechnology **11**, 677 (2016).

[6] A. Gruber et al., Science **276**, 2012 (1997).

[7] P. Appel et al., Review of Scientific Instruments **87**, 063703 (2016).

[8] N. Bar-Gill et al., Nature Communications **4**, 1743 (2013).

[9] L. Rondin et al., Reports on Progress in Physics **77**, 056503 (2014).

[10] P. Maletinsky et al., Nature Nanotechnology **7**, 320 (2012).

[11] G. de Lange et al., Phys. Rev. Lett. **106**, 080802 (2011).

[12] N. H. Wan et al., Nano Lett. **18**, 2787 (2018).

[13] P. Zubko et al., Annual Review of Condensed Matter Physics **2**, 141 (2011).

[14] A. Ohtomo et al., Nature **427**, 423 (2004).

[15] S. Gariglio et al., J. Phys.: Condens. Matter **21**, 164213 (2009).

[16] J. A. Bert et al., Nature Physics **7**, 767 (2011).

[17] M. Ben Shalom et al., Phys. Rev. Lett. **104**, 126802 (2010).

[18] A. F. Young et al., Nature Physics **8**, 550 (2012).

[19] K. D. Nelson et al., Science **306**, 1151 (2004).

Tayloring excitonic insulators in InAs/(AlSb)/GaSb bilayer systems

Amina S. L. Ribeiro,[1] Ruediger Schott,[1] Werner Dietsche,[1] and Werner Wegscheider[1]
[1]*Advanced Semiconductor Quantum Materials Group,*
Physics Department ETH-Hönggerberg, CH-8093, Zürich, Switzerland

The bilayer system InAs/(AlSb)/GaSb consists on having the bottom of InAs conduction band lying on a lower energy level than the top of GaSb valence band creating an inverted band structure that provides a unique 2D semiconductor system, which allows to have electrons and holes coexisting in the same material simultaneously. Therefore, it has attracted attention due to the possibility of excitonic interactions which can be controlled by varying the thickness and height of an $Al_xGa_{1-x}Sb$ middle barrier. Those interactions can induce the system into a phase transition generating an excitonic insulator (EI). Depending on the pair electron-hole density and the temperature, the system can be described by EI or exciton Bose-Einstein Condensate. In this work, we will study the possibility of formation of an EI in InAs/(AlSb)/GaSb quantum wells exploring its electrical properties via magnetotransports measurements.

I. INTRODUCTION

The inverted band structure of the bilayer semiconductor system InAs/GaSb relies on the fact that the bottom of InAs conduction band remains in a lower energy level compared to the top of GaSb valence band. This specific sample structure represented in FIG. 1, shows a physical system which has the coexistence of two-dimensional electron gas (2DEG) for InAs and two-dimensional hole gas (2DHG) for GaSb, simultaneously.

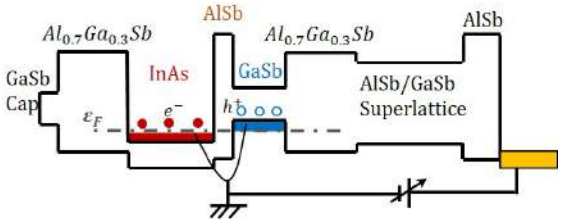

FIG. 1: Diagram of sample structure. Adapted from[1].

This coexistence of electrons (e) and holes (h) allows their coupling due to the Coulomb interaction of $e - h$ pair, creating excitons (bound state), which can induce an insulating state, called excitonic insulator (EI) or Bardeen-Cooper-Schrieffer (BCS) excitonic condensation[1–3].

The FIG.2 represents the phase diagram for an $e - h$ system in the parameter space of temperature and pair density for InAs/GaSb bilayer systems. As shown in FIG.2, once we increase the pair density and temperature, we cover the Bose-Einstein Condensate (BEC) superconducting regime, where the exciton states are degenerate. If one proceed increasing the density, the system achieves a critical temperature T_c, indicating the maximum excitonic coupling, providing the phase transition when temperature decreases, holding a behaviour where electrons and holes are weakly bound, like Cooper pairs, defining the EI regime. Hence, depending on the pair density of excitons, there are 2 distinct physical regimes, the exciton BEC or EI.

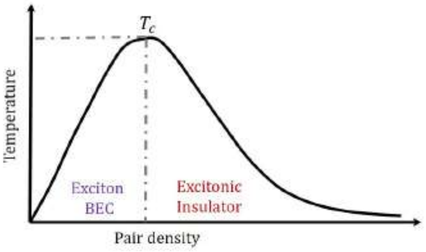

FIG. 2: Phase diagram for $e - h$ pair in InAs/GaSb system. Adapted from[2].

II. OUTLOOK OF RESEARCH PLAN

The heterostructure scheme of interest is illustrated in FIG. 1, consisting of a InAs/(AlSb)/GaSb bilayer system, where we use a front gate to tune the charge density and a GaSb conductive substrate acting as a back gate. The quantum wells (QWs) were sandwiched between $Al_{0.7}Ga_{0.3}Sb$ barriers. In order to control the strengh of excitonic coupling, one can vary the AlSb middle barrier between InAs 2DEG and GaSb 2DHG.

Such a structure allows one to infer the Landau-Levels (LLs) and filling factors of the 2DEG and the 2DHG respectively. However, the quantization mechanism of the Hall resistance in these structures is not completely understood, keeping this unexplored research area very interesting.

In this work, we will investigate the transport phenomena related to Quantum Hall Effect (QHE) in InAs/(AlSb)/GaSb QWs, which seems to differ from conventional bilayer systems[4,5]. We plan to study the behavior of electrons and holes varying the thicknesses of the AlSb middle barrier, the height of this middle barrier by using $Al_xGa_{1-x}Sb$ instead; the thickness of InAs/(AlSb)/GaSb QWs and also see if the transport mechanism changes if one uses doped or undoped substrates for the sample.

Acknowledgments

We would like to acknowledge the NCCR QSIT and Swiss NSF for financial support.

[1] K. Suzuki, K. Takashina, S. Miyashita, and Y. Hirayama, *Landau-level hybridization and the quantum hall effect in* InAs/(AlSb)/GaSb *electron-hole systems*, Phys. Rev. Lett. **93**, 016803 (2004), URL `https://link.aps.org/doi/10.1103/PhysRevLett.93.016803`.

[2] L. Du, X. Li, W. Lou, G. Sullivan, K. Chang, J. Kono, and R.-R. Du, *Evidence for a topological excitonic insulator in inas/gasb bilayers*, Nature Communications **8**, 1971 (2017), URL `https://doi.org/10.1038/s41467-017-01988-1`.

[3] Y. Naveh and B. Laikhtman, *Excitonic instability and electric-field-induced phase transition towards a two-dimensional exciton condensate*, Phys. Rev. Lett. **77**, 900 (1996), URL `https://link.aps.org/doi/10.1103/PhysRevLett.77.900`.

[4] H. L. Stormer, Z. Schlesinger, A. Chang, D. C. Tsui, A. C. Gossard, and W. Wiegmann, *Energy structure and quantized hall effect of two-dimensional holes*, Phys. Rev. Lett. **51**, 126 (1983), URL `https://link.aps.org/doi/10.1103/PhysRevLett.51.126`.

[5] K. v. Klitzing, G. Dorda, and M. Pepper, *New method for high-accuracy determination of the fine-structure constant based on quantized hall resistance*, Phys. Rev. Lett. **45**, 494 (1980), URL `https://link.aps.org/doi/10.1103/PhysRevLett.45.494`.

The Casimir effect in periodic systems

Aleksandra Nelson[1] and Valery Marachevsky[2]
[1]*Physik-Institut, Universität Zürich, CH-8057 Zürich, Switzerland.*
[2]*Division of Theoretical Physics, Physical Department, Saint Petersburg State University, 198504, Ulianovskaya str. 1, Petrodvorets, Saint Petersburg, Russia.*

Recently the Casimir effect has become a problem of a great interest. One system that was investigated throughout the last decades is the system of two periodical gratings separated by a vacuum slit. In this work, we calculated the Casimir forces between two periodical bodies with sinusoidal surfaces. We analyzed the dependence of the Casimir force on the separation distance and on the corrugated region width.

I. INTRODUCTION

The Casimir effect is a physical problem at the intersection of two fields: quantum electrodynamics and condensed matter theory. In the theory of quantum electrodynamics, there always exist the vacuum zero energy which includes zero energies of all quantum oscillators in the free space.

$$E = \sum_i \frac{\hbar\omega_i}{2} \tag{1}$$

This energy is equal to an infinite constant in the case of free space. However, in the presence of boundaries, we can extract from this constant a finite term that depends on the system parameters, such as distances, shapes or others. Thus we can expect the existence of the force between those boundaries.

The declared effect was first predicted in 1948 by H. B. G. Casimir[1] who considered a system of two perfectly conducting planes and derived an attractive force between them:

$$F = \hbar c \frac{\pi^2}{240} \cdot \frac{1}{d^4}. \tag{2}$$

This result was later generalized to the case of arbitrary dielectric semispaces by Dzyaloshinskii, Lifshitz and Pitaevskii[2]. The material properties were defined by the model of dielectric permittivity.

The first experimental evidence of the Casimir effect came to light in 1958 when the force between two dielectrics was measured by Derjaguin and Abrikossova[3]. Despite some inaccuracy of the results the experiment successfully demonstrated the existence of the Casimir forces.

Throughout the last decades, the interest in the Casimir effect has been rising among the scientists. And they began to expand their research to the nonplanar geometries. For some artificial shapes of the system there was a semi-analytical solution, however, the most crucial breakthrough came with several computational techniques[4] that allowed solving the systems with arbitrary geometries, that required a reasonable computational time.

These computational methods someway reduce the Casimir force calculations to a classical scattering problem of a set of incident waves or to a response of the fields in the media to some current sources.

II. THE SYSTEM OF PERIODICAL GRATINGS

The described group of methods was applied for the case of gratings periodical in one spatial direction and translational invariant in the orthogonal direction. A. Lambrecht and V. Marachevsky[5] in 2008 suggested using the Rayleigh decompositions[6] as incident waves in such systems. The developed formalism was valid for arbitrary periodical surfaces of the gratings and arbitrary materials, defined by frequency dependence of dielectric permittivity.

Through the use of the developed formalism, it was demonstrated that the calculated Casimir forces coincide with the experimental measurements[7].

III. GENERALIZATION TO THE 2D PERIODICITY

In our work, we generalized the method developed by Lambrecht and Marachevsky[5] to the case of gratings periodical in two orthogonal directions (Fig. 1).

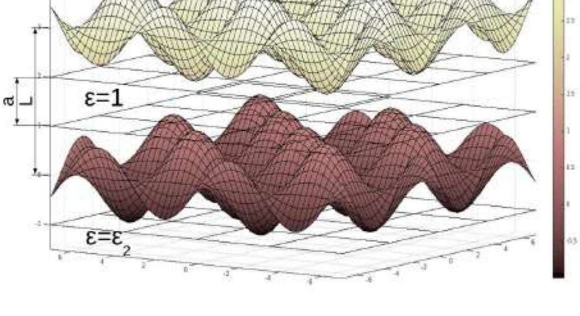

FIG. 1: Gratings periodical in two directions.

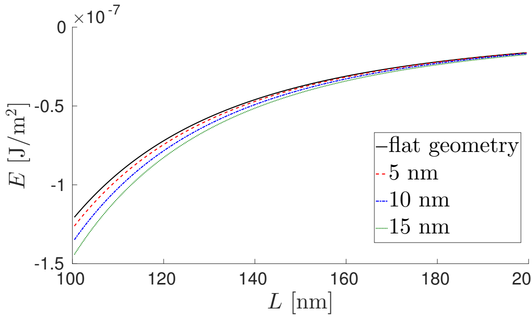

FIG. 2: The Casimir energy E of two 2d sinusoidal Si gratings with corrugation amplitudes $b = 5, 10, 15$ nm. The Lifshitz energy of two Si semispaces is shown by a black solid line.

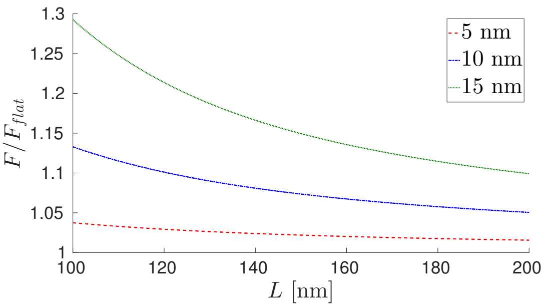

FIG. 3: Ratios of the normal force F between two 2d sinusoidal Si gratings to the Lifshitz force F_{flat} between two Si semispaces.

We also applied the suggested formalism to the Casimir force calculations in the systems with a sinusoidal shape[8]. The surface profile of each grating was defined by a function $f(x, y) = b\cos(2\pi x/d_x)\cos(2\pi y/d_y)$. L was a distance between middle planes of corrugation regions of the gratings (Fig.1).

For better convergence, we choose gratings made of silicon. We used the one oscillator model of dielectric permittivity:

$$\varepsilon_{Si}(i\omega) = \varepsilon_\infty + (\varepsilon_0 - \varepsilon_\infty)\frac{\omega_0^2}{\omega_0^2 + \omega^2}, \qquad (3)$$

with parameters $\varepsilon_\infty = 1.035$, $\varepsilon_0 = 11.87$, $\omega_0 = 6.6 \cdot 10^{15}\,\frac{rad}{s}$.

Here we present the calculated Casimir energy E at zero temperature $T = 0$ for several values of corrugation amplitudes $b = 5, 10, 15$ nm (Fig. 2). The periods of gratings are selected to be $d_x = d_y = 100$ nm. We compare the results with the Lifshitz energy[2] of two Si semispaces separated by a vacuum slit L.

We also show the ratios of the normal Casimir forces between two 2d sinusoidal Si gratings $F = -\partial E/\partial L$ to the Lifshitz force between two Si semispaces $F_{flat}(L)$ on the Fig. 3.

We can see that the larger corrugated region the stronger the force between the gratings. When the distance between the objects increases the difference in the forces vanishes.

IV. CONCLUSION

In our work, we developed the theoretical formalism which is suitable for arbitrary gratings with periodicity in two dimensions. The material of the grating can be defined by any dielectric permittivity function limited only by the rate of convergence.

Different periodical systems can be studied in the future using our method.

Acknowledgments

This research was supported in part by Saint Petersburg State University grant 11.38.237.2015. Research was carried out using computational resources provided by Resource Center "Computer Center of SPbU" (http://cc.spbu.ru/en).

---

[1] H. B. G. Casimir, *On the Attraction Between Two Perfectly Conducting Plates*, Proc. Kon. Ned. Akad. Wetensch. **51**, 793 (1948).

[2] I. Dzyaloshinskii, E. Lifshitz, and L. Pitaevskii, *The general theory of Van der Waals forces*, Advances in Physics **10**, 165 (1961).

[3] B. Derjaguin and I. Abrikossova, *Direct measurements of molecular attraction of solids*, Journal of Physics and Chemistry of Solids **5**, 1 (1958).

[4] S. Johnson, *Numerical methods for computing Casimir interactions*, in *Casimir Physics*, edited by D. Dalvit, P. Milonni, D. Roberts, and F. da Rosa (Springer-Verlag Berlin Heidelberg, 2011), Lecture Notes in Physics 834, chap. 6.

[5] A. Lambrecht and V. N. Marachevsky, *Casimir Interaction of Dielectric Gratings*, Phys. Rev. Lett. **101** (2008).

[6] O. M. Rayleigh, *On the dynamical theory of gratings*, Proc. Roy. Soc. A **79**, 399 (1907).

[7] H.-C. Chiu, G. L. Klimchitskaya, V. N. Marachevsky, V. M. Mostepanenko, and U. Mohideen, *Demonstration of the asymmetric lateral Casimir force between corrugated surfaces in the nonadditive regime*, Phys. Rev. B **80**, 14 (2009).

[8] V. Marachevsky and A. Nelson, *The Casimir force for 2d sinusoidal gratings*, EPJ Web of Conferences **125** (2016).

Towards exotic topological states in parralel semiconductor nanowires

Olivier Faist,[1] Christian Jünger,[1] Lucia Sorba,[2] Andreas Baumgartner,[1] and Christian Schönenberger[1]
[1]*Department of Physics, University of Basel, CH-4056, Basel, Switzerland*
[2]*NEST-INFM and Scuola Normale Superiore, Piazza dei Cavalieri 7, I-56126 Pisa, Italy*

Recent advances in semiconductor-nanowire device fabrication have resulted in the first tentative evidence for Majorana Fermions in solids. Our aim is to extend the family of such semiconductor-superconductor hybrid structures to devices with two parallel nanowires, which potentially might lead to fractional Majorana states (parafermions), which might be used as building blocks for topological quantum computing. We discuss the challenges in this project and the first steps towards this new device type.

I. INTRODUCTION

Semiconductor nanowires (NW) provide a flexible and reliable way of growing a conductor with low dimensionality at the nanoscale (defined as features being smaller than 100nm)[1]. Possible engineering of exotic topological states in these nanowires[2] has attracted a lot of interest, and recently the detection of signatures of Majorana Fermions[3] holds a lot of promise; schemes have been proposed to use them as a base for topological quantum computation (TQC).

TQC provides an elegant way around the problem of qubit decoherence, in that it offers a possibility of topologically protected error-free computations. Beyond Majorana fermions, fractional Majorana fermions, also called parafermions, promise an even wider array of possible gates for TPC. One way of engineering a parafermion is by coupling two nanowires to a common superconductor[4], notably requiring low critical fields (500 mT). Our over-arching goal is to fabricate such a device. We will first list and review the challenges we expect to face, present the state of our research, and then discuss the next steps we sill be focussing on.

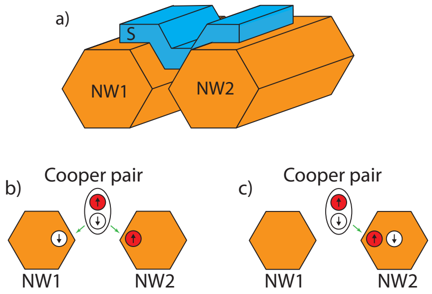

FIG. 1: **a)** Schematic of a double nanowire superconductor heterostructure. Two competing S-N transport processes are **b)** crossed Andreev pairing. **c)** direct Andreev pairing. Tunneling processes also contribute to transport.

II. INGREDIENTS FOR ENGINEERING PARAFERMIONS IN A DOUBLE NANOWIRE DEVICE

Theoretical work[4] predicts that should some conditions be met, one could possibly engineer those parafermion states, in a device resembling fig. 1 a). These conditions are:

1. **Parralel nanowires in close proximity.** NWs must be electrically isolated, but lie next to each other.
2. **Individual contacting** of these parrallel nanowires. This requires a precise (up to 20-30nm) fabrication cycle, from reading out wire postition to lithography of a structure around the nanowire pair.
3. **Pairing potential Δ dominated by crossed Andreev pairing**. Qualitatively, we want crossed Andreev pairing (fig. 1 b)) to dominate direct Andreev pairing (fig. 1 c)) and other tunneling effects.
4. **A floating superconducting island** over the wire pair, in order to induce a superconductive gap in the nanowire pair.
5. **Different spin-orbit interaction strength** in each nanowire. Spin-orbit coupling is naturally anisotropic in NWs, and we would need to individually characterize each wire.
6. **large B-field parallel to the NW pair.** This presents an issue, since the magnetic field may not exceed the critical field of the superconductor,

Once these conditions are met, such a device might exhibit traces of a parafermion particle, which could be measured in a cryogenic setup.

III. PRELIMINARY RESULTS

Preliminary work has focused on individually contacting nanowire pairs. For this, nanowires are deposed on

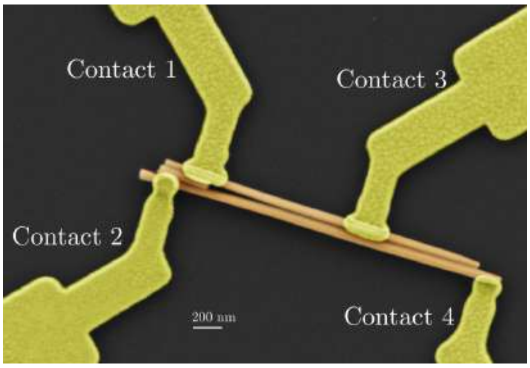

FIG. 2: SEM Image of a prototype device. Wire thickness is 40nm..

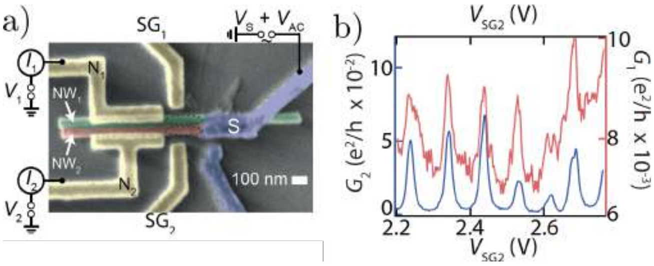

FIG. 3: State-of-the art double nanowire Cooper pair splitter. **a)** e-beam image of the fabricated device. **b)** Current correlations due to CPS: the current peaks in dot 1(red) when tuning quantum dot 2 show correlations due to cooper pair splitting[5].

a base structure (used to align succesive design steps) and then suitable randomly formed wire pairs are post-selected using scanning electron microscopy. From these images, wire positions are read out using a custom program, and structures are designed and lithographied. Such a device can be seen in fig. 2. We have achieved individual contacting, our effort is now concentrated on improving the fabrication yield.

As to requirement **3**, cooper pair splitting in a double nanowire device was shown in recent experiments[5] (fig. 3). Although the 20% cooper pair splitting efficiency achieved here is still far from carbon nanotube experiments[6], which can be near unity.

A superconductor island (requirement **4**), schematically shown in in blue in fig. 1, has to answer a compromise: It should be thin enough not to influence the magnetic field, but thick enough to be able to bridge and contact both wires. As to different Spin-orbit coupling for each wire (req. **5**) it has been shown that the g-tensor is randomly oriented in a nanowire[7], so it is reasonable to expect that the SOI is not identical in the two NWs.

IV. OUTLOOK

The main focus of current efforts is the reliable contacting of individual wires in a double wire configuration. Once that is mastered and reliably reproduced, our next goals will be the characterisation of spin-orbit interactions in individual wires and coupling the wires to a common superconductor.

Acknowledgments

This project is financially supported by QuantERA - SuperTop project, the NCCR QSIT, the SNF as well as the Swiss nanoscience institute (SNI).

---

[1] Y. Xia, P. Yang, Y. Sun, Y. Wu, B. Mayers, B. Gates, Y. Yin, F. Kim, and H. Yan, *One-dimensional nanostructures: Synthesis, characterization, and applications*, Advanced Materials **15**, 353 (2003).

[2] A. Y. Kitaev, *Unpaired majorana fermions in quantum wires*, Physics-Uspekhi **44**, 131 (2001).

[3] V. Mourik, K. Zuo, S. M. Frolov, S. R. Plissard, E. P. A. M. Bakkers, and L. P. Kouwenhoven, *Signatures of majorana fermions in hybrid superconductor-semiconductor nanowire devices*, Science **336**, 1003 (2012).

[4] J. Klinovaja and D. Loss, *Time-reversal invariant parafermions in interacting rashba nanowires*, Physical Review B **90**, 045118 (2014).

[5] S. Baba, C. Jünger, S. Matsuo, A. Baumgartner, Y. Sato, H. Kamata, K. Li, S. Jeppesen, L. Samuelson, H. Xu, et al., *Cooper-pair splitting in two parallel inas nanowires*, Arxiv **1802.08059** (2018).

[6] J. Schindele, A. Baumgartner, and C. Schönenberger, *Near-unity cooper pair splitting efficiency*, Phys. Rev. Lett. **109**, 157002 (2012).

[7] S. d'Hollosy, G. Fbin, and A. Baumgartner, *g-factor anisotropy in nanowire-based InAs quantum dots*, AIP Conference Proceedings **1566**, 359 (2013).

Towards molybdenum disulfide nanostructures with superconducting contacts

Mehdi Ramezani,[1] Kenji Watanabe, Takashi Taniguchi,[2] Christian Schönenberger,[1] and Andreas Baumgartner[1]
[1]Department of Physics, University of Basel, CH-4056, Basel, Switzerland
[2]National Institute for Materials Science, Namiki 1-1, Tsukuba, Ibaraki 305-0044, Japan

Electronic devices based on two dimensional semiconductors with superconducting contacts hold great promises for fundamental research, as well as for applications, for example to artificially generate topological states of matter, such as Majorana bound states. Here we focus on semiconducting van der Waals heterostructures, which allows to combine a large variety of active materials with different properties and contact materials. However, the fabrication of even the most basic devices is challenging on various levels. For instance, the electron mobility is typically low in these materials, and superconducting contacts have not been reported so far. Here we report on our very preliminary steps to fabricate superconducting edge contacts to hexagonal boron nitride (hBN) encapsulated molybdenum disulfide (MoS_2). The encapsulation of the active layer is performed in an inert gas atmosphere using a dry transfer method. The very preliminary electrical characterization shows a two-terminal resistance of 2.1 $M\Omega$ at zero backgate voltage, tunable to 1.4 $M\Omega$ at 1.5 V on the backgate.

I. INTRODUCTION

Semiconducting nanostructures combined with superconducting materials has been widely investigated to be utilized in quantum computing and study of physical phenomena[1]. Such system has attracted extensive attention during recent years mentoring nanowires with large spin-orbit interaction contacted via conventional superconductor. However, such system suffers from low fabrication yield, instability under ambient condition, limiting in device configuration, and scalability.

Layered transition metal dichalcogenides (TMDCs) are a class of materials that can be cleaved down to atomically thin layers, with distinct properties compared to their bulk counterpart[2]. Molybdenum disulfide is formed by hexagonal arrangement of metal atoms sandwiched by a strong covalent bond between chalcogenide atoms. The broken inversion symmetry in its crystallographic structure, lifts to the spin degeneracy at K and K' point in the first Brillouin zone. Encapsulation of molybdenum disulfide with hexagonal boron nitride (hBN) flakes tends to suppress scattering and enhances mobility[3]. The observed splitting of the valence band maximum around the high-symmetry point K in monolayer molybdenum disulfide is attributed to the spin orbit interaction (SOI)[4]. Presence of supercurrent in quantum hall regime will be mediated by edge states. Therefore, encapsulated molybdenum disulfide contacted with superconducting materials can potentially lead to phase coherent Andreev reflection at the interface of the junction. Intuitively, transparent superconducting contacts should be addressed to detect supercurrent in the system. Edge contact proved to enhance ohmic behavior in graphene-normal metal contacts[3] as well as graphene-superconductor junction. Yet, there is no solid report on edge contact to any other two-dimensional material. Here in this study, we are introducing the very first steps to fabricate edge contact of superconducting material to encapsulated molybdenium disulfide.

II. SAMPLE FABRICATION

Cleaving of crystaline molybdenite using the well known mechanical exfoliation method could lead to high quality two-dimensional crystals, with higher mobility. However, exfoliation methods tend to introduce residual contamination between the stacks, which leads to charge scattering. In order to minimize the material degradation, and residual contamination, all stacking steps are conducted in glove box (nitrogen 99.9999%) via a dry-transfer method. Figure 1(a) illustrates the schematic of molybdenum disulfide flake encapsulated within hBN crystals, and graphite back gate. The superconducting MoRe contacts are sputtered and then connected to pads by Ti/Au leads. The thickness of the flakes are identified using its contrast under optical microscope. The contacts are patterned using electron beam lithography step, followed by a low temperature developing step. The contacts are etched utilizing a reactive ion etching (RIE; CHF_3 and O_2) system. Figure 1(b) displays the optical micrograph of the device were molybdenum disulfide is contacted to molybdenum rhenium via edge contact.

III. RESULTS AND ANALYSIS

In order to characterize this device we will discuss first characterizations of this type of contacts. The two-terminal measurements using a conventional lock-in technique is performed at room temperature. Fig 2 shows the characteristics of two adjacent contact separated by 300 nm. These data show gate-tunable zero-bias response of a junction, with resistance 2.1 $M\Omega$ at zero gate voltage, and 1.4 $M\Omega$ at 1.5 V.

The large resistance could be attributed to a thermally activated tunneling through a large Schottky barrier, which leads to high contact resistance at low temperature. Since we have not investigate low temperature characteristics of this device, it is hard to have a solid conclusion about the origin of the contact resistance.

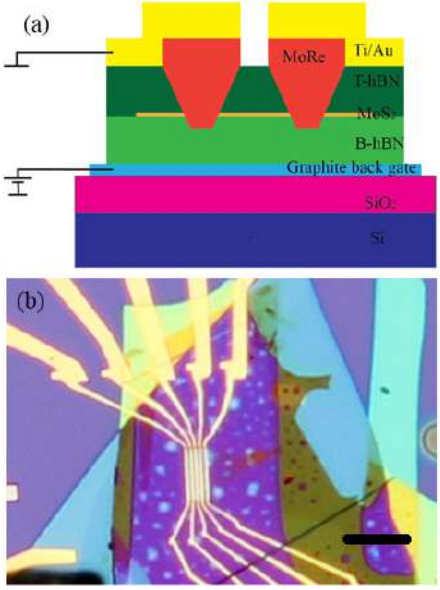

FIG. 1: (a) Schematic of the encapsulated molybdenum disulfide with superconducting edge contacts. (b) Optical microscopy of the encapsulated molybdenum disulfide. The scale bar is 5 μm.

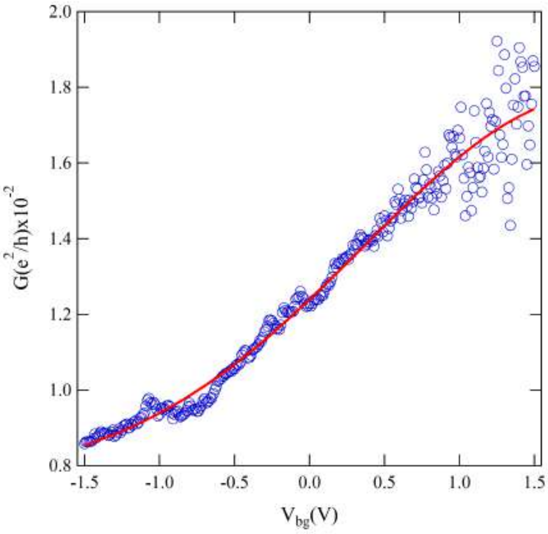

FIG. 2: Two terminal conductance of encapsulated molybdenum disulfide in respect to different gate voltages, and the corresponding fit (red solid line).

IV. CONCLUSIONS AND OUTLOOK

In conclusions, we demonstrated a method to fabricate potentially superconducting edge contact to monolayer molybdenum disulfide. The room temperature measurements shows gate-tunable conductance, which is consistent for all four junctions in the same device. Intuitively, the whole processing could lead to more complex designs which can satisfy the requirements of more complex measurements. The low temperature measurements at cryogenic temperature could reveal the origin of resistance, type of contact, and many physical phenomena in the system.

Acknowledgments

We would like to thank Swiss nanoscience institute (SNI) for the financial support.

---

[1] M. Leijnse and K. Flensberg, *Introduction to topological superconductivity and majorana fermions*, Semiconductor Science and Technology **27**, 124003 (2012).

[2] A. Splendiani, L. Sun, Y. Zhang, T. Li, J. Kim, C.-Y. Chim, G. Galli, and F. Wang, *Emerging photoluminescence in monolayer mos2*, Nano letters **10**, 1271 (2010).

[3] L. Wang, I. Meric, P. Huang, Q. Gao, Y. Gao, H. Tran, T. Taniguchi, K. Watanabe, L. Campos, D. Muller, et al., *One-dimensional electrical contact to a two-dimensional material*, Science **342**, 614 (2013).

[4] Z. Zhu, Y. Cheng, and U. Schwingenschlögl, *Giant spin-orbit-induced spin splitting in two-dimensional transition-metal dichalcogenide semiconductors*, Physical Review B **84**, 153402 (2011).

Towards non-destructive, real-time transport measurements of interacting Fermi Gas

Victor Helson,[1] Barbara Cilenti,[1] Kevin Roux,[1] Hideki Konishi,[1] and Jean-Philippe Brantut[1]

[1] *Institute of Physics, École Polytechnique Fédérale de Lausanne, CH-1015, Lausanne, Switzerland*

In recent years, it has become possible to investigate transport phenomena using ultracold atoms in a variety of geometrical configurations, e.g. with two reservoirs connected through a mesoscopic channel[1]. The measurements, however, rely on comparing different samples because of the destructive nature of probing methods, which makes them sensitive to even very weak fluctuations in the atomic sample preparation. In order to achieve more precise measurements, we will implement non-destructive measurements of the atomic current featuring cavity QED techniques[2]. We are currently developing a new apparatus where a degenerate Fermi gas of ^{6}Li will be coupled to a high-finesse optical cavity. In this abstract, we will discuss the non-destructive probing scheme using the high-finesse cavity and present the recent progress on the experimental apparatus.

I. INTRODUCTION

Technical progress made in the field of ultracold atoms over the past decades has opened the way to the study of transport phenomena in strongly interacting clouds of degenerate Fermi gases. While transport processes typically occur for electrical charges within a material, and give rise to the material's electronic applications, numerically simulating such systems has been proven difficult because of their non-equilibrium nature[3]. However, with the possibilities offered by the use of optical trapping to both cool down and shape atomic clouds, along with the use of tunable short-range interactions, ultracold atoms can actually be used as a platform for simulating many condensed matter phenomena, including transport.

Experiments in this field have already been realized and configurations such as the Landauer setup[4] and a quantum point contact[5] have been achieved with the use of ultracold ^{6}Li atoms. However the measurement method used in previous experiments relied on comparing different samples due to its inherent destructive nature, which made the results very sensitive to fluctuations in the atomic sample preparation *e.g.* to the number of atoms. In order to circumvent this limitation, we are building a new experimental setup which will feature a non-destructive way of monitoring the atomic flow in a single realization of the experiment, granting us insight about the dynamics of the atomic cloud[6]. A high finesse Fabry-Pérot cavity, within which the atomic samples are prepared, will enable these non-destructive measruements through continuous monitoring of the cavity field with a enhanced signal-to-noise ratio.

In this abstract, we will present an overview of the non-destructive measurement technique along with the experimental appartus currently being set up.

II. NON DESTRUCTIVE MEASUREMENTS

The continuous and non destructive measurement of atomic currents on single realizations of a cold atomic gas is a staple feature of the new experimental setup. The concept is presented in figure 1: it relies on (i) the two (or multi-)terminal Landauer configuration, where the system of interest is connected to large atomic reservoirs allowing to inject and collect particles, and (ii) the use of continuous measurements of atom numbers using a high finesse cavity and a probe laser far from the atomic resonance. The atomic current consists in atoms continuously entering and leaving the reservoir, thereby entering the mode of the cavity and leading to a phase shift of the probe laser, which is measured by a quantum limited interferometer.

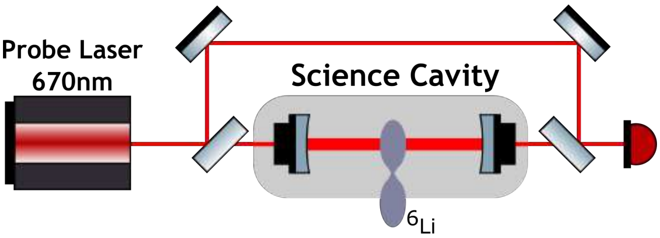

FIG. 1: A simple homodyne detection scheme allowing to measure the dispersive phase shift of a probe laser beam induced by an atomic cloud inside of an optical cavity. Using a probe beam resonant with the cavity allows to increase the signal-to-noise ratio of the measurement.

The high finesse cavity ensures that the phase shift and measurement back-action stands out of the trivial effects of spontaneous emission[7], yielding a enchanced signal-to-noise ratio at a fixed destructivity of the atomic sample[8].

III. EXPERIMENTAL APPARATUS

The experimental setup consists of an ultra-high vacuum chamber within which a thermal gas of ^{6}Li atoms is produced in an oven to be successively trapped and cooled up to the quantum degeneracy inside a high-finesse optical cavity. The core of the setup is shown by figure 2, which displays, from left to right:

- An oven containing solid ^{6}Li chunks, which produce a thermal gas when heated up.
- A Zeeman slower acting as a first cooling stage.

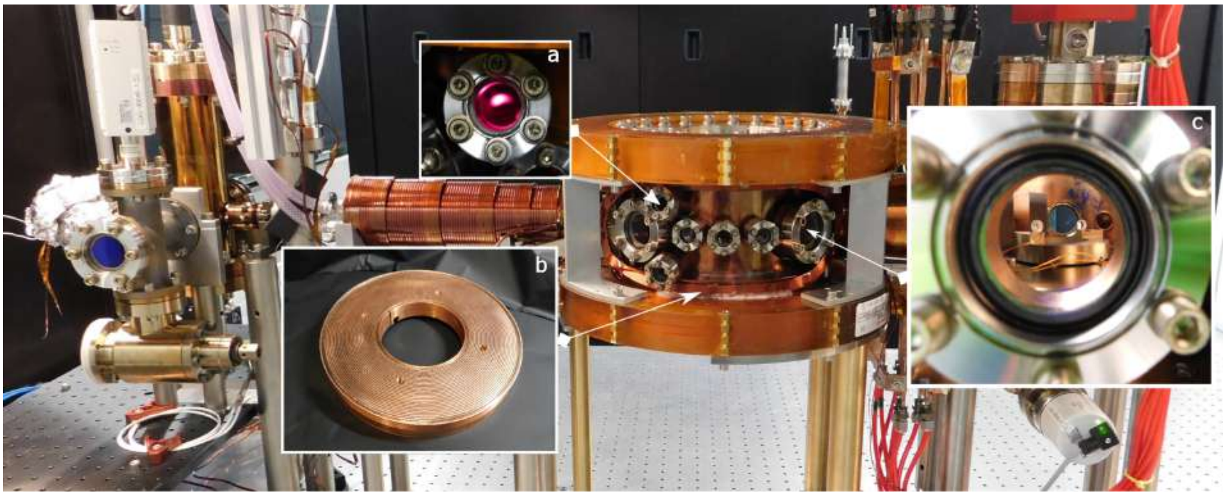

FIG. 2: Picture of the experimental setup being built. The thermal ^{6}Li gas is produced in an oven – the aluminum foiled part on the left – then slowed down as it progresses down the Zeeman slower – the tube at the center of the picture – to end up being trapped in the main science chamber. **a.** A fluorescent cloud of ^{6}Li atoms trapped in a magneto-optical trap inside the chamber. **b.** One of the coils designed to scan the scattering length of the atoms near a Feshbach resonance. **c.** The optical cavity inside the chamber, resting on its vibration dampening stack.

Atoms going through the tube experience a spatially varying Zeeman shift which enables a counter-propagating laser beam to remain resonant with them as they continuously get slowed down thanks to laser Doppler cooling.

- The main science chamber which contains a high-finesse optical cavity – $F = 50000$ at 670nm – to trap, cool down and probe the atomic cloud. The cavity rests on a vibration dampening stage which acts as a low-pass filter for mechanical vibrations.

At the moment, we are able to confine the atoms in a magneto-optical trap at the center of the cavity. While further tuning of the trapping parameters remains to be done, we retrieve around 10^8 laser cooled atoms.

The next step, currently being implemented, is evaporative cooling with the use of a dipole trap created by a 1064nm laser resonantly shined onto the cavity. The intra-cavity power and therefore the trapping depth are enchanced by a factor proportionnal to the finesse of the cavity[9] – $F = 3000$ at 1064nm – which allows to produce a trap with a depth of a few mK with only 100mW of laser power.

---

[1] S. Krinner, T. Esslinger, and J.-P. Brantut, *Two-terminal transport measurements with cold atoms*, Journal of Physics: Condensed Matter **29**, 343003 (2017).

[2] S. Uchino, M. Ueda, and J.-P. Brantut, *Universal Noise and Heating in Continuous Measurements of Interacting Fermions*, ArXiv e-prints (2018).

[3] I. Bloch, J. Dalibard, and W. Zwerger, *Many-body physics with ultracold gases*, Rev. Mod. Phys. **80**, 885 (2008).

[4] J.-P. Brantut, J. Meineke, D. Stadler, S. Krinner, and T. Esslinger, *Conduction of ultracold fermions through a mesoscopic channel*, Science **337**, 1069 (2012).

[5] D. Husmann, S. Uchino, S. Krinner, M. Lebrat, T. Giamarchi, T. Esslinger, and J.-P. Brantut, *Connecting strongly correlated superfluids by a quantum point contact*, Science **350**, 1498 (2015).

[6] C. Laflamme, D. Yang, and P. Zoller, *Continuous measurement of an atomic current*, Phys. Rev. A **95**, 043843 (2017).

[7] Z. Chen, J. G. Bohnet, J. M. Weiner, K. C. Cox, and J. K. Thompson, *Cavity-aided nondemolition measurements for atom counting and spin squeezing*, Phys. Rev. A **89**, 043837 (2014), URL `https://link.aps.org/doi/10.1103/PhysRevA.89.043837`.

[8] J. E. Lye, J. J. Hope, and J. D. Close, *Nondestructive dynamic detectors for Bose-Einstein condensates*, Phys. Rev. A **67**, 043609 (2003).

[9] H. Tanji-Suzuki, I. D. Leroux, M. H. Schleier-Smith, M. Cetina, A. T. Grier, J. Simon, and V. Vuletić, *Interaction between Atomic Ensembles and Optical Resonators*, Advances in Atomic Molecular and Optical Physics **60**, 201 (2011).

Transport of Ultracold Fermions through Tunable Low-Dimensional Structures

Jeffrey Mohan,[1] Samuel Häusler,[1] Laura Corman,[1] Martin Lebrat,[1] Philipp Fabritius,[1] and Tilman Esslinger[1]
[1]*Institute of Quantum Electronics, ETH Zürich, 8093 Zürich, Switzerland*

We describe our experiment for studying transport of neutral Fermions through one- and two-dimensional structures using magneto-optically confined lithium-6. We show how we use a digital micromirror device as a spatial light modulator to generate additional arbitrary potential landscapes and outline here some recent improvements to our generation method. This system allows us to apply the full toolbox of ultracold atomic gas quantum simulators to address open questions in transport properties of quantum phases of matter.

I. INTRODUCTION

Among the many technological and scientific advances brought about by the second quantum revolution are ultracold atomic gas quantum simulators[1]. The key advantage of using these systems for studying their solid-state analogues is the experimental control the atoms' internal degrees of freedom afford. Using their electronic and hyperfine structure and Feshbach resonances, modern experiments employ a combination of optical and magnetic traps to cool and confine clouds of $10^5 - 10^6$ atoms to temperatures in the tens of nanokelvins regime with interatomic interactions that can be tuned from strongly attractive to strongly repulsive to non-interacting.

This same internal structure furthermore allows us to locally probe and manipulate the cloud. With near-resonant light, the density distribution of the cloud can be directly measured using absorption imaging, and with far-off-resonant light, we can produce a conservative potential directly proportional to the laser intensity $V(\mathbf{r}) \propto I(\mathbf{r})$ that is either attractive or repulsive depending on the sign of the detuning[2]. By integrating a microscope objective, the imaging resolution and feature sizes of the projected potentials can be shrunk to address characteristic length scales of the atoms like the Fermi wavelength.

In our experiment, we use these tools to build atomtronic counterparts of fundamental electronic devices such as the two-dimensional electron gas (2DEG) and the quantum point contact (QPC). The "device", shown in orange in Figure 1a, begins as a cloud of Fermionic lithium-6 atoms that is magneto-optically confined into a three-dimensional cigar shape. The dimensionality at the center is reduced to either 2D or 1D by shining 1 or 2 repulsive TEM_{01}-like beams that confine the atoms into the constriction shown in Panel b. With additional beams not shown, we can create temperature and chemical potential imbalances between the two reservoirs and observe the relaxation dynamics as they exchange particles and heat through the QPC by directly measuring the density in each region. This system naturally forms a two-terminal device and has been confirmed to reside in the 1D regime through observation of the hallmark quantization of particle conductance in a system of non-interacting Fermions[3].

The promise of cold gas quantum simulators, however, is to go beyond what is experimentally or theoretically achievable in solid state systems. To this end, we employ a spatial light modulator (SLM) to engineer scattering structures within the QPC with more flexibility than metallic gates or AFM tips can achieve in solid state devices. The digital micromirror device (DMD) we use as an SLM is depicted in Figure 1a shaping the beam that forms a 1D lattice on the atoms when focused through the microscope in Figure 1b.

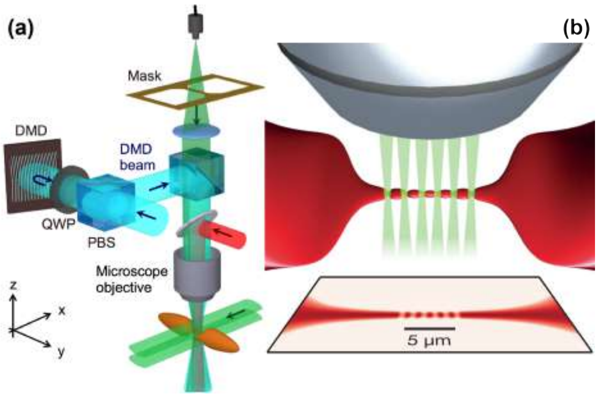

FIG. 1: The optical system used to define the atomtronic device[4,5]. The 3D reservoirs (orange lobes in **(a)**) are coupled via a 1D channel (blown up in **(b)**) onto which the beam shaped by the DMD (green) is projected to form the desired potential landscape.

II. POTENTIAL ENGINEERING WITH A DIGITAL MICROMIRROR DEVICE

A DMD is simply an array of $\sim 1000 \times 1000$ micron-scale mirrors that can be individually flipped into either an on or off state where light is reflected with near-unit and near-vanishing reflectivity respectively. We can therefore imprint holograms with $\sim 10^6$ binary degrees of freedom modifying only the amplitude of the beam impinging on the DMD, a typical example of which is shown in Figure 1a. Given the state of each mirror and complete knowledge of the linear optical system between the DMD and the atoms, we can therefore calculate the potential felt by the atoms that is produced by the hologram. We however want to solve the reverse problem: What is the hologram the DMD must imprint on a field such that it forms the desired potential in the atomic plane? The difficulty of this problem is two-fold: Firstly, how do we map a generic amplitude and phase hologram to a binary state of the DMD? Secondly, propagating a field from the atomic plane to the DMD plane requires both amplitude and phase information, but specifying a potential $V(\mathbf{r})$

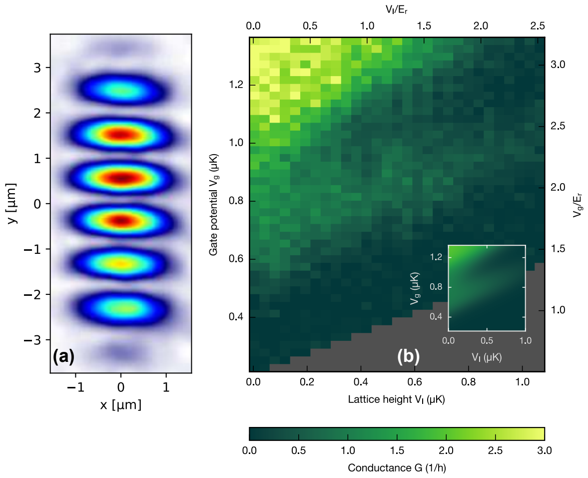

FIG. 2: **(a)** An experimental lattice potential produced by the DMD and **(b)** the effect of the lattice on the transport properties of a non-interacting Fermi gas in a QPC[5]. The inset is a fit-free theoretical prediction.

fixes only the amplitude and not the phase.

The solution to these two problems developed by Zupancic *et al.*[6] has been successfully applied in our experiment to produce a number of novel results. In one application, the DMD was used to produce a finite lattice on the QPC whose resulting band gap could be clearly observed[5]. The lattice as well as evidence of this gap is shown in Figure 2. Panel b shows the particle conductance of a non-interacting Fermi gas through the lattice as a function of its height and the chemical potential in the QPC. According to the Landauer-Büttiker formula, the region of suppressed conductivity near $V_g = 1.1\ \mu$K that widens with increasing lattice strength indicates a decrease in transmission and therefore in the density of states *i.e.* a band gap.

III. HOLOGRAM IMPROVEMENT AND FUTURE WORK

The lattice achieved with the current hologram generation method is, however, not identical to the target potential (6 evenly spaced sites of equal height). While this does not qualitatively change the effects of the lattice, it does smear out the band gap and make the observed signal less clear. For this reason and to improve the low efficiency with which this method uses laser power, which has so far been an experimental bottleneck, we have implement and adapted to the DMD another solution[7] that relaxes a number of constraints of the previous one. With this method, we release control over the field's amplitude and phase in regions of the atomic plane where atoms do not explore *i.e.* outside the QPC. This deconstrains the problem to achieve higher fidelity in the controlled region and a ten-fold increase in efficiency. The improvement of this method is demonstrated by the experimental images in Figure 3.

With this new method of generating optical potentials, we will study transport of the gas through structures predicted to have a topological character, such as lattices with a flat band where interactions dominate and the density of states is enhanced[8].

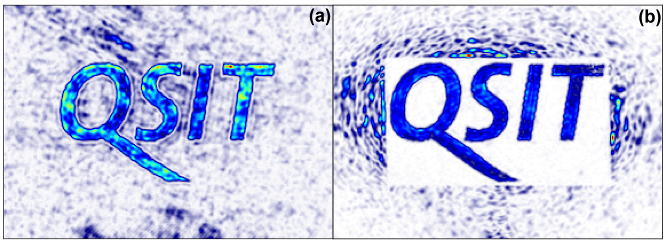

FIG. 3: The QSIT logo generated with the old **(a)** and new **(b)** method demonstrating the increased conformity in the control region at the expense of freedom outside.

Acknowledgments

We thank current and former members of the Quantum Optics group for their prior work on this project and acknowledge financial support from NCCR QSIT, Swiss NSF, and ERC.

---

[1] I. Bloch, J. Dalibard, and S. Nascimbène, *Quantum simulations with ultracold quantum gases*, Nature Physics **8**, 267 (2012).

[2] R. Grimm, M. Weidemüller, and Y. B. Ovchinnikov, *Optical Dipole Traps for Neutral Atoms* (Academic Press, 2000).

[3] S. Krinner, D. Stadler, D. Husmann, J.-P. Brantut, and T. Esslinger, *Observation of quantized conductance in neutral matter*, Nature **517**, 64 (2014).

[4] S. Häusler, S. Nakajima, M. Lebrat, D. Husmann, S. Krinner, T. Esslinger, and J.-P. Brantut, *Scanning Gate Microscope for Cold Atomic Gases*, Phys. Rev. Lett. **119**, 030403 (2017).

[5] M. Lebrat, P. Grišins, D. Husmann, S. Häusler, L. Corman, T. Giamarchi, J.-P. Brantut, and T. Esslinger, *Band and Correlated Insulators of Cold Fermions in a Mesoscopic Lattice*, Phys. Rev. X **8**, 011053 (2018).

[6] P. Zupancic, P. M. Preiss, R. Ma, A. Lukin, M. E. Tai, M. Rispoli, R. Islam, and M. Greiner, *Ultra-precise holographic beam shaping for microscopic quantum control*, Opt. Express, OE **24**, 13881 (2016).

[7] A. L. Gaunt and Z. Hadzibabic, *Robust Digital Holography For Ultracold Atom Trapping*, Scientific Reports **2**, 721 (2012).

[8] S. Peotta and P. Törmä, *Superfluidity in topologically nontrivial flat bands*, Nature Communications **6**, 8944 (2015).

Weak coupling of a charge-tunable quantum dot to a tunable microcavity

Natasha Tomm,[1] Daniel Najer,[1] Benjamin Petrak,[1] and Richard J. Warburton[1]

[1]*Department of Physics, Nanophotonics Group, University of Basel, CH-4056, Basel, Switzerland*

Optical microcavities enhance light-matter interaction and photon confinement, allowing one to study rich single quantum emitter physics, called cavity quantum electrodynamics (cQED). Making use of the appropriate tuning of the microcavity properties, one can entangle single-emitter and cavity states (strong coupling) or enhance spontaneous emission (weak coupling). By weakly coupling zero-dimensional semiconductor structures (quantum dots - QDs) to a microcavity mode, the goal is to construct a single-photon source presenting high *purity*, high *brightness* and high *indistinguishability*. These are key characteristics for quantum information technologies.

I. INTRODUCTION

Optical quantum technologies require on-demand production of single-photons[1], with high *purity*, high *brightness* and high *indistinguishability*[2,3]. State-of-the-art single-photon sources involve heralded photons techniques, such as parametric downconversion (not on-demand) or semiconductor nanostructures in photonic structures[4]. The later is highly attractive, offering easy integration and scalability.

Semiconductor quantum dots (QDs) have discrete energy levels, similar to the electronic states in a single atom. At low temperature, there is an almost 100% probability that a resonant excitation pulse will result in the emission of a single photon. However, the high-index semiconductor environment in which the QDs are embedded limits the escape of this photon, resulting in less than 5% of photons usually emerging from the device[5].

A solution to such a low collection rate is to embed the QD in an optical microcavity, which is able to confine light to small volumes by resonant recirculation[6]. As predicted by E.M. Purcell in 1946, one can enhance spontaneous emission making use of a resonant cavity[7]. The aim of this project is to achieve in practice a high brightness single-photon source, by fine-tuning the spectral and spatial properties of a self-fabricated microcavity. Through effective coupling of cavity mode to the QD, we will be able to achieve Purcell emission enhancement, and produce a high quality single-photon source.

II. THEORETICAL BACKGROUND

Spontaneous emission is interpreted in quantum theory as a stimulated emission process driven by fluctuations in the *vacuum field*[4]. The ground state of an empty optical cavity has a randomly fluctuating electric field with amplitude E_{vac}, which is inversely proportional to the mode volume V with a certain photon density of states $\rho_{vac}(\omega, V)$. According to the *Fermi's golden rule* the spontaneous emission rate is proportional to the photon density of states, and given by

$$W = \frac{2\pi}{\hbar^2}|M|^2\rho(\omega, V), \tag{1}$$

where M is a transition matrix element describing the electric dipole interaction.

Coupling the emitter resonantly to a single cavity mode leads to a modification of photon density of states, due to the mode volume confinement. The ratio of spontaneous emission rate inside a cavity to the free-space spontaneous emission rate is called the *Purcell factor*, and at resonance is described by

$$F_p = \frac{3}{4\pi^2}\left(\frac{\lambda}{n}\right)^3 \frac{Q}{V}, \tag{2}$$

where λ is the wavelength of emission, n is the refractive index of the material, and Q is the quality factor of the optical cavity, describing the photon loss rate per round-trip.

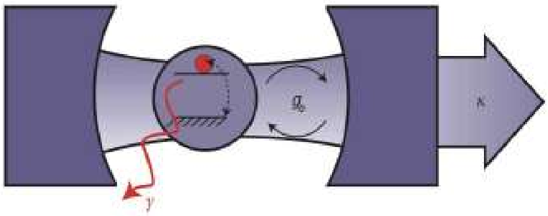

FIG. 1: Schematic of a two-level emitter coupled to a cavity by a coupling rate g_0. κ is the cavity's photon loss rate and $\propto \frac{1}{Q}$, and γ is the emitter's non-resonant decay rate, that broadens the emission linewidth.

From Equation 2 is clear that by confining the optical mode to a small volume inside the cavity the Purcell factor is increased, and a higher rate of photons is generated. Also according to Equation 2, the Q-factor of the cavity plays an important role, determining the cavity's photon loss rate κ. Given the intrinsic emitter's non-resonant decay rate γ, the condition for the weak-coupling regime is that $4g_0 < |\kappa - \gamma|$, where the highest quantum outcoupling efficiency is achieved when $2g_0 = \kappa$.

III. EXPERIMENTAL SETUP

In our experiments, a gated heterostructure with embedded self-assembled InAs QDs is grown on top of a

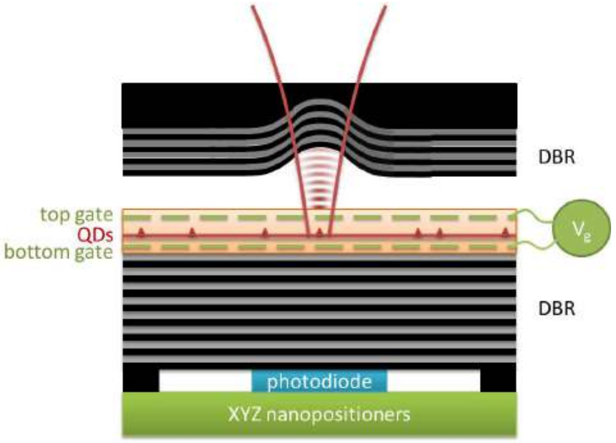

FIG. 2: Scheme of experimental setup: QD embedded in heterostructure, placed on top a xyz nanopositioner, with which the alignment of the sample relative to the top DBR is realized.

high reflectivity ($R > 99.98\%$) semiconductor distributed Bragg reflector (DBR), composed of alternating layers of GaAs and AlAs. The cavity is completed by a top dielectric DBR constructed on a concave mirror template of very small radius ($5\mu m < r < 20\mu m$)[8]. The sample is placed on xyz nanopositioners, in order to be able to fully tune the location and shape of the excitation beam relative to the QD[9,10], as seen in Fig. 2.

This experimental setup allows us to move the sample laterally relative to the top mirror, coupling an input Gaussian beam to the QD, and more importantly, we are able to in-situ tune the length of the cavity z, selecting the cavity frequency to anti-node position. With the appropriate combination of high-transmission/low-loss top mirror and a high reflectivity bottom mirror, efficient values of Q-factor and mode volume are expected.

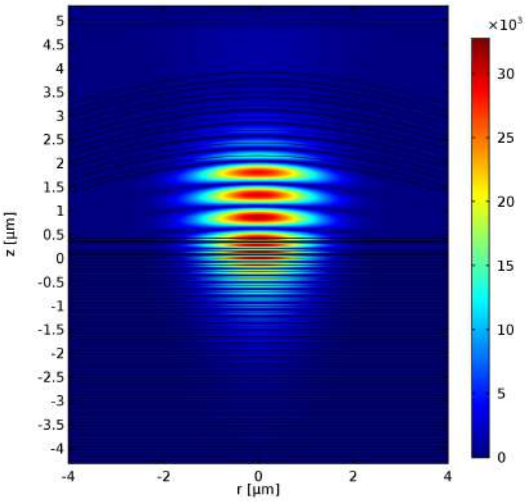

FIG. 3: Simulated cavity mode $|E_{vac}|^2$. Parameters: $\lambda = 919nm$, number of top mirror pairs = 7, number of bottom mirror pairs = 46.

According to simulations (see Fig. 3) the expected Q-factor for a configuration with a bottom DBR with 46 layers and a top mirror with 7 layers is of about 10 thousand. With this setup, the expectation to maximize the efficiency of out-coupling, reaching quantum efficiency of even 90% and a Purcell enhancement in the order of 9, configuring a high brightness and high purity single-photon source in the weak coupling regime.

---

[1] R. Warburton, *Single spins in self-assembled quantum dots*, Nature Materials **12**, 483 (2013).

[2] N. Somaschi, V. Giesz, L. De Santis, J. Loredo, M. Almeida, G. Hornecker, S. Portalupi, T. Grange, C. Anton, J. Demory, et al., *Near-optimal single-photon sources in the solid state*, Nature Phot. **10**, 340 (2016).

[3] A. Kuhlmann, J. Houel, A. Ludwig, L. Greuter, D. Reuter, A. Wieck, M. Poggio, and R. Warburton, *Charge noise and spin noise in a semiconductor quantum device*, Nature Physics **9**, 570 (2013).

[4] M. Fox, *Quantum Optics: An Introduction* (Oxford: Oxford University Press, 2006), 6th ed.

[5] P. Senellart, V. Giesz, and L. Lanco, *Ultrabright single-photon sources*, Photoniques Special EOS Issue p. 23 (2017).

[6] K. Vahala, *Optical microcavities*, Nature **424**, 839 (2003).

[7] E. Purcell, *Spontaneous emission probabilities at radio frequencies*, Phys. Rev. **69**, 681 (1946).

[8] D. Najer, M. Renggli, D. Riedel, S. Starosielec, and R. Warburton, *Fabrication of mirror templates in silica with micron-sized radii of curvature*, Appl. Phys. Lett. **110**, 011101 (2017).

[9] L. Greuter, S. Starosielec, A. Kuhlmann, and R. Warburton, *Towards high-cooperativity strong coupling of a quantum dot in a tunable microcavity*, Physical Review B **92**, 45302 (2015).

[10] L. Greuter, S. Starosielec, D. Najer, A. Ludwig, L. Duempelmann, D. Rohner, and R. Warburton, *A small mode volume tunable microcavity: Development and characterization*, Appl. Phys. Lett. **105**, 121105 (2014).

Optical control of NFAD detector using bright light

Gaëtan Gras,[1,2] Anqi Huang,[3,4] Vadim Makarov,[5,6] Hugo Zbinden,[2] and Félix Bussières[1,2]
[1]*ID Quantique SA, CH-1227 Carouge, Switzerland*
[2]*Group of Applied Physics, University of Geneva, CH-1211 Geneva, Switzerland*
[3]*Institute for Quantum Computing, University of Waterloo, Waterloo, ON, N2L 3G1 Canada*
[4]*Department of Electrical and Computer Engineering, University of Waterloo, Waterloo, ON, N2L 3G1 Canada*
[5]*Russian Quantum Center and MISIS University, Moscow*
[6]*Department of Physics and Astronomy, University of Waterloo, Waterloo, ON, N2L 3G1 Canada*

We study the vulnerability of a negative feedback avalanche diode (NFAD) detector to the blinding attack. Such an attack could threaten the security of quantum key distribution (QKD) systems. As potential countermeasure, we tested the monitoring of the current implemented in the ID220 from ID Quantique to detect the attack.

I. INTRODUCTION

Since its first inception[1], quantum key distribution (QKD) has attracted a lot of interest. The underlying principle of QKD allows two parties, Alice and Bob to share securely a secret key without making assumptions on the computational power of an eavesdropper Eve. However, practical systems can suffer from imperfections compared to models opening loopholes which can be used by Eve to get all or part of the secret key without being detected. Various types of attack have been proposed such as photon number splitting (PNS) attack[2], detector efficiency mismatch attack[3]. Here, we will be interested in the blinding attack also called faked state attack. In this attack, Eve uses bright light to take control of Bob's detectors and forced him to measure the outcome of her choice. This way, she can can reproduce the outcome of her measurement in Bob's setup introducing no error. Such an optical control of detectors have been demonstrated for single photon avalanche diodes (SPADs)[4–8] and for superconducting nanowire single photon detectors (SNSPDs)[9,10]. Here, we work on negative feedback avalanche diode (NFAD) detector.

II. BLINDING ATTACK

Under normal conditions, the detector works in Geiger mode, i.e., the diode is polarized with a voltage V_{bias} greater than the breakdown voltage. When a photon reached the detector, it creates an avalanche generating an electrical pulse. To generate the secret key, this analog signal is converted into a digital signal by using a comparator with a threshold voltage V_{th}. In order to take control of the detector, Eve sends continuous bright light onto the diode. By doing this, she generates a current through the diode to reduce the voltage across it. If Eve sends enough light she can then reduce the voltage across the diode below the breakdown voltage and put the detector into the linear mode. In this mode, the detector is no longer sensitive to single photons but instead works as a linear detector. Eve can then superimpose optical pulses to her blinding laser to generate controlled faked detections which we will call forced detections.

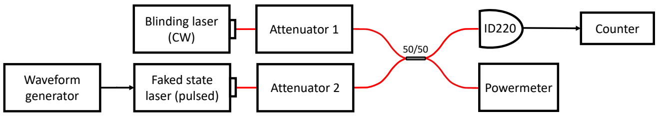

FIG. 1: Experimental setup used for the characterization of the blinding of the photodetector.

The setup of our experiment is shown in Fig. 1. Similar setup were used in previous experiments[4–6]. For the attack, we used 2 lasers at 1550nm powered by a waveform generator. The first laser (blinding laser) is working in continuous wave mode to make the detector enter its linear mode and hence become insensitive to single photons. The second laser is generating optical pulses of 33 ps full width half maximum (FWHM) at a variable rate controlled with the waveform generator. These pulses are generating the forced detections. We placed an optical attenuator after the pulsed laser in order to vary the energy of each pulse. The 2 laser signals are then combined by a beam splitter with a ratio 50/50. One arm is connected to a powermeter. The other arm is connected to the device. A counter is also used to measure the rate of forced detections.

III. EXPERIMENTAL RESULTS

Fig. 2 shows the probability to get a detection depending on the energy of the triggering pulse for various blinding power. For this experiment, we sent pulses at a rate of 40 kHz so none of them would hit the detector while it is in its deadtime. As we can see, there is a transition region where the detection probability is non-zero but less than one. As we increase the blinding power, this transition region becomes narrower up to a certain point. For low blinding power, this transition is too wide for an eavesdropper to perfectly control Bob's detectors in a BB84 protocol[5]. Eve has then two possibilities : either increase the blinding power to have a transition region sufficiently narrow (factor less than 2 between probabilities 0 and 1) or send pulse with a click probability less than 1 and adjust her output rate[11].

As the blinding requires to generate a continuous current in the detector, a possible way to detect the attack is to monitor the mean current flowing through the diode. As we can see on Fig. 3, when the detector is blinded i.e. when the count rate reaches 0, the current increases to several μA. In a normal use of the detector for QKD, one would prefer to work in the region before the saturation where the current is of the order of 100 nA. By setting the current threshold at the right value, we can then unambiguously detect the blinding of the detector.

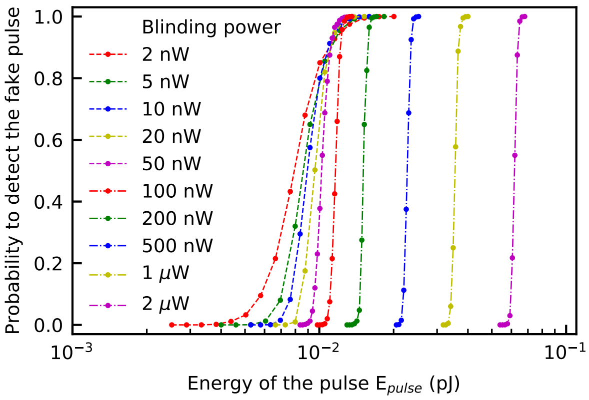

FIG. 2: Probability to generate a faked detection as a function of the pulse energy for a detector ID220 single mode with 10% photon counting efficiency set.

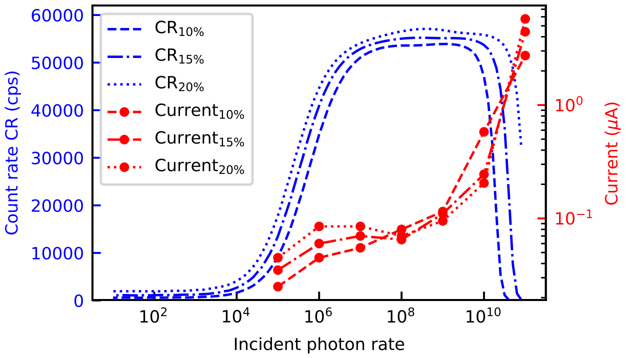

FIG. 3: Evolution of the detector count rate and bias current as a function of the incident photon rate.

IV. CONCLUSION AND OUTLOOK

We showed that by using bright light, we are able to take control of a NFAD single photon detector. This could potentially threaten the security of QKD systems if no proper countermeasure is implemented. Here, we showed that by monitoring the current flowing through the diode, we can unambiguously detect the attack. Further works will include improvements of the countermeasures against more sophisticated attacks and test of the efficiency of the attack against QKD protocols.

Acknowledgments

This project has received funding from the European Unions Horizon 2020 research and innovation programme under the Marie Skodowska-Curie grant agreement № 675662, NSERC of Canada (programs Discovery and CryptoWorks21), CFI, and MRIS of Ontario. A.H. was supported by China Scholarship Council.

[1] C. H. Bennett and G. Brassard, in *Proc. IEEE International Conference on Computers, Systems, and Signal Processing (Bangalore, India)* (IEEE Press, New York, 1984), pp. 175–179.

[2] B. Huttner, N. Imoto, N. Gisin, and T. Mor, *Quantum cryptography with coherent states*, Phys. Rev. A **51**, 1863 (1995).

[3] V. Makarov, A. Anisimov, and J. Skaar, *Effects of detector efficiency mismatch on security of quantum cryptosystems*, Phys. Rev. A **74**, 022313 (2006), erratum ibid. **78**, 019905 (2008).

[4] S. Sauge, L. Lydersen, A. Anisimov, J. Skaar, and V. Makarov, *Controlling an actively-quenched single photon detector with bright light*, Opt. Express **19**, 23590 (2011).

[5] V. Makarov, *Controlling passively quenched single photon detectors by bright light*, New J. Phys. **11**, 065003 (2009).

[6] L. Lydersen, C. Wiechers, C. Wittmann, D. Elser, J. Skaar, and V. Makarov, *Hacking commercial quantum cryptography systems by tailored bright illumination*, Nat. Photonics **4**, 686 (2010).

[7] L. Lydersen, J. Skaar, and V. Makarov, *Tailored bright illumination attack on distributed-phase-reference protocols*, J. Mod. Opt. **58**, 680 (2011).

[8] I. Gerhardt, Q. Liu, A. Lamas-Linares, J. Skaar, C. Kurtsiefer, and V. Makarov, *Full-field implementation of a perfect eavesdropper on a quantum cryptography system*, Nat. Commun. **2**, 349 (2011).

[9] M. Fujiwara, T. Honjo, K. Shimizu, K. Tamaki, and M. Sasaki, *Characteristics of superconducting single photon detector in dps-qkd system under bright illumination blinding attack*, Opt. Express **21**, 6304 (2013).

[10] M. G. Tanner, V. Makarov, and R. H. Hadfield, *Optimised quantum hacking of superconducting nanowire single-photon detectors*, Opt. Express **22**, 6734 (2014).

[11] L. Lydersen, N. Jain, C. Wittmann, Ø. Marøy, J. Skaar, C. Marquardt, V. Makarov, and G. Leuchs, *Superlinear threshold detectors in quantum cryptography*, Phys. Rev. A **84**, 032320 (2011).

Calibrating Qubit Gates on a $^{40}\text{Ca}^+$ Ion

Brennan de Neeve,[1] Vlad Negnevitsky,[1] Andrey Lebedev,[2]
Matteo Marinelli,[1] Christa Flühmann,[1] and Jonathan Home[1]
[1]*Institute of Quantum Electronics, ETH-Hönggerberg, CH-8093, Zürich, Switzerland*
[2]*Institute for Theoretical Physics, ETH Hönggerberg, CH-8093 Zürich, Switzerland*

We investigate the use of quantum phase-estimation and classical Bayesian estimation to optimise the calibration of single-qubit gates in a trapped ion quantum computer. We first implement a non-adaptive phase estimation procedure to calibrate laser pulses used to perform single-qubit gates on a $^{40}\text{Ca}^+$ ion qubit. We then improve the accuracy of the procedure by applying Bayesian adaptive estimation as a sub-routine of the non-adaptive method.

I. INTRODUCTION

Although much of the theory of quantum error correction is now well-established, it remains a challenge to experimentally achieve error rates below the thresholds set by quantum error correction theorems. Maintaining low coherent errors for experiments of increasing complexity is an important part of this challenge, where accurate knowledge about the physical system must be obtained.

Here we demonstrate the use of non-adaptive phase-estimation to calibrate the frequency and time of a laser pulse used to perform single-qubit gates on a $^{40}\text{Ca}^+$ ion qubit. We then improve the accuracy of our estimation procedure by implementing adaptive Bayesian estimation as a subroutine of the original procedure.

II. CALCIUM ION QUBIT

Our physical qubit is encoded into the internal states of a trapped $^{40}\text{Ca}^+$ ion. Relevant internal states and transitions are shown in figure 1. The levels used for the optical qubit are the $|\text{S}_{1/2}, \text{m} = +1/2\rangle$ ground state and $|\text{D}_{5/2}, \text{m} = +3/2\rangle$ metastable excited state. The qubit levels are coupled by a quadrupole transition at 729 nm with a lifetime on the order of one second[1].

Qubit state preparation in the $|\text{S}_{1/2}, \text{m} = +1/2\rangle$ ground state is achieved by applying 397 nm light to couple the $|\text{S}_{1/2}, \text{m} = -1/2\rangle$ state through a dipole-allowed transition to the $\text{P}_{1/2}$ states while simultaneously applying light at 866 nm and 854 nm to couple the $\text{D}_{3/2}$ to the $\text{P}_{1/2}$ levels and the $\text{D}_{5/2}$ to the $\text{P}_{3/2}$ levels, respectively.

Qubit readout is performed by applying 397 nm light while simultaneously applying 866 nm light to prevent populating the $D_{3/2}$ levels.

III. SINGLE-QUBIT GATE CALIBRATION

Changes in experimental conditions such as the magnetic field at the location of the ion or the operating temperature of control devices make it necessary to calibrate the frequency and time of a 729 nm laser pulse applied to a $^{40}\text{Ca}^+$ ion qubit in order to achieve accurate single-qubit gates. For example the evolution operator on a single-qubit resulting from a resonant laser pulse of duration t can be written[2,3]

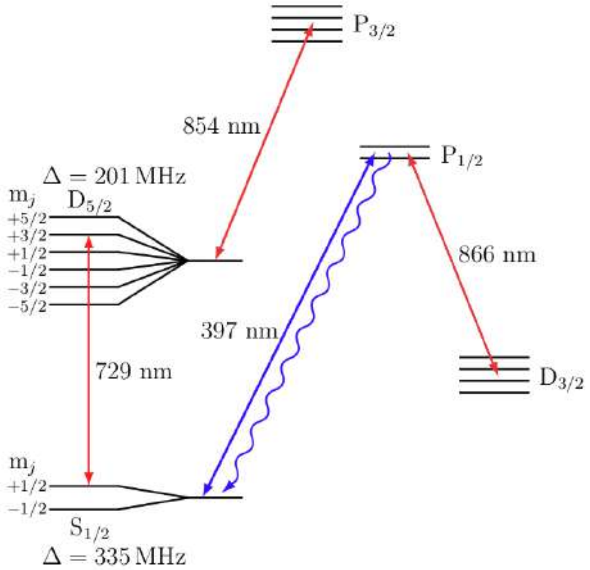

FIG. 1: $^{40}\text{Ca}^+$ energy levels and transitions. The Zeeman splittings shown are for a magnetic field of $\simeq 119$ G.

$$U_{\text{pulse}}(\Omega t) = \cos\left(\frac{\Omega t}{2}\right)\mathcal{I} - i\sin\left(\frac{\Omega t}{2}\right)\sigma_x\,. \quad (1)$$

where Ω is the Rabi-frequency, $\mathcal{I}$ is the single-qubit identity operator, and σ_x the Pauli x operator. Applying an accurate evolution to the qubit requires accurate knowledge of how the parameter Ω is related to the inputs of our experimental control system. Here we achieve this by estimating the phase Ωt in (1) for a given set of control inputs. A similar approach can be taken to estimate the detuning $\omega - \omega_0$ of the laser pulse, where ω is the angular frequency of the laser, and ω_0 is the transition frequency of the qubit.

In order to obtain the desired phase estimates, we apply the procedure described by Kimmel *et al.*[4,5]. Here we give a brief summary of the method; please see their technical work for a more detailed analysis.

For a given set of control system inputs, we apply a

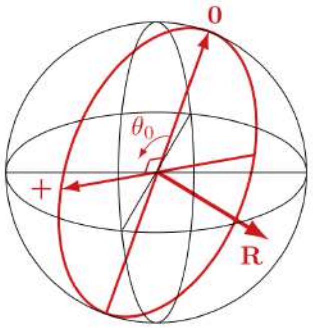

FIG. 2: The phase θ_0 of an arbitrary qubit rotation, about an axis **R**, is represented on the Bloch sphere. The measurement axis for the $|0\rangle$ measurements is defined along the initial pure state used by the procedure, and the axis for the $|+\rangle$ measurements lies in the plane of rotation at an angle of $\pi/2$ from the initial state vector.

qubit rotation with phase θ_0 followed by a measurement in one of two bases, we refer to here as a $|0\rangle$ measurement and a $|+\rangle$ measurement. The $|0\rangle$ measurement corresponds to a projection along the initial state, and the $|+\rangle$ measurement to a projection along the state corresponding to the initial state followed by a $\pi/2$ rotation as shown on the Bloch sphere in figure 2.

By repeating S experiments for each of the measurements (for a total of $2S$ experiments), we obtain an estimate for the phase $\hat{\theta}_0 = \mathrm{atan2}\,(n_+ - S/2,\, n_0 - S/2) \in (-\pi,\, \pi\,]$ where n_0 and n_+ are the total number of successful outcomes for the $|0\rangle$ and $|+\rangle$ measurements, respectively.

We improve the accuracy of our estimate by increasing the number of applications of the phase θ_0 before measurement. We repeat the procedure described above for $j = 1, 2, \cdots, K$ and apply the phase a number of times $k_j = 2^{j-1}$ before each measurement performed at step j. Using the estimate $\hat{\theta}_0$ from the previous step $j-1$, we determine the principal range (number of factors of 2π) for the phase estimate at the j^{th} step of the procedure.

We further improve the accuracy of estimation compared to the original proposal by Kimmel *et al.* by replacing the $|0\rangle$ and $|+\rangle$ measurements at each step j by Bayesian adaptive estimation. We represent our knowledge of the phase θ_0 by a probability density $P(\theta)$. We update the density after s measurements, $P_s(\theta)$, by applying Bayes theorem: $P_s(\theta) \propto p(\xi_s|\phi,\theta)P_{s-1}(\theta)$, where $p(\xi_s|\phi,\theta) = \frac{1+\xi_s\cos(\phi-\theta_0)}{2}$ is the probability of measuring the qubit "spin" state $\xi_s = \pm 1$ (up or down) given an applied rotation of phase θ_0 and a laser phase ϕ. We then choose the laser phase ϕ for the next step to maximise the expected entropy gain at step s of the procedure.

IV. RESULTS

Measured estimation accuracies obtained by applying both the non-adaptive and adaptive procedures to a $^{40}\mathrm{Ca}^+$ ion qubit are plotted in figure 3. We estimate the $\pi/2$-time $t_{\pi/2}$ such that $\Omega t_{\pi/2} = \pi/2$ (see equation (1)) using different values of the total number of steps K.

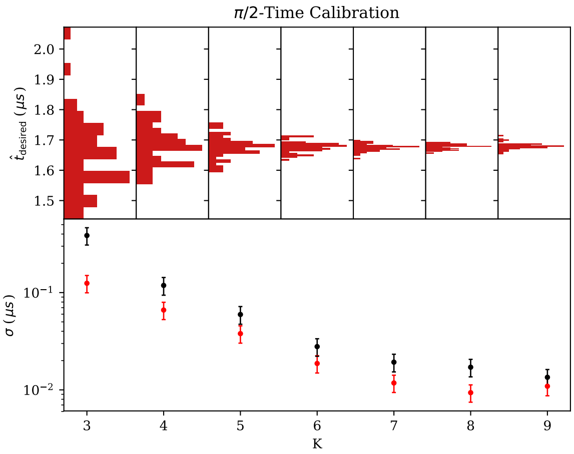

FIG. 3: Experimental estimates for $\pi/2$-time obtained by applying 50 repetitions of calibration using the non-adaptive (black) and adaptive (red) procedures applied with different total number of steps K. Each point in the lower plot shows the sample standard deviation of estimates for the 50 repetitions. The upper plot shows the histogrammed estimates for the adaptive procedure.

---

[1] M. Block, O. Rehm, P. Seibert, and G. Werth, *3d D-2(5/2) lifetime in laser cooled Ca+: Influence of cooling laser power*, The European Physical Journal D - Atomic, Molecular, Optical and Plasma Physics **7**, 461 (1999).

[2] S. Haroche and J.-M. Raimond, *Exploring the Quantum Atoms, Cavities and Photons* (Oxford University Press, 2006).

[3] J. J. Sakurai and J. Napolitano, *Modern Quantum Mechanics* (Pearson, 2011), 2nd ed.

[4] S. Kimmel, G. H. Low, and T. J. Yoder, *Robust calibration of a universal single-qubit gate set via robust phase estimation*, Physical Review A **92**, 062315 (2015).

[5] B. L. Higgins, D. W. Berry, S. D. Bartlett, M. W. Mitchell, H. M. Wiseman, and G. J. Pryde, *Demonstrating Heisenberg-limited unambiguous phase estimation without adaptive measurements*, New Journal of Physics **11**, 073023 (2009).